Department of Precision and Microsystems Engineering

Controlling the deposition resolution of nanoparticle aerosols using aerodynamic focusing

R. Sobhi

Report number   : 2020.066
Responsible supervisor   : Dr. Ir. M. Tichem
Daily supervisor   : S. Aghajani, MSc
Specialisation   : Micro and Nano Engineering
Type of report   : Master thesis
Date   : December 18, 2020

TU Delft

Delft
University of
Technology

Challenge the future

Controlling the deposition resolution of nanoparticle aerosols using aerodynamic focusing

BY

R. Sobhi

to obtain the degree of Master of Science
at the Delft University of Technology,
to be defended publicly on Friday December 18, 2020

TU Delft

Acknowledgements

After a very interesting and intensive period of one year, this research has come to an end. This thesis contained a lot of hard, yet always informative, moments. A few months into my research, the COVID-19 pandemic broke out. Despite this pandemic, help was provided to me in various ways and for that I am deeply grateful.

It is with immense gratitude that I acknowledge the support and help of my responsible supervisor, dr. ir. M. Tichem. I am very thankful that he gave me the opportunity to do this research.

Many thanks to S. Aghajani, MSc for being my daily supervisor. Saleh always made an effort to help me when I was stuck.

Thank you dr. ir. R.A.J. van Ostayen, for being part of the committee and providing me with interesting feedback and discussions.

I would also like to thank the MNE group for giving me new insides in the micro and nano engineering field.

Thank you Patrick van Holst, and all the other lab-responsibles, for helping me when needed and providing me with the necessary lab trainings.

Finally, I would like to thank my family and friends for supporting me during this intensive period.

<div align="right">

R. Sobhi
Rotterdam, December 3, 2020

</div>

Abstract

The demand for nanoparticles in various applications is increasing. These applications can only be realised if nanoparticles can be specifically arranged and patterned on a substrate. This thesis considers a direct write method that uses an aerodynamic focusing nozzle to deposit these particles. A major challenge arises when the nanoparticles are decreased in size. This research studies the control of the deposition resolution of small sized nanoparticles ($\leq$ 10 nm) in an aerosol flow.

A FEM model was developed to describe the particle's path. These models were made for a converging and converging sheath gas nozzle. Due to the small particle sizes considered, it was found that only the Stokes (drag) force needs to be accounted for during modelling. The effect of different nozzle exit throat, working distance, angle and flow rate configurations are studied. Nozzle designs were evaluated using three performance criteria, namely the contraction factor, focusing ratio and line width. These describe the contraction of the particles within the nozzle system, the focusing after the nozzle system and the width of the line, respectively.

It was found that smaller angles, longer converging sections and higher velocities resulted in smaller line widths. Also, the contraction factor hardly depends on the particle size. Smaller nozzle exit throats have significantly higher focusing ratios for particles smaller than 10 nm. The working distance does not effect the contraction factor directly, indicating capabilities of deposition on non-flat surfaces.

The converging nozzles can only deposit $\leq$10 nm particles if the nozzle exits are sufficiently small. This can cause clogging. The focusing ratios, in these nozzles, never exceeds the value of one, indicating always a larger line width than the nozzle exit diameter.

In the sheath gas nozzle system, high sheath gas ratios are essential for increasing the contraction factor and particle velocity. This prevents clogging. Introducing the sheath gas earlier in the nozzle system is more effective than at the end.

The best modelled contraction factor, focusing ratio and line width achieved, using 10 nm particles, with a converging nozzle are 1.0, 0.4 and 874 microns, respectively. This nozzle has a nozzle exit throat of 400 microns and an angle of 10 degrees. However, a modelled contraction factor of 9.3, focusing ratio of 3.8 and line width of 104 microns are achieved using a converging sheath gas nozzle with a nozzle throat of 400 microns and an angle of 5 degrees. Narrower line widths are expected if the throat diameters are reduced.

For the experiments, a setup was used in which nanoparticles are generated using a spark ablation method. During these experiments it was seen that the maximum flow rate is mainly dependent on the nozzle exit throat of the aerosol channel. The line widths, during experimenting, were found to be wider due to inaccuracies in the stage and the differences in settings between the model and setup.

Contents

List of Symbols

The symbols are given in chronological order of this thesis.

$\mathbf{F}_{St}$	[N]	Stokes force
$\mathbf{F}_{Ba}$	[N]	Basset force
$\mathbf{F}_{Vm}$	[N]	Virtual mass force
$\mathbf{F}_{Ps}$	[N]	Pressure gradient force
$\mathbf{F}_{Gr}$	[N]	Buoyancy force
$\mathbf{F}_{Ma}$	[N]	Magnes lift force
$\mathbf{F}_{Sa}$	[N]	Lift force
$\mathbf{F}_{Sum}$	[N]	Sum of all forces
a	[m]	Particle radius
kT	[J]	Thermal energy
μ_f	[Pa s]	Fluid viscosity
μ_p	[Pa s]	Particle viscosity
$\mathbf{u_f}$	[m/s]	Fluid velocity
$\mathbf{u}_p$	[m/s]	Particle velocity
ρ_f	[kg/m^3]	Fluid density
ρ_p	[kg/m^3]	Particle density
t	[s]	Time
τ	[s]	Relaxation time
c_M	[-]	Added mass coefficient
m	[kg]	Particle mass
$\mathbf{g}$	[ms^{-2}]	Gravitational acceleration
ω	[m/s]	Vorticity of the medium surrounding the particle
$\mathbf{\Omega}$	[rad/s]	Angular velocity of the particle
R	[m]	Capillary radius
$\mathbf{e}_x$	[-]	Horizontal unit vector
$\mathbf{e}_y$	[-]	Vertical unit vector
Re_p	[-]	Reynolds particle number
$\mathbf{U}$	[m/s]	Particle velocity field
$\mathbf{U}_p$	[m/s]	Fluid velocity field
C_m	[kg/m^3]	Particle mass variation concentration
η	[-]	Contraction factor
r_0	[m]	Radial position of particle before lens
r_p	[m]	Radial position of particle after lens
D_p	[m]	Particle diameter
C_s	[-]	Correction factor for Stokes law

f_d	[-]	Correction factor for Stokes law
U_0	[m/s]	Characteristic flow velocity
L_0	[m]	Characteristic length
Kn	[-]	Knudsen number
Kn_p	[-]	Knudsen particle number
A	[-]	Constant for correction factor for Stokes law
B	[-]	Constant for correction factor for Stokes law
Q	[-]	Constant for correction factor for Stokes law
λ_0	[m]	Mean free path
Ma	[-]	Mach number
v	[m/s]	Flow velocity
a	[m/s]	Speed of sound
γ	[-]	Ratio of specific heats
p^*	[Pa]	Minimum downstream pressure
p_1	[Pa]	Upstream pressure
p_2	[Pa]	Downstream pressure
L_m	[m]	Distance of nozzle exit to the Mach disk
S^*	[-]	Stokes critical value
κ	[-]	Isentropic coefficient
R	[J/(K mol)]	Ideal gas constant
T	[K]	Temperature
A	[m^2]	Cross section of the nozzle
A^*	[m^2]	Minimum cross section of the nozzle
FR	[-]	Focusing ratio
$\mathbf{I}$	[-]	Identity matrix
$\mathbf{F}$	[N/m^3]	Volume force vector
C_p	[J/(kg ΔK)]	Specific heat capacity at constant pressure
$\mathbf{q}$	[W/m^2]	Heat flux vector
$\mathbf{Q}$	[W/m^3]	Heat sources
$\mathbf{S}$	[s^{-1}]	Strain rate tensor
τ	[Pa]	Viscous stress tensor
S_k	[-]	Sutherland constant
k	[W/(mK)]	Thermal conductivity
k_0	[W/(mK)]	Thermal conductivity at reference temperature
μ_0	[Pa s]	Viscosity at reference temperature
$\mathbf{x}$	[m]	Particle position
r	[m]	Particle radius
Q	[m$^3/s$]	Volumetric flow rate
d	[m]	Particle diameter

List of Abbreviations

ABS	Acrylonitril-butadieen-styreen (material)
A-DW	Aerosol-based direct writing
AL	Aerodynamic lenses
AM	Additive Manufacturing
A/T	Aerosol/total flow rate
C	Converging
Ca	Capillary
CAB	Collimated Aerosol Beam
CAD	Computer-aided design
CAM	Computer-aided manufacturing
CD	Converging-diverging
CDC	Converging-diverging-converging
CSG	Converging sheath gas
DFM	Design for manufacturing
DPN	Dip pen nanolithography
DW	Direct writing
FEM	Finite Element Method
FR	Focusing ratio
HTM140V2	High Temperature Mold 140V2 (material)
LEEP	Laser-enhanced electroless plating
LENS	Laser-engineered net shaping
LGDW	Laser-guided direct writing
MAPLE	Matrix-assisted pulsed laser evaporation
MCS	Microcold spray
NDSU	North Dakota State University
NFP	Nano fountain pen
NT/LW	Nozzle throat/line width
PME	Precision and Microsystems Engineering
SAM	Spark Ablation Method
SG	Sheath gas
SLA	Sterolithograpy printer
STL	Stereolithography
TU Delft	Delfts University of Technology
2PP	Two-photon-polymerization

Chapter 1

Introduction

There is an increasing demand for nanoparticles, in the improvement and development of various applications, due to their unique properties. These nanotechnology applications can be found all around us, for example in food products, car coating and drug delivery. [1]

Additive manufacturing (AM) methods use information from a computer-aided design (CAD) file and convert this into a stereolithography (STL) file. [2] These methods are nowadays also used to produce products in the sub-micrometer and -nanometer scale. This category is very useful and relevant when considering the nanotechnology branch. In this branch, precision development of products is key.

Direct Writing (DW) is a flexible multi-length scale processes family for depositing functional materials on a substrate in order to form simple linear or complex conformal structures. [3] This is, for example, used in different kinds of sensors, film transistors [4], interconnects [5], solar cell grid contacts and RFID antennas [6]. The most important advantage of these technique are their wide product and manufacturing flexibility. Flow-based and droplet-based DW, are two popular ways to deposit particles within this category. These techniques are not typical high precision printers for DW. However, the writing speed and volume are usually higher than other techniques. These techniques also usually have more writing freedom, which makes it possible to write on different kinds of surfaces and roughnesses. For these (nano)particles to be deposited correctly, they have to be well focused. This focusing is often created by using a good nozzle system. Designing such a nozzle system for relatively small (nano)particles is very challenging since the focusing then becomes significantly more difficult than for larger particles.

The aim of this thesis is to research: *how to control the deposition resolution of an aerosol flow of small (≤10 nm) nanoparticles*. The setup that is improved for focusing is the Spark Ablation Method (SAM) setup. This is a DW machine, based in the Precision and Microsystems Engineering (PME) department of Delfts University of Technology (TU Delft), that generates (metal) nanoparticles inline. After gaining the information needed, to be able to control the resolution of deposition of the nanoparticles, three proposed nozzle designs are given.

This thesis is structured as follows, firstly the DW field is briefly explained. Hereafter, the research approach and the problem statement are given. The physics of the aerosol, the focusing of the nozzle and examples of focusing nozzles are given in chapter 2. Chapter 3, describes the Finite Element Method (FEM) models that are constructed, using COMSOL, to understand how to control the resolution of deposition of nanoparticles. This chapter

is followed by a chapter that compares the different types of nozzles modelled in the previous chapter. Chapter 5 gives the modelling results of the proposed nozzles, the modifications made to the original SAM setup and an elaboration on the production of these nozzles. This chapter is concluded by showing a few experimental results done with the nozzles. Finally, the conclusions and recommendations are stated in the last two chapters, respectively.

1.1 State-of-the-Art

The AM method that is considered in this thesis is DW. In this section, a brief explanation of nanoparticles is firstly given. Hereafter, the State-of-the-Art of the DW techniques available is discussed.

1.1.1 Nanoparticles

Particles are categorized as nanoparticles when they have dimensions that are smaller than 100 nm. Single (nano)particles can combine and become larger particles (aggregates). Aggregates with covalent, ionic or metallic bonds are formed when the primary particles contact each other at edges and surfaces. Shear stress cannot break these aggregates further down. Agglomerates with weak bonds are formed when particles contact each other. As mentioned, these weak forces are usually due to covalent, ionic bonds working on a small contact area, but they can also be caused by Van der Waals forces. Not only the size of nanoparticles is an important characteristic, but also morphology, composition, the nature of the interfaces and distribution of phases (if multi-phases is considered) are of importance. [7]
These nanoparticles are used for various reasons. One of the reasons is that they have a high driving force for diffusion due to the high surface to volume ratio. This is specifically at higher temperatures. This then implies that these nanoparticles can be sintered over shorter time scales at lower temperatures than larger particles. The thermodynamic properties are changed due to the surface free energy. This also results in a reduced melting point. [8] So, due to the small dimensions of nanoparticles and the changing characteristics of the same material, these nanoparticles are used in multiple products as stated earlier in the introduction.

1.1.2 Direct writing

DW technologies can be classified in roughly four main categories as mentioned by Hon et al. [3]. However, most of the following techniques use particle diameters of ≥ 100 nm. Figure 1.1 shows a compact classification of the DW field. The bold terms in this chart, indicates what is further discussed in this thesis. This overview is briefly elaborated on in this section.

The first category made, is the *flow-based DW*. Here, the delivery of the material is flowable and gas is used during the process. This technique uses technologies such as the MicroPen and the nScript with an orifice or needle for the micro dispensing. This system then can continuously deposit features with speeds between 0.1 mm/s and 300 mm/s. These features can be as small as roughly 25 μm, the flow rates are in the nL/s range, viscosity from 0.5 MPa s to 10^6 MPa s. This allows to deposit a large amount of different ink compositions. [3]
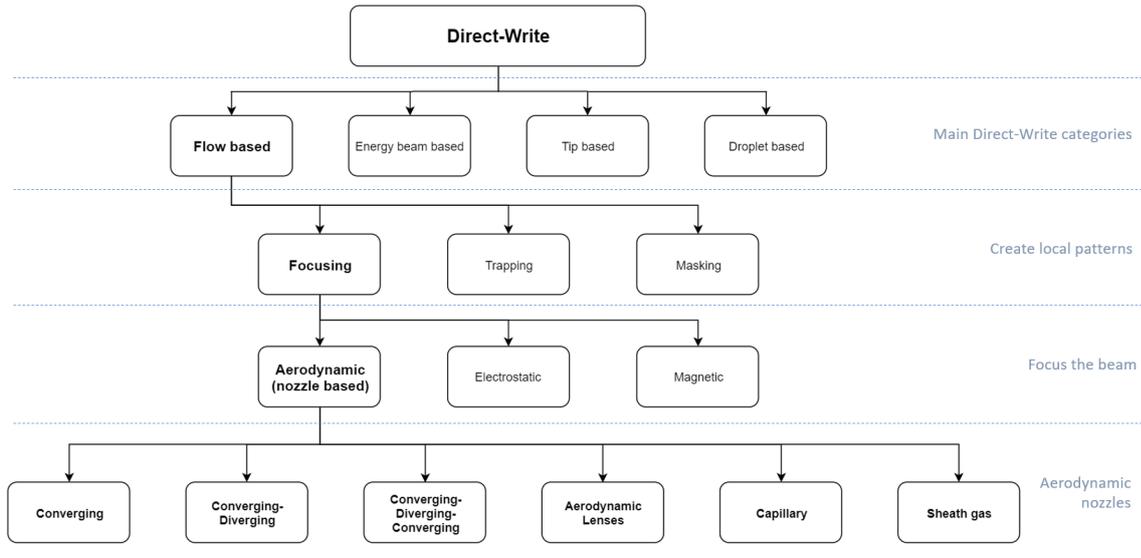
Figure 1.1: A compact summary chart of the direct write field, where the bold terms indicate the focus of this research.

Most flow-based techniques are wet or dry systems that do not produce the particles inline. The deposited droplet diameter and line width are approximately 5-100 μm and 25-400 μm, respectively. The particle diameter within these droplets are approximately 0.5-2 μm. [3, 9]

Within flow-based DW there are different methods that can be distinguished to create local patterns (i.e. to do a selective patterning): focusing the beam, local trapping of particles from a flow or masking. There are roughly three ways to focus the beam: aerodynamic focusing (nozzle based), electrostatic focusing and magnetic focusing. There are different nozzle types within aerodynamic focusing: converging (C), converging-diverging (CD), aerodynamic lenses (AL), converging-diverging-converging (CDC), capillary (Ca) and sheath gas (SG) nozzles. These nozzles are discussed in section 2.5.

The second category is called *energy beam based DW* because it uses technologies that are equipped with high-power lasers. The material on the substrate is transformed and/or propelled by the use of these lasers. A variety of techniques are covered by laser-based systems such as: matrix-assisted pulsed laser evaporation DW (MAPLE-DW), laser-enhanced electroless plating (LEEP), laser-guided DW (LGDW) [10], laser-engineered net shaping (LENS) [11], and Mesoscribe Technologies [12]. Laser-trimming the patterns can realize writing features with resolution on the line width down to 2 μm [13]. Some non-laser-based approaches such as focused ion beam DW are also included in this category. Using gallium and precursor gases volumetric print rates of 0.05 $\mu m^3/s$ and features down to 80nm can be written [3].

Most energy beam based techniques are dry systems that can both can produce particles inline or not inline. The deposited particle diameter and line width are approximately 0.05-10 μm and 0.1-50 μm, respectively. [3, 10, 11, 12, 13, 14, 15]

The third category is called *tip-based DW*. As the name already indicates, this category uses techniques that use their tips to write. Nano fountain pen (NFP), capillary-based liquid microdroplet deposition and dip pen nanolithography (DPN) are tip-based DW technologies [16]. Non capillary tip-based DW techniques can reach down to sub-100 nm

resolution, where the capillary based only reached a maximum resolution of 32 μm. All techniques are either very close to or touch the substrate when writing.

Most tip-based techniques are wet systems that do not produce the particles inline. The deposited droplet diameter and line width are approximately 0.1-10 μm and 0.05-50 μm, respectively. [3, 16]

The last category discussed is called *droplet-based DW*. Within this category droplets containing (nano)particles are prouced and eventually deposited. A very popular technique within this category is the "Inkjet printer". This technology uses electrostatic, hydro-dynamic, piezoelectric, acoustic and thermal energy to produce small droplets of liquid. Hereafter, these droplets are ejected from a nozzle. There are two versions of this technique: continuous inkjet (CIJ) and drop-on-demand (DOD). Using inkjet techniques resolutions down to 20 μm are realized. For high-throughput operations the noncontact approach is scalable, where hundreds to thousands of nozzles can be installed in a single head. Since only a limited viscosity range is atomizable, inkjet is very sensitive to the characteristics of the printing ink. Also, a certain volatility is required for correct drying of the deposited ink. However, when the ink is too volatile nozzles can easily get stuck. What complicates printing over nonplanar substrates in this technique, is that the nozzle-to-substrate distance must be precisely controlled. [3]

Most droplet-based techniques are wet systems that do not produce the particles inline. The deposited droplet diameter and line width are approximately 5-100 μm and 1-100 μm, respectively. The particle diameter within these droplets are approximately 0.05-2 μm. [3, 9, 17, 18, 19, 20, 21]

A subset of droplet-based DW is Aerosol-Based DW (A-DW). The definition of an aerosol is a suspension of fine liquid or solid particles in a gas. A-DW technique is an additive process which prints CAD/CAM features using machines that use a solid or liquid beam. Collimated Aerosol Beam DW (CAB-DW) and Aerosol Jet are two A-DW methods that are developed by North Dakota State University (NDSU) and Optomec, respectively [17, 18]. Both techniques deposit material with sub-10 μm resolution using a focused aerosol spray. Microcold spray (MCS) is an example of a method that uses a solid feed and can be seen in fig. 1.2.
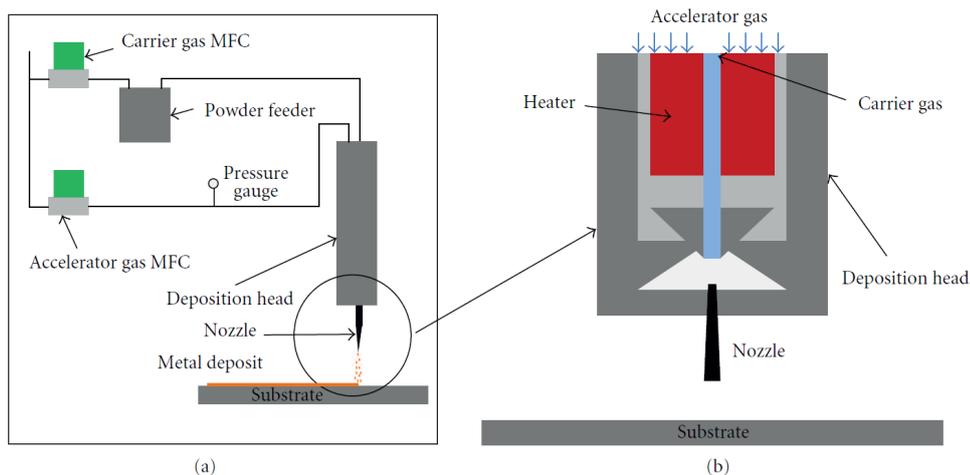

Figure 1.2: The Microcold spray system is shown in (a), where the deposition head of this Microcold spray is shown in (b). This schematic overview is for solid aerosols and was made by Bhattacharya et al. [20]

This method deposits ductile metal particles onto a substrate after accelerating these particles to near or above sonic velocities through a focusing nozzle [19, 20]. The main difference between MCS, Aerosol Jet and CAB-DW is that MCS deposits lines that exhibit conductivities near the bulk value without a thermal treatment afterwards.

Optomec [21] showed that when adding sheath gas to their nozzle in the Aerosol Jet Printer, focusing was improved. The streamlines of the aerosol can then be focused to a tenth of the nozzle orifice. This resulted in a minimum line width of approximately 10 μm. However, the particles that were deposited are larger than the nanoparticle size range.

This technology (see fig. 1.3) roughly consists of two main parts, the Mist Generation and the In-Flight-Processing [21].
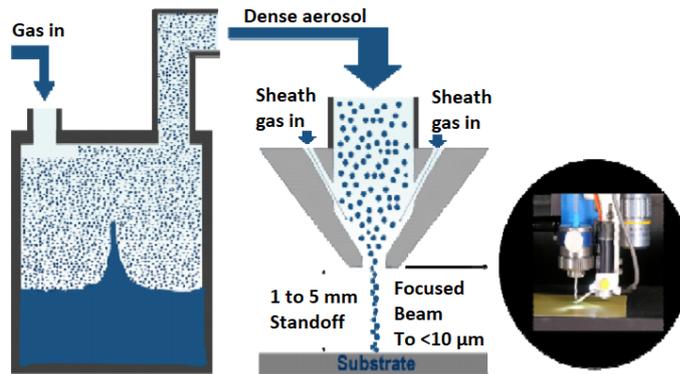

Figure 1.3: A schematic representation of the Aerosol Jet Printer made by Optomec. [21]

The "Mist Generation" part atomizes liquid raw material, which is done by the use of an pneumatic or ultrasonic atomizer. After this step the aerosol is formed. Hereafter, this aerosol flow needs to be focused and the droplets need to be eventually deposited. This is done in the "In-Flight-Processing" part. To focus this aerosol stream, a deposition head is used that forms an annular, coaxial flow between this stream and a sheath gas stream. This flow eventually exits the print head, and the droplets are deposited on the substrate in front of it, through a nozzle. Focusing the aerosol with this technology, a stream width of a tenth of the nozzle orifice can be achieved. This technology is CAD driven, which means that from a standard ".dxf file" a pattern is directly written. This patterning is then made by placing a substrate on a surface, 1 to 5 mm from the nozzle exit, and moving this by a computer-controlled system. However, the substrate can also be fixed and the deposition head can be translated.

After this deposition process, a post process is often needed. This is usually done to increase certain properties of the deposited material, such as electrical conductivity, or to cure this deposited material. The post processing differs for different materials, mainly because not all materials can handle the high-temperature post processing (ca. 250 $°C$). However, a laser can be integrated in the system which enables sintering of the deposited material while leaving the substrate unharmed.

1.2 Problem statement and goal

Most research done on aerodynamic focusing only considers particles in the range of hundreds of nanometer to hundreds of micrometers. Focusing the relatively small nanoparticles is very challenging. When decreasing the size of the (nano)particles that are desired to be deposited, these particles will be more likely to follow the streamlines when exiting the nozzle due to their smaller relaxation time. [22] This results in less focusing after the nozzle exit and wider line widths. This behaviour is further clarified in chapter 2.

This thesis focuses on being able to control the deposition of small nanoparticles. Hence, the problem statement of the research is: *Controlling the deposition resolution of an aerosol flow of ≤10 nm nanoparticles.* The setup available at the PME department in TU Delft, is an aerosol DW method that uses aerodynamic focusing. It is chosen to study the control of deposition of these small particles on this system. This setup is further described in section 1.3. The desired goal of the project is: *Designing a nozzle system for a flow-based DW setup that controls the deposition resolution to aerodynamically focus ≤10 nm nanoparticles to a line width of approximately 100 µm.* Section 1.4 explains what method is used to manufacture these nozzle systems.

1.3 Direct write setup

The setup used is named the Spark Ablation Method (SAM). SAM is used to aerodynamically focus the continuously generated nanoparticles inline. The discharge that is used in this generator enables the system to produce metal or alloy nanoparticles (see fig. 1.4). To generate these nanoparticles, two electrodes are placed in the same plane directly in front of each other. The electrodes are then locally heated to very high temperatures (typically 20000 K [23]) which results in locally evaporation of the material.

Figure 1.4: A spark discharge generator that is also used at the Precision and Microsystems Engineering department in Delfts University of Technology. [24]

Hereafter, a gas carries the vaporized materials (nanoparticles). In this setup this gas is chosen to be argon. A high concentration of nanoparticles is formed due to that the vapor cloud, that is formed by the electrodes, is very small compared to other evaporation-condensation processes. This also results in relatively fast cooling below the boiling point. [7] After the atoms leave the electrodes they start to coalescence and form, ca. 0 nm to 20 nm, spherical nanoparticles (primary particles). Hereafter, these primary particles start to agglomerate and thus from (larger) differently shaped and sized (nano)particles. This process is shown in fig. 1.5.
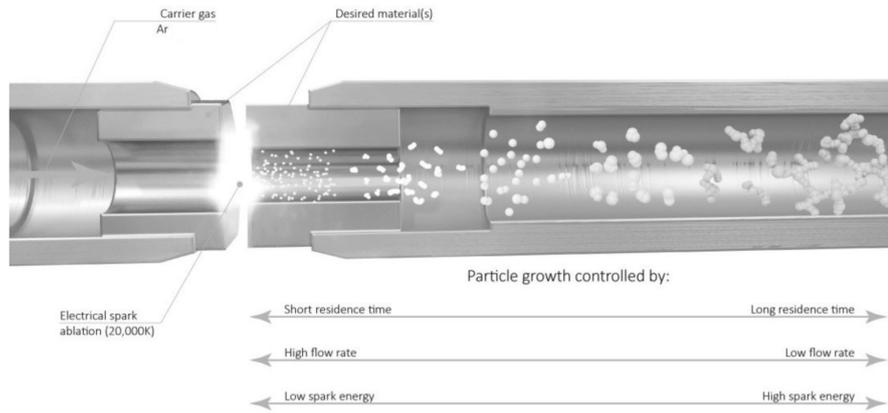
Figure 1.5: Generation of (nano)particles using the spark discharge generator used in the setup at the Precision and Microsystems Engineering department in Delfts University of Technology. [24]

Thus, the result is an aerosol of argon gas mixed with polydisperse metal or alloy nanoparticles. This aerosol is then is directed to a nozzle (in a vacuum chamber) which significantly increases the velocity of the (nano)particles and eventually focuses these (nano)particles on a substrate. [7] This setup is shown in fig. 1.6.
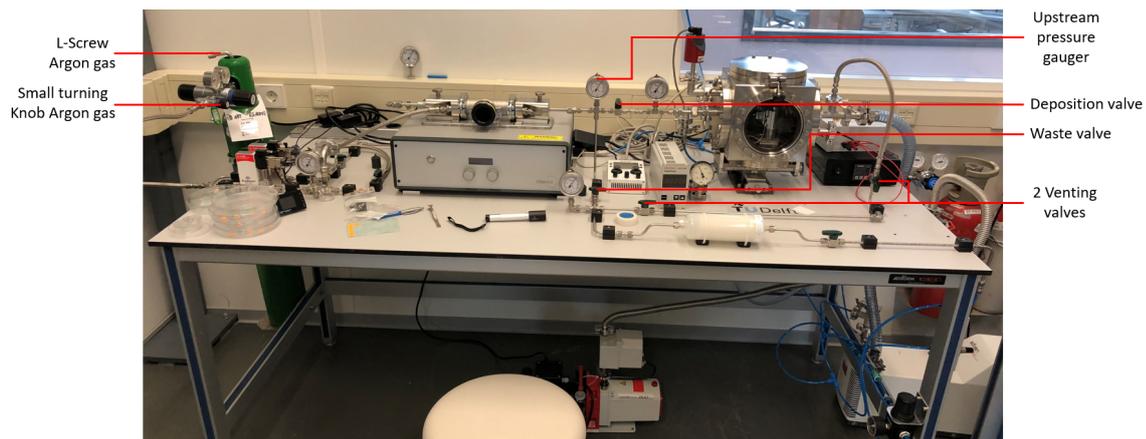

Figure 1.6: Original Spark ablation method setup.

A few experiments, on this setup, showed that the regular C nozzles reached a line width of approximately 400-700 μm. However, the SAM setup also brings advantages to the aerodynamic flow-based DW field. First, the flow is more pure, in the sense of the particles in it. Since the system is inline everything happens at once, which results in no additional contamination. Secondly, this system uses atmospheric pressure which makes it easier to install. Also, the system uses electrodes that are only locally heated to create the (nano)particles. This makes the electrodes in the system long lasting. Most setups use cartridges that need to be replaced frequently. Finally, this setup has a high throughput.

1.4 Approach

To be able to focus the small particles as desired, a (aerodynamic) focusing system needs to be designed (nozzle). The two approaches used to design such a good nozzle are given in the bullet points below.

- **Shape and geometry** - By manipulating the shape and geometry of the nozzle, the streamline conditions and velocity of the particles in it can be varied. If this is designed correctly, a shape can be manufactured to focus these nanoparticles to the desired goal.

- **Sheath gas** - By making a nozzle with sheath gas implemented in it, the streamlines can be focused in a certain direction. By using this technique the desired goal can be achieved.

By changing the shape and geometry of the nozzle, the performance of the focusing could be improved. To understand which shapes and geometries could positively influence the resolution of deposition, the physics of aerosol and different nozzles are studied, as given in chapter 2.

Implementing sheath gas should help increase the focusing. When adding sheath gas to a nozzle, the particles that leave the nozzle are forced to stay near the centerline and should eventually result in narrower lines when deposited. The designed nozzle should be able to be connected to the sheath gas line of the system and be leak proof at the same time.

The two nozzles to be studied are: a regular C nozzle and a converging sheath gas (CSG) nozzle. First, the regular C nozzle is modelled in COMSOL and studied. Hereafter, different sheath gas flows are calculated and the CSG nozzle is studied using COMSOL. Hereafter, the proposed nozzles are studied and printed. Finally, some experiments with the designed nozzle are done. The design and operational parameters that are studied are mentioned in the bullet points below.

- Design: The diameter of the exit of the nozzle (nozzle exit throat).

- Design: The sheath gas entry at different points (nozzle length) and angle of deposition (angle).

- Operational: The distance to the substrate (working distance).

- Operational: Different distribution of the aerosol and sheath gas flow rates.

To be able to have more shape and material freedom when designing the nozzle system, it is chosen to 3D print the nozzles. The Stereolithography (SLA) type 3D printer is available at PME and is used to print the nozzles. This 3D-printer, prints with a resolution of approximately 300 microns. [25, 26] There are a few materials that can be used with the SLA printer: Acrylonitril-butadieen-styreen (ABS) tough and High Temperature Mold 140V2 (HTM140V2). They are both polymers, however the latter one has a better resolution. Hence, HTM140V2 is the material used to print the nozzles.

1.5 Research questions

A few problems need to be solved to be able to reach the goal. These problems are formulated in the research question and are given in the bullet points below.

- What model is capable of showing the deposition resolution of different nanoparticles sizes and how is this model made?

- How do the shape and geometry of the nozzle influence the deposition resolution?

- How does the distance of the nozzle to the substrate influence the deposition resolution?

- How does sheath gas influence the deposition resolution?

- How do these design and operational parameters influence different particle sizes?

- Can this polydisperse setup study the line width of small particles or is a size selector needed?

At the end of this research one should be able to answer these questions.

Chapter 2

Aerosol Science and Technology

To be able to control the resolution of deposition of nanoparticles, the physics of aerosols needs to be understood. This chapter will first explain the general physics of aerosol particles in a flow and the forces acting on it. Then, the trajectory of relatively small particles in a flow are explained. Hereafter, the flow and collection of these particles after exiting the nozzle is discussed. Finally, the different types of nozzles are given and elaborated on.

2.1   Forces

The seven main forces that are acting on a particle in a fluid, when modelled as aerosol, are given in eq. (2.1).

$$\sum \mathbf{F} = \mathbf{F}_{St} + \mathbf{F}_{Ba} + \mathbf{F}_{Vm} + \mathbf{F}_{Ps} + \mathbf{F}_{Gr} + \mathbf{F}_{Ma} + \mathbf{F}_{Sa} \tag{2.1}$$

In this formula $\mathbf{F}_{St}$ is the Stokes force, $\mathbf{F}_{Ba}$ is the Basset force, $\mathbf{F}_{Vm}$ is the virtual mass force, $\mathbf{F}_{Ps}$ is the pressure gradient force, $\mathbf{F}_{Gr}$ is the buoyancy force, $\mathbf{F}_{Ma}$ is the Magnus lift force and $\mathbf{F}_{Sa}$ is the Saffman lift force [17, 27, 28, 29, 30, 31, 32, 33, 34, 35]. Where $\mathbf{F}_{St}$, $\mathbf{F}_{Ba}$, $\mathbf{F}_{Vm}$, $\mathbf{F}_{Ps}$, $\mathbf{F}_{Gr}$, $\mathbf{F}_{Ma}$ and $\mathbf{F}_{Sa}$ calculate respectively the steady viscous drag force, non-steady viscous drag force, inertia of fluid surrounding particle added to particle, pressure gradient, force caused by gravity, lift force due to particle rotation and lift force on a particle with local shear flow.

Not all seven forces are accounted for when considering small (nano)particles. Forces are only accounted for if they are not negligible compared to the Stokes force. When using particles in the range of 10 μm, the gravity force is negligible. It was found by Marshall that the Basset force may be neglected [31]. The virtual mass force, Basset force and pressure gradient force could be ignored according to Crowe et al. [29]. The maximum particle diameter used in this research is 100 nm, which is much smaller than this. Akhatov et al. stated that the two most important forces are the Stokes and Saffman forces [17].

The randomness of particles suspended in a fluid can be described by the Brownian motion. This random motion is due to collision between the fast-moving molecules in the fluid. This is shown in eq. (2.2).

$$|\mathbf{F}_{Sum}| \, 2a \leq kT \tag{2.2}$$

In this equation F_{Sum} are all the forces acting on the particle. This phenomena can be neglected when the thermal energy kT is less than the energy that is needed to move a particle a the same distance as its diameter. Considering room temperature the termal energy will be $kT = 4 \times 10^{-21} \text{m}^2\text{kgs}^{-2}$. Using eq. (2.2), F_{Sum} has to be between $1 \times 10^{-15}\text{N}$ and $1 \times 10^{-16}\text{N}$. The forces that will be used during this research will be much larger, so the Brownian motion can be neglected.

The stokes force was found by George Gabriel Stokes [36] by developing the first theoretical model for the forces acting on small spherical aerosol particles in a viscous fluid under laminar flow conditions and thus also a small Reynolds number ($Re_p < 1$). By solving the Navier-Stokes equation (equations of motion) for laminar flow around a cylinder and sphere, Stokes came up with the force on a particle as stated in eq. (2.3) [37, 38, 39]. This equation gives the force exerted.

$$\mathbf{F}_{St} = 6\pi a \mu_f \left(\mathbf{u_f} - \mathbf{u}_p\right) \tag{2.3}$$

In this equation μ_f, a and $\mathbf{u} - \mathbf{u_p}$ are the fluid viscosity, particle radius and the fluid velocity relative to the moving particle [37, 38, 39].

The Basset force can be important when considering high rate acceleration or deceleration. Considering the acceleration of a sphere in the Stokes regime in a quiet fluid, this force can be derived. The past acceleration on the drag is accounted for using this force. [40] The Basset force is given in eq. (2.4).

$$\mathbf{F}_{Ba} = 6a^2\sqrt{(\pi\rho_f\mu)} \int_0^t \left(\frac{d\mathbf{u}_f/dt - d\mathbf{u}_p/dt}{\sqrt{t-\tau}}\right) d\tau \tag{2.4}$$

In this equation $(t - \tau)$ and ρ_f are the elapsed time since previous acceleration from 0 to t, where τ is the stokes relaxation time and the density of the fluid, respectively.

The ratio of the Basset to the Stokes force is given in eq. (2.5). [40]

$$\epsilon_{Ba} = \frac{|\mathbf{F}_{Ba}|}{|\mathbf{F}_{St}|} = \sqrt{\frac{18\rho_f\tau}{\pi\rho_p t}} = \sqrt{\frac{18\rho_f a^2}{\pi\mu t}} \tag{2.5}$$

For the Basset force to be large, the particles have to accelerated at a very high rate ($t << \tau$). Considering the maximum particle size to be 10 μm, which is much larger than in our case, this would result in a t of 0.00004 s. In this research this would be even a smaller number. Hence, this is not an acceleration that the particles will reach so that is why the Basset force can be neglected.

The Virtual mass force is considered when looking at the inertia added to a system. Deflection is caused when a solid body moves through a fluid or gas. Extra inertia will be added, since the carrier and body cannot occupy the same physical space at the same time. [41] This equation is given in eq. (2.6).

$$\mathbf{F}_{Vm} = -c_M\frac{\rho_f}{\rho_p}m\left(\frac{d\mathbf{u}_f}{dt} - \frac{d\mathbf{u}_p}{dt}\right) \tag{2.6}$$

In this equation m is the particle's mass and c_M is the added mass coefficient. This coefficient is in case of a sphere equal to 0.5.

Again, considering the largest effect of this force would be at the largest particle. This force is calculated with a particle size of 10 μm, which is much larger than the particles considered in this research. Calculating the first parts results in: $m\frac{\rho_f}{\rho_p} = \frac{4}{3}\pi\rho_f a^3 = 5\times10^{-15}$kg. If steady state is assumed then $\frac{d\mathbf{u}_f}{dt} \approx 0$. For the term $\frac{d\mathbf{u}_p}{dt}$ to be relevant it needs to scale with 10^7. Since we already established in the Basset force that such high accelerations will not be reached, this part of the equation will be too small. For this reason the Virtual mass force can be neglected.

The difference in pressure across the surface is caused by the acceleration of external flow past the particle. This is the pressure gradient force as given in eq. (2.7).

$$\mathbf{F}_{Ps} = m\frac{\rho_f}{\rho_p}\left(\frac{D\mathbf{u}_f}{Dt}\right) \tag{2.7}$$

In this equation D/Dt is the rate of change with the time following a fluid particle. This can also be written as: $\frac{D\mathbf{u}_f}{Dt} = \frac{d\mathbf{u}_f}{dt} - [(\mathbf{u}_p - \mathbf{u}_f) \cdot \nabla]\,\mathbf{u}_f$.

As shown in the Virtual masss force $m\frac{\rho_f}{\rho_p} = 5 \times 10^{-15}$kg, which is a relatively small digit. The term $\frac{D\mathbf{u}_f}{Dt}$ can be neglected. So that is why the pressure gradient force can be neglected.

To represent the weight of displaced medium the Buoyancy force is used. This force buoys up a object that is partially immersed in a fluid or gas. This force is equal to the weight of the fluid or gas displaced by this object. Equation (2.8) gives this force.

$$\mathbf{F}_{Bu} = m\left(1 - \frac{\rho_f}{\rho_p}\right)\mathbf{g} \tag{2.8}$$

In this equation $\mathbf{g}$ is the gravity constant. Equation (2.9) gives the ratio of the Buoyancy to the Stokes force.

$$\epsilon_{Bu} = \frac{|\mathbf{F}_{Bu}|}{|\mathbf{F}_{St}|} = \frac{2a^2\left(\rho_p - \rho_f\right)g}{9\mu\left(u_f - u_p\right)} \tag{2.9}$$

Since the Buoyancy force will only dominate if the relative velocity is significantly small, this force can be neglected.

When the spinning of the particle has a specific velocity, a lift force can be caused. [42] This force is the Magnus force. The velocity gradient of the flow causes a spin, this results in a difference of velocity on the particles upper and lower side. The Magnus force caused by this will push the particle to the higher velocity and is given in eq. (2.10). [40]

$$\mathbf{F}_{Ma} = -\frac{3}{4}m\frac{\rho_f}{\rho_p}\left(\frac{1}{2}\omega - \mathbf{\Omega}\right) \times (\mathbf{u}_p - \mathbf{u}_f) \tag{2.10}$$

In this equation ω and $\mathbf{\Omega}$ are respectively the vorticity of the medium surrounding the particle and the angular velocity of the particle.

The ratio of the Magnus to the Stokes force is given in eq. (2.11).

$$\epsilon_{Ma} = \frac{|\mathbf{F}_{Ma}|}{|\mathbf{F}_{St}|} \cong \frac{a^2\rho_f U_f}{6\mu R} \tag{2.11}$$

In this equation U_f and R are respectively the carrier flow mean velocity and the Ca radius.

Since the particle size is squared, it can be seen that this force will only be dominant if the particle size is large. For such small particles that will be considered in this research, it is safe to say that this force can be neglected.

The lift force applied to aerosol particles in Poiseuille flow (simple laminar shear flow) is the Saffman force. [34] This force was made by P.G. Saffman in 1965. [34] The magnitude of the relative velocity and the rate of shear of the particle with respect to the fluid is proportional to the lift. This force is calculated with eq. (2.12).

$$\mathbf{F}_{\text{Sa}} = 6.46 a^2 \left(u - u_p \right) \sqrt{\rho_f \mu_f \left| \frac{\partial u}{\partial y} \right|} \, \text{sign} \left(\frac{\partial u}{\partial y} \right) \mathbf{e}_y \tag{2.12}$$

In this equation 6.46, u and u_p are a constant determined by Saffman due to numerical integration [34], the axial velocity component of the gas and the axial velocity component of the particle.

The ratio of the Saffman to the Stokes force is given in eq. (3.10).

$$\epsilon_{\text{Sa}} = \frac{|\mathbf{F}_{\text{Sa}}|}{|\mathbf{F}_{\text{St}}|} = \frac{6.46}{12\pi} \sqrt{Re_{\text{p}}} = \frac{6.46}{12\pi} \sqrt{\frac{2 a \rho_{\text{m}} |u_{\text{f}} - u_{\text{p}}|}{\mu}} \tag{2.13}$$

As can be seen this force has a larger range of particle size where it is still dominant. For this reason the Saffman force could also be considered as a dominant force. However, this force can be neglected for maximum particle diameters of 100 nm. The calculation to show this for this research is given in section 3.2.2.

2.2 Particle carried by a fluid flow

The equations showed in the previous section are not specifically for relatively small spherical aerosol particles. This section will describe why the relatively small particles will tend to follow the streamlines.

To describe the motion of relatively small spherical aerosol particles, that are suspended in a fluid flow, Robinson's inequality can be used. This is given in (eq. (2.14). [43]

$$\frac{d\mathbf{U}_p}{dt} = \frac{\mathbf{U} - \mathbf{U}_p}{\tau} \tag{2.14}$$

In this equation $\mathbf{U_p}$, $\mathbf{U}$ and τ are the particle velocity, the fluid velocity field and the particle relaxation time, respectively. [43] However, this equation does include the aerodynamic drag effect of the particle, but it does neglect the effects of Brownian diffusion or lift forces. If the particle is in a non-uniform flow, other forces may be considered according to Fuchs and Maxey and Riley. [44, 45] But, if the volume of the particle and the fluid are the same, the particle is much heavier than the fluid and the local particle Reynolds is less or equal to a few hundred, these other forces can be neglected. [44] When considering small particles in a carrier flow eq. (2.14) is slightly different. Robinson [46] made a so called 'virtual' particle flow, this flow is a continuous spatial distribution of uniformly sized, small particles each governed by eq. (2.14). When doing so, eq. (2.14) can be written as given in eq. (2.15).

$$\frac{D\mathbf{U}_p}{dt} = \frac{\mathbf{U} - \mathbf{U}_p}{\tau} \tag{2.15}$$

In this equation $\frac{D}{dt}$ is the differentiation following the particle trajectory of the virtual field. The particle mass variation concentration is given in eq. (2.16).

$$\frac{1}{C_m}\frac{DC_m}{Dt} = -\nabla \cdot \mathbf{U}_p \tag{2.16}$$

In this equation C_m is the particle mass variation concentration and is defined as the average particle mass per unit volume of aerosol. [46].

Robinson combined eqs. (2.15) and (2.16) and came up with the Robinson's inequality given in eq. (2.17).

$$\frac{DC_m}{Dt} > 0 \tag{2.17}$$

In this inequality the relaxation time is considered to be constant. Also, it is assumed that the particles are in equilibrium with fluid far upstream. If this holds, than the equality can be made for incompressible irrotational flows. The meaning of this equality is that the local particle concentration will be more likely to increase along particle trajectories. When considering eq. (2.17) and assuming that the flow is irrotational, axisymmetric and incompressible, it is concluded that the particles will be more likely to concentrate around the centerline. However, for this inequality to be used the U_p, $\nabla \cdot \mathbf{U}_p$ and $\nabla \times \mathbf{U}_p$ have to be defined.

2.3 Contraction factor and near axis description of a particle stream

When assuming a steady laminar flow and considering where a particle is at different times in a nozzle, the contraction factor can be derived. Assuming an aerodynamic lens (type of nozzle) and fluid, with particles, passing though it as shown in fig. 2.1, this contraction factor of a particle stream can be explained.
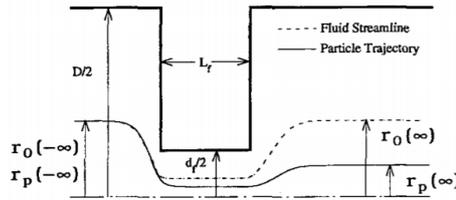

Figure 2.1: The contraction factor of a particle stream showed by using as an example an aerodynamic lens. [43]

The particle enters at a radial position $r_0(-\infty)$, when this particle passes the lens, the radial position of the particle is defined as $r_p(\infty)$. The parameter $r_p(\infty)$ will be different from $r_0(\infty)$, the radial position of the fluid streamline, because of the inertial effects present. This difference is the contraction factor of a particle stream as given in eq. (2.18).

$$\eta \equiv \frac{r_p(\infty)}{r_0(\infty)} \tag{2.18}$$

Obtaining a general analytical expressions for this contraction factor of a particle stream for a random particle size and position $r_0(-\infty)$, is not possible. Nonetheless, when

a particle is close to the axis and is small, the near axis description of a flow can be used.

When considering axisymmetric flow, a particle near the axis has some important equations. These equations will be given below without the derivation. The particles will follow the streamlines, in and out of the nozzle, if the velocity of the flow (i.e. Stokes number) and the relaxation time are not high enough. The relaxation time here indicates after how long the particle will follow the flow streamlines again. To focus the particles after they exit the nozzle, this should be considered. For this reason, the relaxation time and the Stokes number are given in eqs. (2.19) and (2.20), respectively. [44]

$$\tau = \frac{\rho_p D_p^2 C_s}{18 \mu f_d} \tag{2.19}$$

In this equation ρ_p, D_p, μ and C_s are the material density of the particle, the diameter of the particle, the viscosity of the fluid and a correction factor for the Stokes law when the particle diameter comes close to the mean free path (λ) and the slip becomes higher, respectively.

$$S = \frac{\tau_0 U_0}{L_0} = \frac{\rho_p D_p^2 C_{s0} U_0}{18 \mu_0 L_0} \tag{2.20}$$

In this equation U_0 and L_0 are the characteristic flow velocity and the characteristic length, respectively. All the other quantities that have a '0' in the subscript are values that are based on upstream conditions, where the particle and fluid flow are in equilibrium.

This means that if the Stokes number is (much) smaller than one, the relaxation time will also be very small and thus the particles will follow the streamlines instead of their own path. However, if the Stokes number is increased (much) above one, the relaxation time will be high and the particle will less likely follow the streamlines and will follow their own path.

The parameter C_s given in eqs. (2.19) and (2.20) is defined in eq. (2.21).

$$C_s = 1 + Kn_p \left[A + Q \exp\left(-B/Kn_p \right) \right] \tag{2.21}$$

In this equation Kn_p is the particle Knudsen Number as given in eq. (2.22) and A, B and Q are constants [44, 47].

$$\mathrm{Kn}_{p0} = \frac{\lambda_0}{D_p} \tag{2.22}$$

The particle Knudsen number is a ratio of the mean free path length in the system to the particle diameter. This is a dimensionless number. The Knudsen number is directly related to the pressure. To have a high Knudsen number, the mean free path should be increased. This could be achieved by using a vacuum chamber.

More interesting dimensionless numbers to look at, when considering particles in a flow, are the Reynolds number and Mach number. The Reynolds number foresees the patterns in a fluid's behaviour. This number can also be explained as the ratio of the inertial and viscous forces. This number is then used to check whether the flow is laminar (orderly) or turbulent (chaotic and random). When considering high Reynolds numbers ($\mathrm{Re}_{p0} > 2000$) the inertial forces are then much higher than the viscous forces, which will results in a turbulent flow. Looking at low Reynolds number ($\mathrm{Re}_{p0} < 10$) it is seen that the viscous forces are more dominant and will result in laminar flow. [48] Turbulent flow is

not desired when focusing particles. This Reynolds number can be related to the particle or the flow and are given in eqs. (2.23) and (2.24), respectively.

$$\text{Re}_{p0} = \frac{\rho_0 |\mathbf{U_0} - \mathbf{U_p}| D_p}{\mu_0} \tag{2.23}$$

In this equation $|\mathbf{U_0} - \mathbf{U_p}|$ is the relative velocity. They Reynolds number for the flow is similar to the particle Reynolds number (eq. (2.23)) and is given by eq. (2.24).

$$\text{Re}_0 = \frac{\rho_0 \mathbf{U_0} D_H}{\mu_0} \tag{2.24}$$

The Mach number gives the ratio of the flow velocity (v) and the local speed of sound (a). This number relates to the speed and thus again relates to how well the particles will follow the streamlines. This then relates to the focusing of the particles. The Mach number is given in eq. (2.25). [49]

$$\text{Ma} = \frac{v}{a}, \quad \text{with } a = \sqrt{\kappa R T} \tag{2.25}$$

The parameters κ, R and T are the isentropic coefficient, (ideal) gas constant and temperature of the gas, respectively. For monatomic gases (e.g. He) κ is 1.67 and for diatomic gases (e.g. nitrogen) this isentropic coefficient is 1.4. [49, 50, 51]

It is important to notice that eqs. (2.20), (2.22), (2.23) and (2.25) are dependent of each other. When the mean free path is large, the velocity of the particles can also be higher. Thus a higher Knudsen number could result in a higher Stokes number. When considering the Mach number, it is noticed that a higher value would result in higher particle speed. This again results in a higher Stokes number and thus will affect the focusing of particles.

The Knudsen, Mach and Reynolds numbers are related by eq. (2.26). [52]

$$\text{Kn} = \frac{\text{Ma}}{\text{Re}} \sqrt{\frac{\gamma \pi}{2}} \tag{2.26}$$

In this equation γ is the ratio of specific heats.

2.4 Mach disk and collection efficiency

After the particles are focused as explained in previous sections, they need to exit the nozzle and be deposited on a substrate.

The upstream (p_1) and downstream (p_2) pressures are the pressures entering the nozzle and after the nozzle, respectively. This pressure difference is one of the main factors that determines the velocity in a nozzle. The minimum downstream pressure for a subsonic flow is given in eq. (2.27).

$$\frac{p^*}{p_1} = \frac{2}{\gamma + 1}^{\frac{\gamma}{\gamma - 1}} \tag{2.27}$$

In this equation p^* is the minimum downstream pressure for subsonic flow and γ is the material dependent heat capacity ratio of the gas.

Placing a substrate at the nozzle exit, causes a stagnation region to be create, as shown in fig. 2.2.
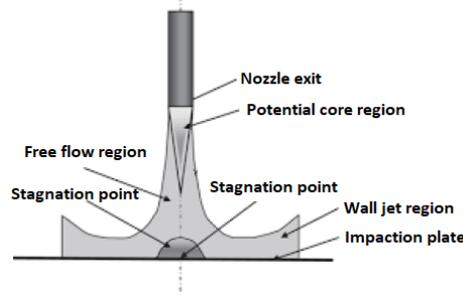
Figure 2.2: Schematic representation of the important components after a nozzle exit. [53]

The stagnation points indicates where the velocity of the gas is zero. The flow lines split and move around the substrate at this region. The gas velocity through the nozzle determines the stagnation region size. There are sharper flow bends for higher velocities, resulting in a smaller stagnation region.

Mach disks are formed after the nozzle exit. This is a very important part of the flow expansion. The distance of this disk is calculated using eq. (2.28). [54]

$$L_m = 0.67 d_n \sqrt{\frac{p_1}{p_2}} \tag{2.28}$$

L_m indicates where the first Mach disk is generated, d_n is the nozzle throat diameter. These disks continue with the same interval, but they become weaker until the flow loses too much energy. The characteristics of this Mach disk after the nozzle are shown in fig. 2.3.
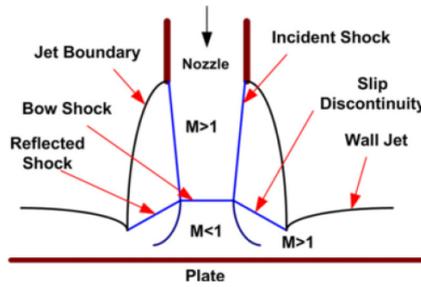

Figure 2.3: Schematic representation of the important components after a nozzle exit. [55]

It is seen that, close to the substrate, a bowshock is formed. A stagnation area is formed behind this bowshock. Wall jets are the flow parallel to the substrate. If the pressure ratio in eq. (2.27) is larger than the pressure ratio between the stagnation area and the surrounding, the wall jets reach sonic velocities.

The successful deposition of these particles in a flow is described by the collection efficiency. When considering the collection of aerosol particles impaction is defined as a special case of curvilinear motion [56]. The same principle applies for all inertial impactors. The aerosol passes through a nozzle and when exiting this nozzle it is aimed at a substrate. This substrate is referred to as impaction plate. The streamlines are bended by an abrupt 90° because the flow is deflected. This is shown in fig. 2.4

If the inertia of a particle is high enough, it will not be able to follow the streamlines and will impact on the impaction plate. If it is assumed that the particles will adhere
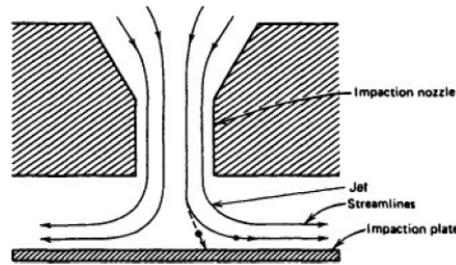
Figure 2.4: Streamlines are bended because the flow is deflected after the exit of the nozzle. [56]

to this plate after impaction, it can be stated that the smaller particles will follow this (90°) streamline and will not hit this plate, due to their small relaxation time. When considering this, it is possible to explain an impactor as a unit that seperates particles in two size ranges. The first range are the particles that have a (sufficiently) high inertia and these particles will be removed from the airstream. The second range are the particles that have too low inertia and will stay in this airstream and will avoid the impaction plate. [56]

When considering the impaction theory a curve can be made that explains the collection (impaction) efficiency versus particle size. This curve is shown in fig. 2.5. The collection efficiency mainly is determined by the Stokes number as showed in section 2.3. [56]
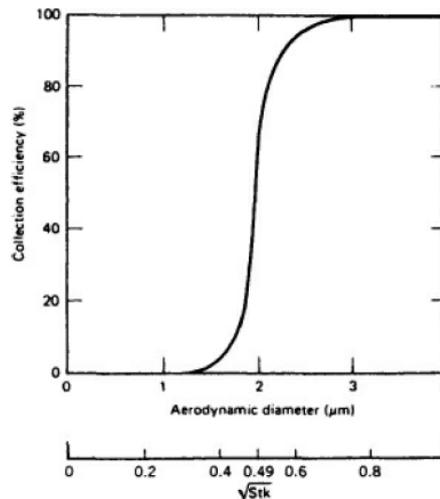

Figure 2.5: Impaction efficiency versus particle size. [56]

Fernandez de la Mora et al. [57] showed that the collection efficiency η versus the nozzle-to-plate distance divided by the particle diameter $\frac{L}{d_n}$ does not show any remarkable degradation when the particle diameter is decreased. This behavior is shown in fig. 2.6.

Fernandez de la Mora et al. [57] also concluded that when the nozzle-to-plate distance is small, and thus particles have a very low Stokes number and cannot be captured inertially, the collection efficiency will take a value that is nonzero with minimal values near 6.5%. This result is unexpected, because the subcritical deposition of particles with negligible intertia (small particle sizes) are usually because of diffusion. These Brownian diffusivities are very size dependent, which makes this a very remarkable result. This result can be clarified if the diffusion is turbulent and not Brownian.
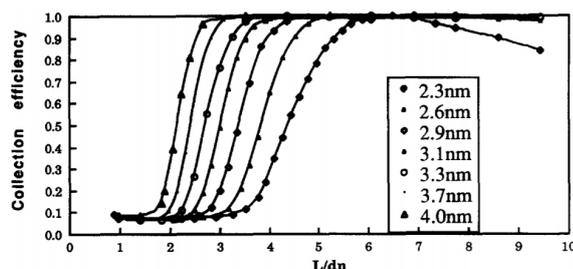
Figure 2.6: The collection efficiency η versus the nozzle-to-plate distance divided by the particle diameter $\frac{L}{d_n}$. [57]

2.5 Different nozzle systems

As introduced in the first chapter of this thesis, designing and using the right nozzle is very important to have good aerodynamic focusing. The equations in previous chapter show that the dimensions are very important to achieve focusing. These dimensions directly translate to the shape and geometry of the nozzle, which makes them a key factor in focusing. The focusing is achieved by designing the nozzle in such a way that the particle divergence at the exit of the nozzle is minimal. Different types of nozzles have been made, using the physics of aerosol discussed in the previous sections, to achieve better focusing. These nozzles are discussed in this section.

2.5.1 Converging nozzle

The working principle of flows through the C nozzle is the basis for the majority of the nozzle systems. This is the reason why the C nozzle will be explained in more detail in this section.

As the word already indicates, a C nozzle decreases in cross-sectional area. Because of conservation of mass, the speed increases when the aerosol flow, that passes through it, enters the smaller cross-section. The aerosol flow has to move faster to maintain a constant amount of aerosol moving through the restricted part of the nozzle. The energy of the random motion of the molecules (pressure) will be converted to faster forward motion, which will result in the increase of the aerosol flow. However, this will then cause a pressure drop in the nozzle. Hence, a C nozzle accelerates subsonic fluids. At the narrowest point (nozzle throat), the flow will reach sonic velocity. However, the pressure ratio has to be high enough to do so. The nozzle is said to be choked if this transition of subsonic to sonic velocity is achieved.

Research done by De la Mora and P. Riesco-Chueca [37] concluded some interesting properties of particles in a flow in a C nozzle. When considering a hypothetical linear flow, it has been found to be that the focus is infinitely sharp. In this type of flow only Stokes values higher than $\frac{1}{4}$ can pass the nozzle axis. Considering symmetrical nozzles, the focus can also be indicated as infinitely sharp when the streamlines are close to the symmetry axis. Defocusing can occur when the streamlines are far from the nozzle centerline, which is due to a geometrical aberration. It has also been shown by De la Mora and P. Riesco-Chueca [37], using numerical examples, that by restricting the region where the particles are flowing into a reasonable angle away from the axis, the width of the focal region can be decreased by the order of two compared to the nozzle diameter. If it is assumed that the jet is exiting through a slit in an infinitely long thin plate, this angle away from the axis

can be taken higher than $\frac{1}{4}\pi$. It is also found that focusing can only occur if the Stokes value exceeds the critical value S^*. This value is usually in the order of unity. The focusing is the least sharp near the critical condition. Here, the geometric-aberration tend to be singular and the focal goes to infinity. Hence, to achieve high-resolution it might be better to stay in the finite distances from the source. This observation could clarify why the previous experiments done by De la Mora and P. Riesco-Chueca [37] had an unassertive degree of focusing. In these experiments the surface that collected the particles leaving the nozzle was hundreds of nozzle diameters away of the source. Since the spatial location of the singularity, where the particles cross the symmetry axis, depends on the relaxation time, varying this point will result in a particle mass spectrometer of great sensitivity and separation power.

Altogether, it has been showed that the particles have to be close to the centerline to be able to achieve good focusing. Also, the distance of the surface that collects the particles should not be too far away.

All these results and findings, made by De la Mora and P. Riesco-Chueca [37], are found by considering idealized examples. These findings are limited by multiple factors, for instance: turbulent mixing at the boundary of the free jet, viscous phenomena on the nozzle walls, the non-linearity of the drag law connecting the two phases, fluid compressibility and the effects of a collecting surface placed on the path of the jet. When considering the sharpness of focusing for very heavy molecules and fine aerosols, the most crucial limiting factor turns out to be diffusion.

Also, Israel and Friedlander stated that, under some flow conditions, the angle of divergence is so small that even well after the nozzle the focusing could stay as small as the size of the tip of the nozzle. [58] However, in this statement it was not taken into account that there might be a collecting surface at the exit of the nozzle. The particles are pushed towards the middle of the nozzle when the inertia of a particle is higher than the drag force that is acting on it. [37]

When designing for a C nozzle, the drag force (Stokes force eq. (2.3)) is the only force that is taken into account. Nevertheless, all the other observations made by De la Mora and P. Riesco-Chueca [37] and Israel and Friedlander [58] should also be considered when designing for such a nozzle.

2.5.2 Converging-diverging nozzle

CD nozzles are often used in rockets and are called 'de Lavel'-type nozzles [59]. First, the flow is subsonic and converges to the minimum area, which is called the throat. The size of the throat chokes the flow and determines the mass flow rate. When considering the throat, it is important to realize that the flow is always set to be sonic, which means that the Mach number is equal to one. After the throat, the nozzle diverges again and the flow isentropically expands to a much higher Mach (and Stokes) number. This Mach number could reach supersonic values and depends on the area ratio of the end of the diverging part to the throat. The static pressure and temperature decreases from the end of the diverging part to the throat due to the expanding of the supersonic flow. The temperature at the end of the diverging part determines the speed of sound at this point, this then determines the velocity at the end of the diverging part. This velocity, pressure and mass flow through the nozzle then will determine the thrust that is produced by the nozzle. Hence, to achieve a (sub)sonic flow a C nozzle will be used and for a supersonic flow a CD nozzle will be preferred.

Each cross section (A) in the nozzle can be calculated with eq. (2.29).

$$\frac{A}{A^*} = \mathrm{Ma} \left[\frac{2}{\kappa + 1} + \frac{\kappa - 1}{\kappa + 1} \mathrm{Ma}^2 \right]^{-\frac{\kappa+1}{2(\kappa-1)}} \tag{2.29}$$

In this equation A^* is the minimum cross section of the nozzle (i.e. the nozzle throat).

When designing for the CD nozzle, the drag force (Stokes force eq. (2.3)) is only taken into account. An ideal CD nozzle is shown in fig. 2.7.
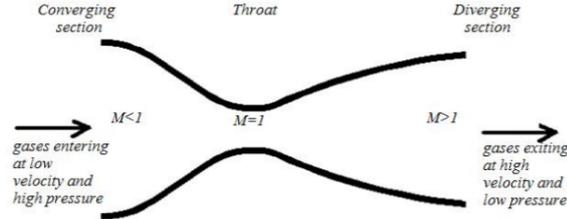

Figure 2.7: A schematic representation of an ideal converging-diverging nozzle. [59]

It has also been found that CD nozzles can be used to produce droplets considerably smaller than the channel it is in. This can be tuned by changing the throat width of these nozzles. The C part of these nozzles have the task to stabilize and accelerate the flow of particles arriving at the junction. When the flow enters the nozzle throat, and thus enters the diverging part, the flow speed starts to decelerate. The pressure difference and the velocity gradient should be maximum at the nozzle throat. This difference results in a section, near the nozzle throat, where the droplets will break. [60, 61] This breaking results in smaller droplets and thus could result in smaller line width, thus higher focusing. This indicates that by scaling this nozzle throat width, the droplet size may be scaled and that the channel width can remain unchanged. Keeping the channel width the same would also result in the flow resistance to almost stay the same. At the same time droplets with sizes of one order smaller than the width of the microchannels which are highly uniform can be made in the flow-focusing microfluidics with a CD section. [62].

2.5.3 Aerodynamic lenses

Usually, to make particle beams a supersonic expansion of a gas with particles in it, it is passed through a nozzle in vacuum. As stated by Xuefeng Zhang et al. [22], the beam of a gas with particles can be focused significantly by passing these particles through AL. These lenses are a construction with axisymmetric subsonic expansions and contractions before the attached nozzle. When designing a device like this, the most important components are the attached nozzle and the AL. This type of focusing uses the fact that the particles are not inertialess. Because the inertia of particles is considered, the gas that passes through subsonic contraction and expansion through an orifice, will not necessarily follow the flow streamlines and thus can converge and focus. Collimation of particles close to the axis will occur if the particles have a displacement towards the axis of symmetry. However, particles may be lost if they impact on the front area of the lens. Xuefeng Zhang et al. [22] found that these two phenomena, collimation and lost of particles, occur when the stokes law is close to unity (St=1). They also found that the diverging of a beam is a function of nozzle geometry, particle Stokes number and Reynolds number. They concluded that a stepped nozzle will help to focus these particles and that the scaling of the particle velocity depends on the speed of sound. Figure 2.8 shows the particle trajectory of different particle diameters through an aerodynamic lens.
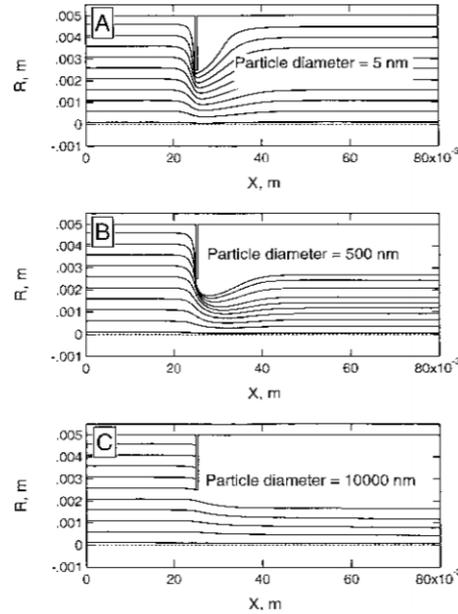
Figure 2.8: A schematic representation of the trajectories of different particles sizes through an aerodynamic lens. [22]

It can be seen that, very little net radial displacement is present in the top plot of fig. 2.8 and that in the lower plot of fig. 2.8 this displacement is much higher. This is due to the fact that if the particles are relatively small, the particle inertia will also be very small and thus the particles will almost completely follow the streamlines. However, when the particles have sufficient particle inertia, they will barely follow the streamlines.

Peng Liu et al. [43] also stated that AL are axisymmetric contractions and enlargements, that create convergent-divergent flow accelerations, to ensure that the particles move closer to the axis as shown in fig. 2.9.
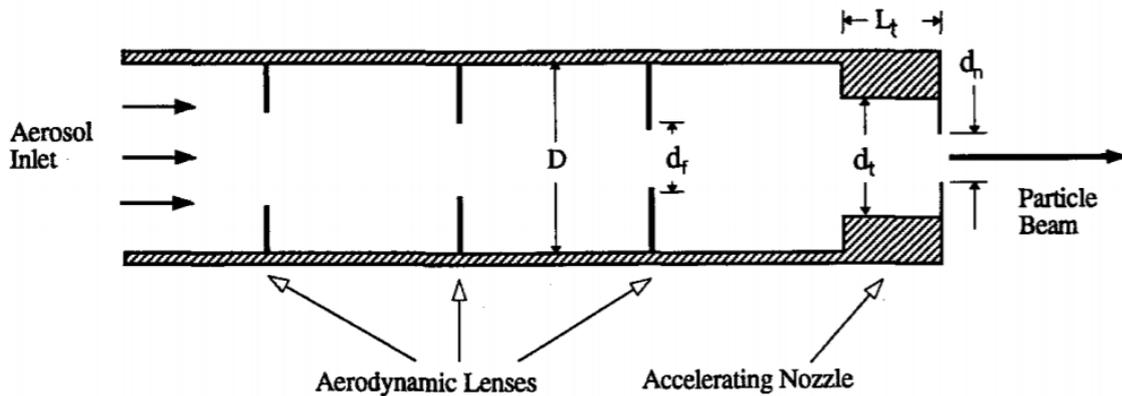

Figure 2.9: A schematic representation of a aerodynamic lenses apparatus. [43]

A gas with particles in it passes through these axisymmetric contractions and enlargements before the nozzles starts to expand. Particles, that have a size smaller than a certain critical value, can be brought closer to the axis and can be kept there by using multiple of these AL. Particles that are close to the axis have low radial drag forces. Hence, they will stay near by the axis and create a small particle beam width downstream. This minimum

27

width is mainly effected by the Brownian motion and the lift forces that are acting on the particles when the nozzle is expanding. Peng Liu et al. [43], used theoretical models and showed that the effects of the Brownian motion are present in all types of particles. However, the lift forces are only present when considering nonspherical particles and are often much more dominating than the effects of the Brownian motion. Thus, using AL could result in remarkable tight and collimated focused particle beams, but is very size dependent.

2.5.4 Converging-diverging-converging nozzle

The CDC nozzle is an elaboration on the CD nozzle. Again, the flow is first subsonic and converges to the minimum area. However, the CDC nozzle has two, instead of one, throats. After the first throat the flow reaches to higher Mach numbers. Using a CDC nozzle the particles are even more collimated and focused around the axis before exiting the nozzle. A typical CDC nozzle is shown in fig. 2.10. [17, 18]
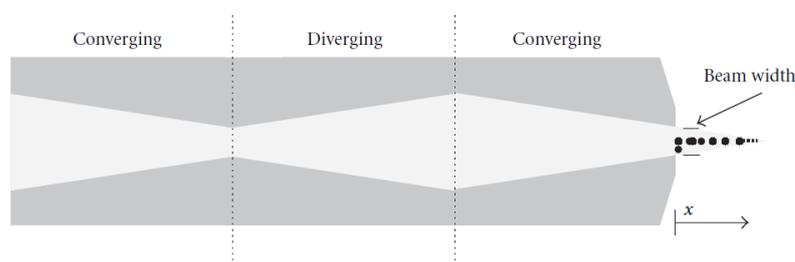

Figure 2.10: A schematic representation of a typical converging-diverging-converging nozzle. [63]

A beam is called collimated when the velocity of the particles are parallel to the axis of the nozzle. This is an optimal and efficient way of focusing the aerosol flow. [64] The idea behind the CDC nozzle is similar to the idea used in the AL [43, 65]. Moreover, CDC nozzles produce narrower collimated beams and less overspray than an AL nozzle. Using collimated beams gives the freedom to use less demanding control systems that control the distance between the nozzle exit and the substrate. Figure 2.11 shows a visual representation on how the collimation of the particles occurs in such a CDC nozzle.
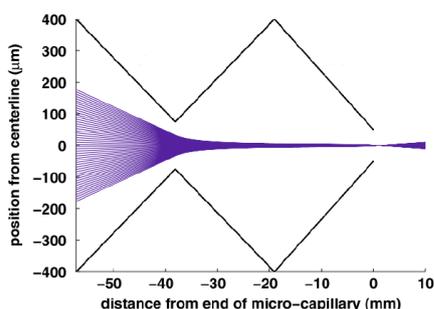

Figure 2.11: Collimation of particles in a typical converging-diverging-converging nozzle. [17]

2.5.5 Capillary nozzle

Akhatov et al. [64], showed the influence of the Saffman force on the dynamics of the fluid when considering aerosol flows through micro-capillaries. When the conditions are correct,

Akhatov et al. [64] concluded that the Saffman force that is acting on the aerosol particles in a gas flowing through a micro-Ca, will cause the particles to migrate to the centerline of the Ca. This is an important observation since the classical aerodynamic focusing only consider the Stokes force and the particle inertia of a gas-particle interaction. When using this method that Akhatov et al. [64] presented, a line width of circa 1 μm could be realised. The flow in this Ca nozzle is a Poiseuille flow. This method is schematically shown in fig. 2.12.
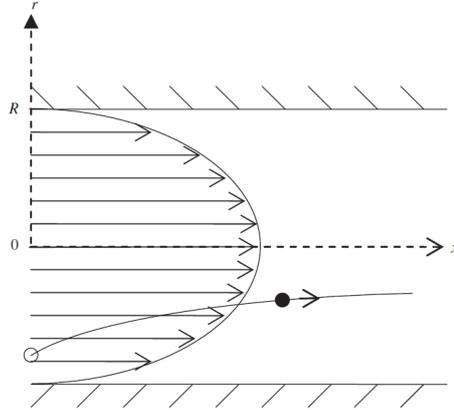

Figure 2.12: A schematic representation of the working principle of a capillary nozzle made by Akhatov et al. [64].

Akhatov et al. [64] showed that when implementing a micro-Ca nozzle in a slightly C nozzle, the streamlines will be inclined to the axis with a relatively small angle and will not be exactly unidirectional. This observation is shown in fig. 2.13.
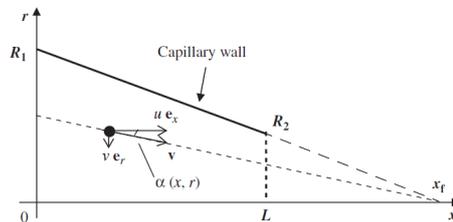

Figure 2.13: Radial and axial velocity of the gas in a capillary nozzle implemented with a slightly converging nozzle. [64]

Akhatov et al. [64] also considered the trajectories of particles when starting at different positions. This is done with both considering the Saffman force and without this force. The results are shown in fig. 2.14

In this plot it was assumed that the particles are only driven by inertia, after they leave the Ca. The particles of the same size then will move to the centerline and will form a focal point next to the tip of the Ca, which is due to the Saffman force and the geometrical convergence of the Ca. The dashed lines in fig. 2.14 shows the geometrical convergence, since the Saffman forces where neglected there and the particles are then only driven by the Stokes drag and inertia. The solid lines, in this plot, show the effect of the Saffman force. Then, the particles are driven by the Stokes drag, inertia and the Saffman force. When comparing the difference of these two results, it can be concluded that the Saffman force has to be taken into account when designing these type of nozzles. If the Saffman force was not accounted for in this case of Akhatov et al. [64] the focusing would
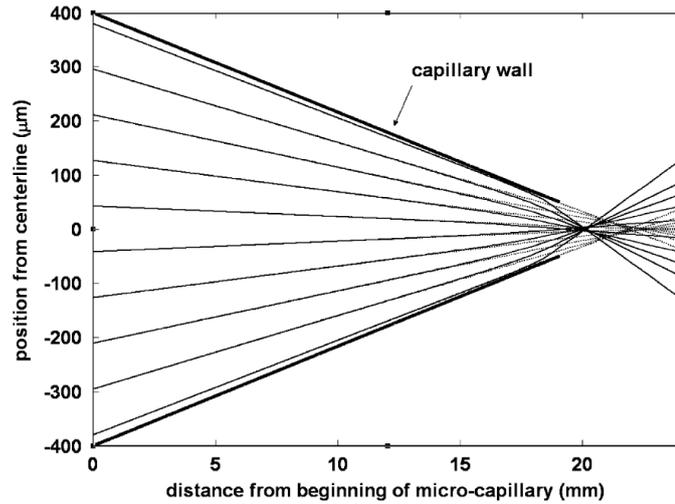
Figure 2.14: The trajectories of particles when starting at different positions. This is done with considering the Saffman force (solid lines) and without this force (dashed lines). [64]

be calculated and modelled to be much better than it actually is. When depositing small particles on a substrate with a micro-Ca nozzle that is slightly C, it has to be taken into account that because of the Saffman force the divergence of the particle trajectories will be a lot faster after the focal point. Hence, the distance between the tip of the micro-Ca and the substrate has to be controlled very accurately. This is hard to realise in practice.

2.5.6 Sheath Gas

Nozzles could implement the usage of SG to force the particles that leave the nozzle to stay near the centerline and thus focus. However, this type of focusing is dependent on multiple factors. Goth et al. [66] stated that the stage speed and the three adjustable flow rates on their instrument affected the width of the lines printed. However, it has to be taken into account that they focused on the number of layers deposited. Furthermore, Mahajan et al. [67] also researched the depending factors of focusing. However, in their study they only focused on the focusing ratio (FR), nozzle size, carrier gas flow rate and stage speed for Aerosol Jet Printing. The focusing ratio in this study is defined as shown in eq. (2.30).

$$\text{Focusing Ratio (FR)} = \frac{\text{Sheath gas flow rate}}{\text{Carrier gas flow rate}} \tag{2.30}$$

Another assumption made is that, nor the ink nor the other conditions are changed. The distance between the nozzle tip and the substrate (working distance) was kept constant at a distance of 2 mm. By testing and experimenting, Mahajan et al. found some relations between the line width and thickness with respect to other factors. It was found that, until a certain point, when increasing the FR the line width decreases. It was also noted that with a increasing FR, the line thickness variations also increases, but that of the line width decreases. This phenomena is shown in fig. 2.15.

Mahajan et al. [67] also found that there is a relation between the nozzle size and the line width and thickness. To find this relation they kept the carrier gas flow rate and stage speed constant at 16 sccm and 2 mm/s, respectively. It was found that smaller nozzles produce smaller line widths and thicknesses (finer lines). This trend is shown in fig. 2.16.
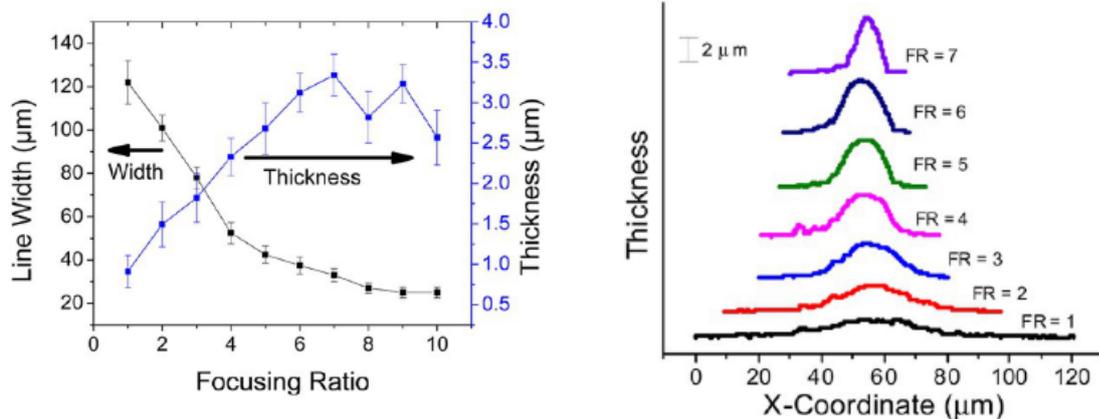
(a) Focusing ratio versus the line width and thickness.

(b) Profilometry scan for different values of the focusing ratio.

Figure 2.15: The dependency of the line width and thickness with respect to the focusing ratio. [67]
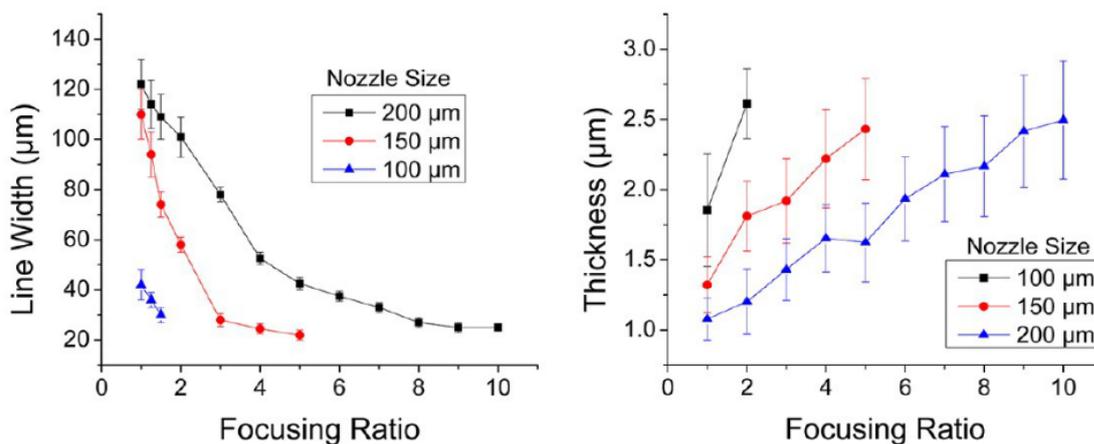
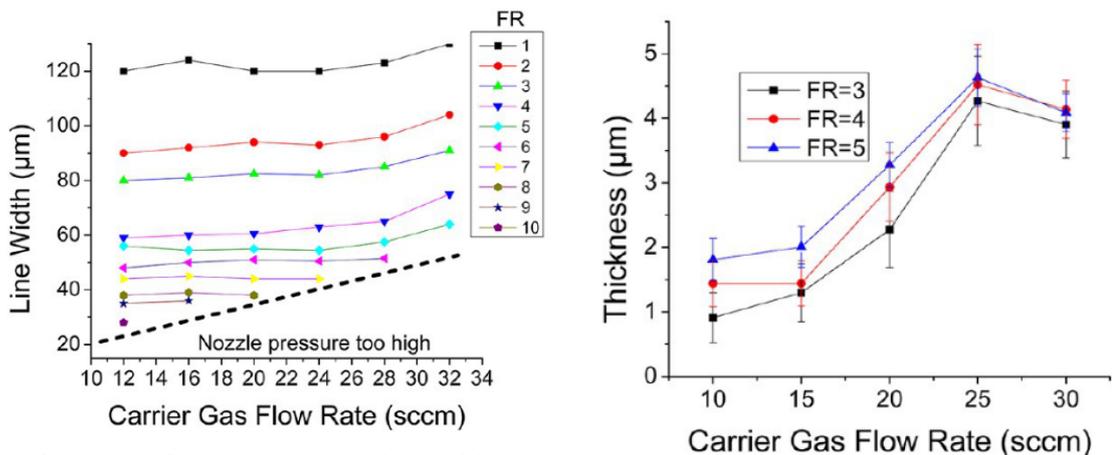(a) Focusing ratio versus the line width while considering the nozzle size.

(b) Focusing ratio versus the thickness while considering the nozzle size.

Figure 2.16: The dependency of the line width and thickness when considering different nozzle diameters. This is done with respect to the focusing ratio. [67]

In these plots the effect of the FR with respect to the line width and thickness is also considered. It was noted that with smaller nozzles the difference in line width is larger when increasing the FR (see fig. 2.16). A drawback of a high FR in a (relatively) small nozzle is that the pressure in these nozzles will be high. Because of this, there is an limitation in the maximum value of the FR in smaller nozzles.

One of the depending factors, that was found by Mahajan et al. [67], is the carrier gas flow rate. However, this can also be considered as the FR, since the line width and thickness depend on the ratio of the SG flow rate to the carrier gas flow rate. This dependency is shown in fig. 2.17.

It is noted that the carrier gas flow rate does not really effect the line width. However, when considering the thickness much more change is seen. At higher carrier gas flow rate
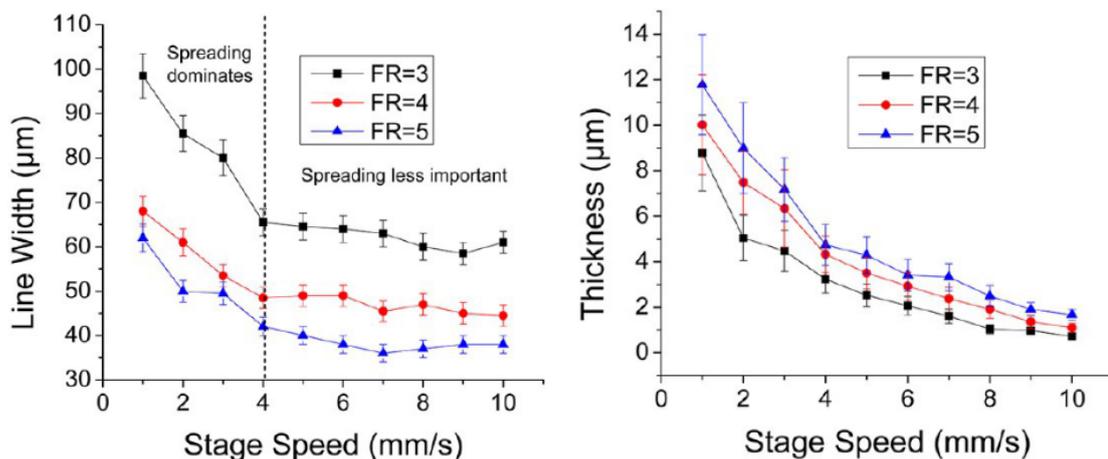
(a) Carrier gas flow rate versus the line width while also considering the focusing ratio.

(b) Carrier gas flow rate versus the thickness while also considering the focusing ratio.

Figure 2.17: The dependency of the line width and thickness when considering different carrier gas flow rates. This is done with respect to the focusing ratio. [67]

the thickness is also seen to be increased. However, since higher carrier gas flow rate means more material deposited, at some point the material will spread and the thickness will decrease. This is also seen in fig. 2.17b. Since the carrier gas flow rate is part of the FR, the same trend is seen when increasing this parameter.

Finally, Mahajan et al. [67] also found another dependency. It has been found that when increasing the stage speed that the line width and thickness will decrease. The FR does not change this trend, it just increases the effect as seen previously. These observations are shown in fig. 2.18.

(a) Stage speed versus the line width while also considering the focusing ratio.

(b) Stage speed versus the thickness while also considering the focusing ratio.

Figure 2.18: The dependency of the line width and thickness when considering different stage speeds. This is done with respect to the focusing ratio. [67]

All in all, it is found that C, CD, Ca and SG nozzles are the best nozzle choices when designing for small particle sizes and a polydisperse flow. This result is used in the proposed nozzle designs as given in chapter 5.

Chapter 3

Modelling

Firstly, this chapter explains the different models and designs that are made. Then, the construction of these models is explained. Hereafter, the model outcome is given by showing which type of results can be extracted from the simulations. Finally, the validation of the models is given.

3.1   Type of models

First, only the shape is studied on a standard C nozzle, as given in section 2.5.1. The three main shapes/geometries variables that are studied on this nozzle, are summarized in the bullet points below. The geometry of a standard C nozzle, with these geometrical aspects, is shown in fig. 3.1.

- The *nozzle exit throat.*

- The *working distance* of the nozzle to the substrate.

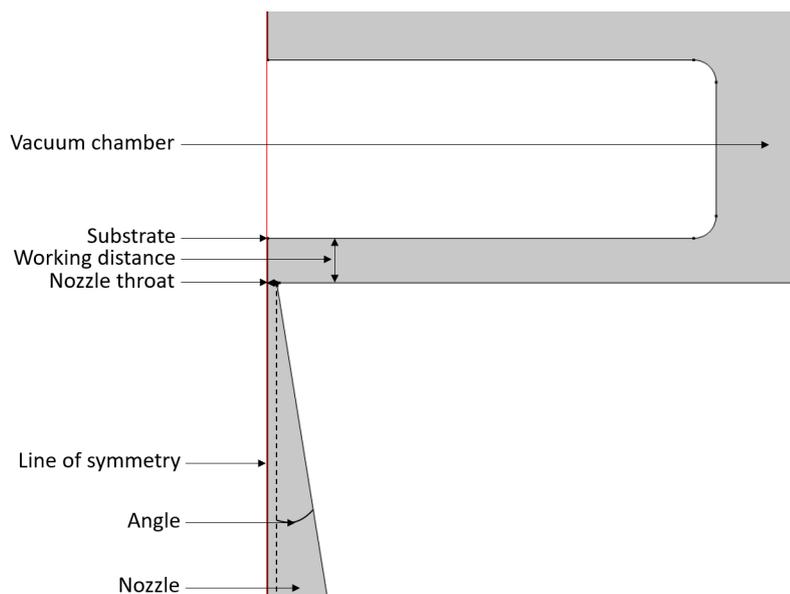- The *angle* at the nozzle exit throat.

Figure 3.1: Graphical explanation of the geometry of a standard (converging) nozzle.

The nozzle exit throat is defined as the diameter of the exit of the nozzle. This diameter is varied and studied. The working distance is the distance of the end of the nozzle to the impaction plate (substrate) where the particles are collected. Finally, when changing the angle, the length of the nozzle also changes. These two variables are studied in one.

The different C nozzle designs are summarized in table 3.1.

Variables	Input variables for Converging nozzle			
	Input 1	Input 2	Input 3	Input 4
Diameter nozzle exit throat	0.4 mm	0.6 mm	0.8 mm	1 mm
Working distance	0.1 mm	0.5 mm	1 mm	-
Angle	10°	15°	35°	50°

Table 3.1: The different inputs of the different studied variables, on a converging nozzle, using COMSOL.

The SLA 3D printer has a minimum printing resolution of about 300 μm. For this reason, nozzle exit throats starting from 400 μm are studied. The working distance is set by hand, hence this distance cannot be too small. Too large working distances are expected to have worse line width. For this reason working distances from 0.1 mm to 1 mm are studied. Finally, the angle effects the length of the nozzle. To have nozzles not too large or small, angles starting from 10 degrees to 50 degrees are studied.

Furthermore 5 different particle diameters are considered in the model: *100 nm, 50 nm, 20 nm, 10 nm and 5 nm*. So, there are 11 different COMSOL models with $11 * 5 = 55$ different solutions and simulation models to consider.

When considering the CSG nozzle, the the aerosol and sheath gas flow rate ratio and the geometry of this nozzle is studied. The four main variables studied for this type of nozzle are summarized in bullet points below.

- The change in *ratio of the aerosol and sheath gas flow rate* introduced to the nozzle.

- The *nozzle exit throat*.

- The *working distance* of the nozzle to the substrate.

- The *angle* at the nozzle exit throat.

The effect of sheath gas to the system is studied by changing the ratio of the aerosol and sheath gas flow rate. The nozzle exit throat and working distance have the same definition as for the standard C nozzle above. However, when the angle is varied, the length of the nozzle will also change. This effects the position where the sheath gas is introduced to the flow. So, the angle will also be studied to understand the difference of early and late introduction of the sheath gas to the system. The different CSG nozzle designs are summarized and given in table 3.2.

Variables	Input variables for Converging Sheath Gas nozzle					
	Input 1	Input 2	Input 3	Input 4	Input 5	Input 6
Ratio Aerosol flow rate/Total flow rate (A/T)	2/8	3/8	4/8	5/8	6/8	7/8
Diameter nozzle exit throat	0.4 mm	0.6 mm	0.8 mm	1 mm	-	-
Working distance	0.1 mm	0.5 mm	1 mm	-	-	-
Angle	5°	10°	15°	35°	50°	-

Table 3.2: The different inputs of the different studied variables, on a converging sheath gas nozzle, using COMSOL.

The nozzle exit throat, working distance and angle variables have for each input three different aerosol flow rate/total flow flow rate (A/T) ratios inputs. So for example, the 0.4 mm diameter nozzle exit throat model is made for A/T=2/8, A/T=4/8 and A/T=7/8. This is done to be able to study if the effectiveness of the sheath gas changes when considering different geometries. Again, all the models have on their turn also a parametric sweep of 5 different particle diameters. All this results in $6 + (12 * 3) = 42$ different COMSOL models with $42 * 5 = 210$ different solutions and simulations models to consider.

In total there are $11 + 42 = 53$ different COMSOL models made with $55 + 210 = 265$ different solutions and simulation models to consider. All these models will be compared in chapter 4.

3.2 Construction of models

To understand and control the resolution of deposition, the models should provide more information then just on the deposited particles. The information needed is summarized in the bullet points below.

- The *line width* after deposition of the particles.

- The *axial velocity* of the flow and particle.

- The *radial velocity* of the flow and particle.

- The *contraction factor* of the nozzle.

Chapter 2 has shown that the particle velocity, flow velocity and the Stokes Number are very important when considering the path that particles follow. This is the reason why information about the axial and radial velocity of the flow and particle are very important. Finally, the effect inside the nozzle on focusing the particles needs to be known. This is shown by looking at the contraction factor of the nozzle. All this information is also considered for the different particle sizes.

Considering the requirements of the information needed and the programs available, the Finite Element software *COMSOL Multiphysics 5.5* is used. This program should be able to provide all the freedom and information needed to design and study the different types of nozzles. COMSOL is capable of giving the results in data (text files) and graphically.

Within COMSOL different physics modules are available to use. The enumeration below summarizes the physics modules that are used for all the models. Also, this enumeration states these modules in the correct order of addition.

1. High Mach Number flow, k-ϵ (hmnf).

2. Particle tracing for fluid flow (fpt).

The approach used here is, first simulating the flow within and outside the nozzle and then adding the particles to this flow. The use of module number 2 has a specific assumption: *one way interaction*. Since the particle concentration is very low (below 0.1%) and the particle sizes are very small (nanometer range), the particles cannot effect the profile of the flow. Thus, because of the particle concentrations and particle sizes used in this research, these modules can be used and plausible models could be expected.

3.2.1 High Mach Number flow, k-ϵ (hmnf)

First, only the flow is simulated and thus only the module *High Mach Number flow, k-ϵ (hmnf)* is used. For this part of the simulation a stationary solution will be sufficient to calculate the flow in- and outside of the nozzle. The stationary study is used when field variables do not change over time. This type of study is used in a fluid flow to compute the steady flow and pressure fields.

This module is used to model gas flows at high Reynolds numbers (turbulent flow). This module can handle sub- and supersonic velocity magnitudes and turbulent flow in supersonic ranges. This interface solves for conservation of mass, energy and momentum. The standard two-equation k-ϵ model with realizability constraints is used to model the turbulence effects. Wall functions are used to model flow and heat transfer close to the walls. It also supports heat transfer in surface-to-surface radiation as well as in solids.

To be able to simulate the models designed, this interface solves the equations given in eqs. (3.1) to (3.3).

$$\frac{\partial \rho}{\partial t} + \nabla \cdot (\rho \mathbf{u}) = 0 \tag{3.1}$$

$$\rho \frac{\partial \mathbf{u}}{\partial t} + \rho(\mathbf{u} \cdot \nabla)\mathbf{u} = \nabla \cdot [-p\mathbf{I} + \tau] + \mathbf{F} \tag{3.2}$$

$$\rho C_p \left(\frac{\partial T}{\partial t} + (\mathbf{u} \cdot \nabla)T \right) = -(\nabla \cdot \mathbf{q}) + \tau : \mathbf{S} - \frac{T}{\rho} \left. \frac{\partial \rho}{\partial T} \right|_p \left(\frac{\partial p}{\partial t} + (\mathbf{u} \cdot \nabla)p \right) + \mathbf{Q} \tag{3.3}$$

Where, ρ is the density in kg/m^3, $\mathbf{u}$ is the velocity vector in m/s, p is the pressure in Pa, τ is the viscous stress tensor in Pa, $\mathbf{F}$ is the volume force vector in N/m^3, C_p is the specific heat capacity at constant pressure in $J/(kg\Delta K)$, T is the absolute temperature in K, $\mathbf{q}$ is the heat flux vector in W/m^2 and $\mathbf{Q}$ contains the heat sources in W/m^3. $\mathbf{S}$ is the strain-rate tensor, which is calculated using eq. (3.4).

$$\mathbf{S} = \frac{1}{2} \left(\nabla \mathbf{u} + (\nabla \mathbf{u})^T \right) \tag{3.4}$$

The eqs. (3.1) to (3.3) are Navier-Stokes equations for a simple compressible fluid. This interface can handle flow of any Mach number. The Mach number is defined in eq. (3.5).

$$\mathrm{Ma} = \frac{|\mathbf{u}|}{a}, \quad \text{with } a = \sqrt{\kappa R T} \tag{3.5}$$

Where a is the speed of sound in m/s. The parameters κ, R and T are the isentropic coefficient, (ideal) gas constant and temperature of the gas, respectively.

Using these equations, eq. (3.1) should be hyperbolic and eqs. (3.2) and (3.3) elliptic for stationary flow. However, diffusive effects are neglected due to the small particles and the high velocity of the flow. This will result in the entire system of equations to become hyperbolic.

This module also assumes that the fluid is an ideal gas (k=1.667). Density and specific heats are related to the pressure and temperature, by the ideal gas law. To accurately approximate the viscosity and thermal conductivity of an ideal gas, the Sutherland's Law is used. These are given in eqs. (3.6) and (3.7) respectively.

$$\frac{\mu}{\mu_0} = \left(\frac{T}{T_0}\right)^{3/2} \frac{T_0 + S_\mu}{T + S_\mu} \tag{3.6}$$

$$\frac{k}{k_0} = \left(\frac{T}{T_0}\right)^{3/2} \frac{T_0 + S_\mathrm{k}}{T + S_\mathrm{k}} \tag{3.7}$$

Where, μ, μ_0 k, k_0 , T, $T_{\mathrm{k},0}$ and S_k are the, viscosity, viscosity at reference temperature, thermal conductivity, thermal conductivity at reference temperature, temperature, reference temperature and the Sutherland constant, respectively.

All the values are filled in and adjusted correctly to an argon gas with copper particles aerosol. The inlet pressure is set to the inlet pressure of the SAM setup. Since this setup operates at the atmospheric pressure, this parameter is set to be 1 bar (10^5 Pa). The nozzle is mounted in a vacuum chamber, so the outlet pressure is considerably lower. Since the aerosol also is deposited in this chamber, the pressure will be slightly higher than the pressure of an completely closed vacuum chamber. For this reason the outlet pressure is chosen to be set as 100 Pa for the time being. If during the experiments this outlet pressure turns out to be higher, the line widths are expected to have larger values than the model and vice versa.

After adding these parameters, a nozzle is introduced to the model. Since the nozzles are symmetrical, only one half of the 2D model is designed. This decreases the file sizes and the calculation time of the simulation (computational cost). The objects were designed using *Polygons*. The three main parts that are of importance in this model are:

- The nozzle.

- The impaction plate, i.e. the substrate.

- The vacuum chamber where the nozzle and substrate are operating in.

Later on in the process a mesh has to be added to the model to be able to do calculations and simulations with it. These three parts are made using multiple polygons, to have the freedom of adding finer or coarser meshes in the sections where it is needed. An example of a standard C nozzle, substrate and vacuum chamber, is shown in fig. 3.2.
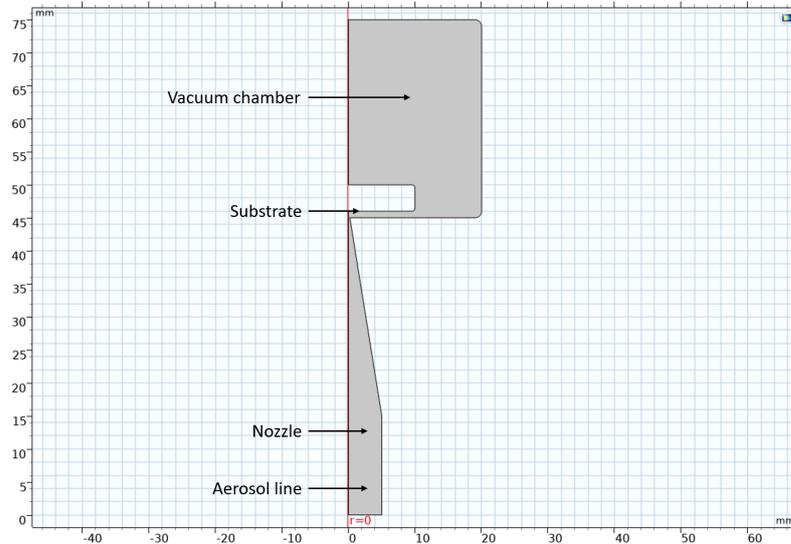
Figure 3.2: An example of multiple polygons used to model a standard converging nozzle, substrate and vacuum chamber.

For the model to work, the initial values and other variable values have to be set. Within the initial values, the pressure is set to 110 Pa and the temperature to 293 K. These are roughly the conditions in the vacuum chamber. The symmetry is set to be at the vertical (zero) axis. The walls of the nozzle, substrate and vacuum chamber are set to have a no slip condition and that nothing can pass through them.

The inlet of the system is chosen as the inlet of the aerosol inlet of the nozzle. The most important values of this inlet are the pressure and Mach Number. The flow is chosen to be a normal inflow.

The outlet is chosen to be at the outlet of the vacuum chamber. The flow is set to be subsonic there and the pressure set to be the outlet pressure as discussed earlier.

Other important values that are used for this module are given in table 3.3.

Variable	Value
μ_{Ref}	2.23e-5 Pa s
k_{Ref}	0.0179 W/(m K)
T_{Ref}	300 K
S_K	166.7 K
M_n	0.03995 kg/mol
γ	1.667
Ma_{Inlet}	0.0011

Table 3.3: Important values used in the High Mach Number flow, k-ϵ (hmnf) module.

To study the designs with this module, a relatively coarse mesh is added to the system first. The system starts calculating at the initial pressure and stops calculating at the final (inlet) pressure. This cannot be done without steps. If the steps are too large, the model will not converge and there will be no final solution and no good simulation of the flow. If the steps are too small, the file will be too large and might not open anymore. A good trade-off needs to be made here by using educated guesses and trial and error. The following educated guess is used for all the models: *120 150 200 250 300 400 range(500,*

1000, 6000) range(7000, 2500, 20000) range(20000, 2000, 100000) Pa. This guess is then fine tuned for each model if necessary.

After solving the first model with the relatively coarse mesh, the mesh is increased to obtain more realistic values. This is also done in steps until the mesh is fine enough that the solution barely changes anymore. Every mesh calculation can be used as initial guess for the finer mesh. Doing the calculation in this way, the computational cost is minimized. The models are computed on the TU Delft Cluster, using *WinSCP*. This allows the models to be computed using 4 Intel(R) Xeon(R) Gold 6150 CPUs at 2.70 GHz (using 4 sockets with 20 cores in total). This is done to reduce the computational time from a few days (on own computer) to several hours (on the cluster) per model. After computing the models, the calculations and simulations for the flow are available for analyzing.

3.2.2 Particle tracing for fluid flow (fpt)

After modelling the flow, the particles are added into it by using the physics module *Particle tracing for fluid flow (fpt)*. The trajectory of the particles can be simulated using COMSOL, since it is assumed that the impact of the particles on the flow is neglibible. This assumption can be made since the particles to be studied are in the nanometer range and the velocity is high. The motion of these particles is defined by Newton's second law, as given in eq. (3.8).

$$m\frac{d^2\mathbf{x}}{dt^2} = \mathbf{F}\left(t, \mathbf{x}, \frac{d\mathbf{x}}{dt}\right) \tag{3.8}$$

Where, $\mathbf{x}$ is the particle position in m, m the mass of the particle in kg and $\mathbf{F}$ is the sum of all forces that are acting on the particle in N. In this module, the particle Reynolds number is defined as given in eq. (3.9).

$$\mathrm{Re}_p = \frac{|\mathbf{u} - \mathbf{u}_p|\, 2r\rho}{\mu} \tag{3.9}$$

Where, $\mathbf{u}$ is the fluid velocity in m/s, $\mathbf{u_p}$ is the particle velocity in m/s, r the radius of the particle in m, ρ the density of the fluid in kg/m^3 and μ the viscosity of the fluid in Pas.

Chapter 2 showed that there are roughly seven forces that act on a particle in a fluid, when modelled as aerosol. However, it was concluded that the main force that will be acting in this system on the particles is the Stokes force, i.e. the viscous drag force. It was also seen that the Saffman force, i.e. the lift force on a particle with local shear, is sometimes large enough to have some influences when accounted for.

As mentioned in chapter 2, the ratio of the Saffman to the Stokes force is given in eq. (3.10).

$$\epsilon_{\mathrm{Sa}} = \frac{|\mathbf{F}_{\mathrm{Sa}}|}{|\mathbf{F}_{\mathrm{St}}|} = \frac{6.46}{12\pi}\sqrt{Re_{\mathrm{p}}} = \frac{6.46}{12\pi}\sqrt{\frac{2a\rho_{\mathrm{m}}|\mathbf{u}_{\mathrm{f}} - \mathbf{u}_{\mathrm{p}}|}{\mu}} = \frac{6.46}{12\pi}\sqrt{\frac{2*(100*10^{-9})*1.784*1}{2.23*10^{-5}}} = 0.0217 \tag{3.10}$$

As can be seen, this force has a larger range of particle size where it is still dominant. However, the particles we are interested in are in the range of 10-100 nm. These particles have a low relaxation time, indicating that the difference in fluid and particle velocity ($|u_{\mathrm{f}} - u_{\mathrm{p}}$) can be assumed to be very small. The particle diameter (a) is also very small.

This leaves us with the following ratio ($\frac{|F_{Sa}|}{|F_{St}|}$) of maximum 0.0217 for 100 nm particles and for 10 nm particles a value of 0.00685. This indicates that the Stokes force is much more dominant in these models. Adding the Saffman force will increase the computational time and file size and add barely any effect. Hence, the Saffman (lift) force is neglected.

The empirical expression for the drag force used in this model is given in eq. (3.11).

$$\mathbf{F} = \pi r^2 \rho \left| \mathbf{u} - \mathbf{u}_p \right| \left(\mathbf{u} - \mathbf{u}_p \right) \left[1.84 \, \mathrm{Re}_p^{-0.31} + 0.293 \, \mathrm{Re}_p^{0.06} \right]^{3.45} \tag{3.11}$$

Since the system is drawn as a 2D axisymmetric object, the particles need to understand that they can pass the axial symmetry and move in all directions freely. The only limitation to the movement of the particles that is induced, are the walls. The system is designed in a way that the particles cannot pass these walls of the nozzle, substrate and vacuum chamber. The SAM setup uses copper electrodes, so the particles in the aerosol are made out of copper with a density of 8960 kg/m^3. Since different (nano)particle sizes are studied, multiple particle sizes are added to the system.

The same in- and outlets are used as in the previous module. The difference is that the particles are added to the inlet part. It is chosen to add 10 same-sized particles to the flow at different radial initial positions. These particles are equally divided over the total width of the inlet of the system. The particles have a velocity due to the flow calculated in the *High Mach Number flow, k-ε (hmnf)* module. If the particles hit the substrate, vacuum chamber wall or outlet, they will adhere to it.

To be able to solve for the particle tracing equations, a time dependent study is computed for this module. This study is used when field variables change over time. In fluid flow, it is used to compute unsteady flow and pressure fields.

In this type of study, the time is defined by using step sizes. These step sizes are very important to achieve the correct models since the particles move over time. If this step size is too large, the particles can ignore the boundaries (walls), and between two steps suddenly be next to the nozzle. Another event that could occur if the step size is too large, is that the particle can deposit at the wrong point. So, the step size should be small. However, if the step size is too small, the computation time will be very high and the files will be too large to run on the computer or even the cluster. A good balance has to be found for each model. This balance is found by using educated guesses and trial and error.

The final results are achieved by using the time dependent study on the second module, which uses the stationary solution of the first module. A parametric sweep is used to model and simulate the particle trajectories of each given particle size independently.

After solving the model on the cluster, the particle tracing is added to the flow. With this model all the information can be extracted that is desired as given in the beginning of this chapter. The different C models, with one in- and outlet, are designed and simulated.

3.2.3 Adding a sheath gas line

To study the effects of sheath gas, another inlet is added to the *High Mach Number flow, k-ε (hmnf)* module. The newly added inlet is the sheath gas inlet and the previous inlet of the model stays as the aerosol inlet. An example of the polygon geometry of the system is shown in fig. 3.3.
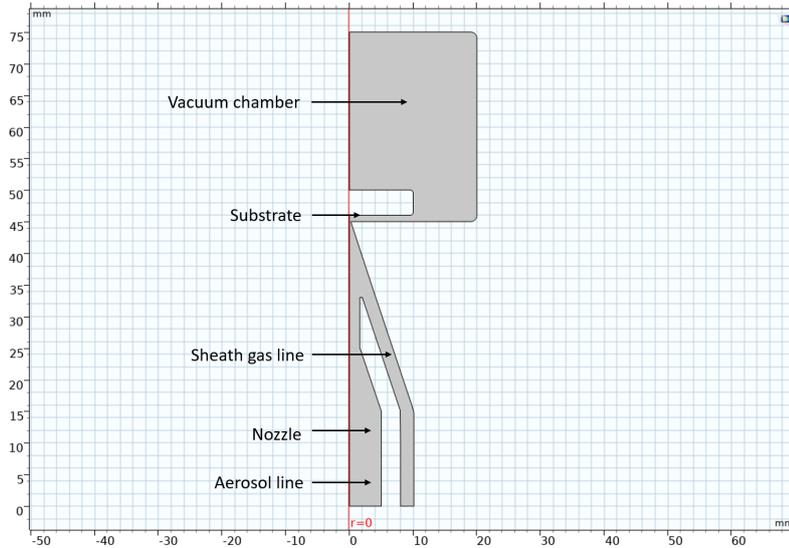
Figure 3.3: An example of multiple polygons used to model a converging sheath gas nozzle, substrate and vacuum chamber.

There is no direct way to add a sheath gas flow rate to the system. Using the volumetric flow rate (Q), as showed in fig. 3.4 and given in eq. (3.12) [68], this problem is solved.
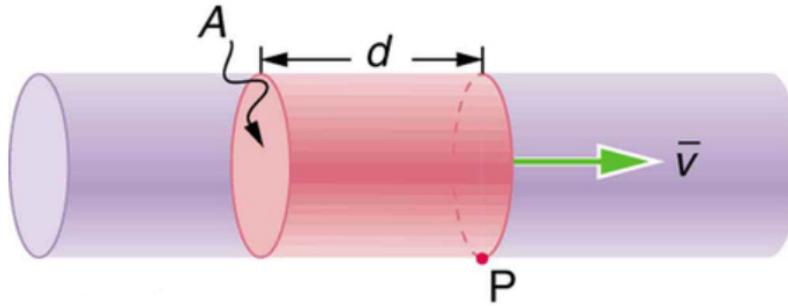

Figure 3.4: A fluid channel to illustrate the volumetric flow rate equation. [68]

$$Q = \frac{V}{t} = \frac{Ad}{t} = A\bar{v} \tag{3.12}$$

The velocity of the flow is calculated using eq. (3.12). This velocity ($\bar{v}$) is then used to calculate the Mach Number, as given in eq. (3.13).

$$Ma = \frac{\bar{v}}{c} \tag{3.13}$$

In this equation c is the speed of sound in argon in m/s. With this equation it is assumed that the pressure and temperature are atmospheric. The aerosol flow rate and the sheath gas flow rate have a maximum total value and thus, there is a trade off between these two values. When adding the correct Mach Numbers to both inlets, the desired sheath gas flow rate is successfully added to the system. A MATLAB script with the exact calculation is shown in appendix A.

3.3 Model outcome

In this section, outcome examples of the C and CSG nozzle models are given.

To achieve good performances, the mesh should be chosen fine enough. If this is not done, the velocity profile and the particle movement are not accurate enough and will not be a good representation of the reality, i.e. the experiments. In figs. 3.5 and 3.6 this phenomenon is shown for the C nozzle. Figure 3.5a shows a C nozzle, modelled using a coarse mesh. The velocity profile after calculating and simulating for this mesh is shown in fig. 3.5b.
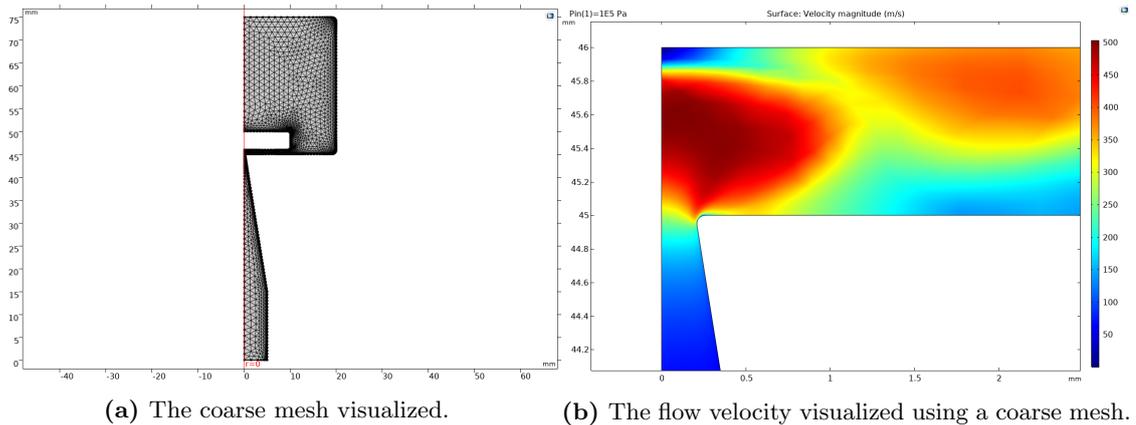

(a) The coarse mesh visualized.   **(b)** The flow velocity visualized using a coarse mesh.

Figure 3.5: A coarse mesh used to model the flow velocity of a converging nozzle in COMSOL.

Figure 3.6a shows the same nozzle but now with a much finer mesh. The velocity profile after calculating and simulating for this mesh, is shown in fig. 3.6b.
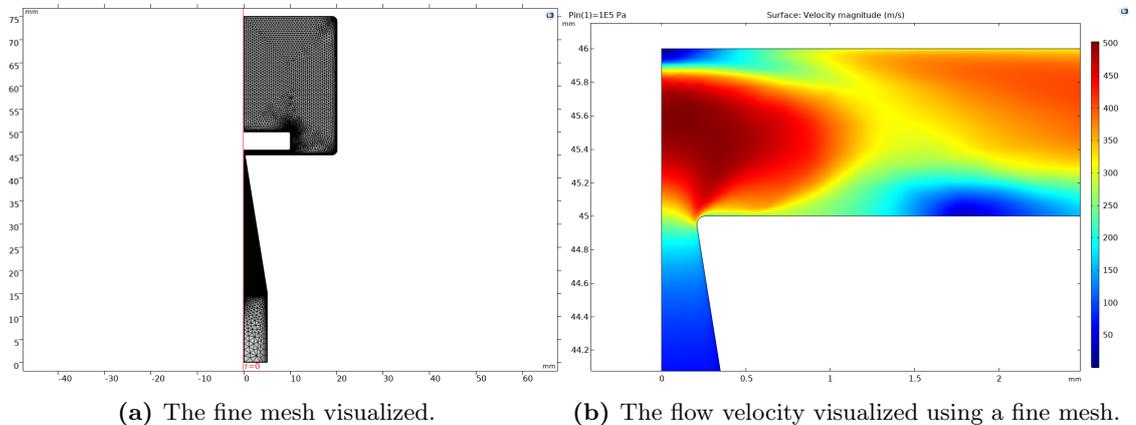

(a) The fine mesh visualized.   **(b)** The flow velocity visualized using a fine mesh.

Figure 3.6: A fine mesh used to model the flow velocity of a converging nozzle in COMSOL.

The finer mesh shows a better velocity profile, although it does not look like much of a difference, these small differences could eventually change the deposited particles significantly. This is mainly due to the small inertia of the particles. The same comparison with the meshes is also done for the CSG nozzle as is shown in figs. 3.7 and 3.8.
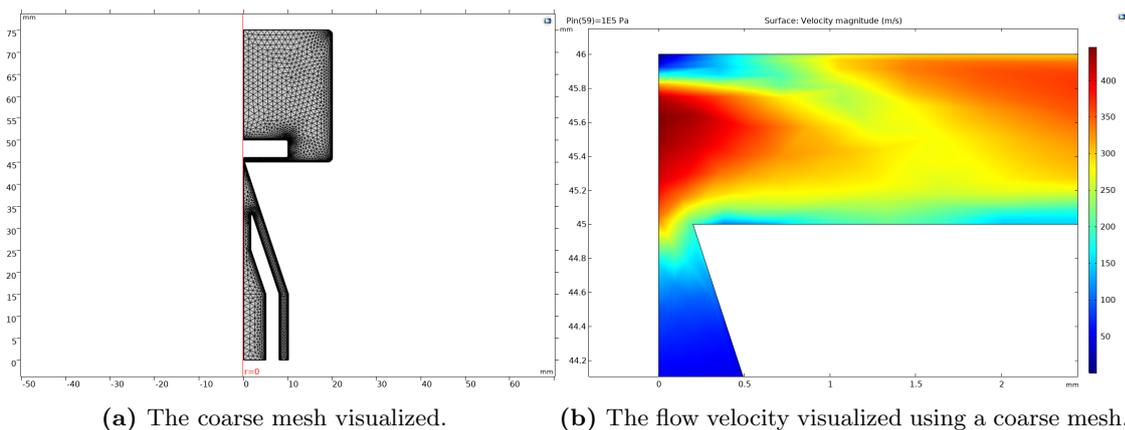
(a) The coarse mesh visualized.

(b) The flow velocity visualized using a coarse mesh.

Figure 3.7: A fine mesh used to model the flow velocity of a converging sheath gas nozzle in COMSOL.

(a) The fine mesh visualized.

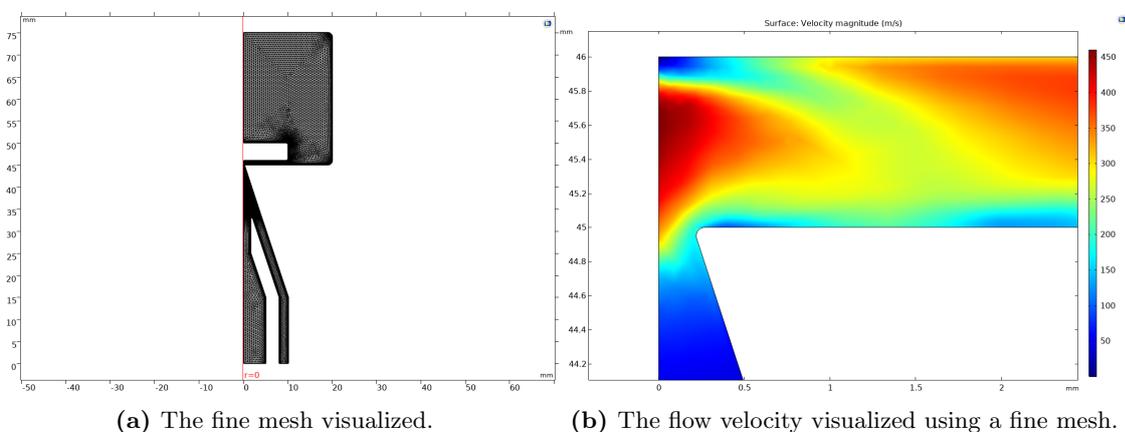**(b)** The flow velocity visualized using a fine mesh.

Figure 3.8: A fine mesh used to model the flow velocity of a converging sheath gas nozzle in COMSOL.

Again, it is seen that the fine mesh shows a better velocity profile than the coarse mesh. For this reason the models are made using fine meshes. It was seen that meshes finer than the shown meshes, do not differ the velocity profile enough anymore to be significant. Meshes as fine as these are used for the models.

To have an idea how the nozzle actually looks like in COMSOL, a 3D model is shown in fig. 3.9. The C nozzle is shown in fig. 3.9a and the CSG nozzle in fig. 3.9b.

The most interesting part to consider, is slightly before and after the nozzle exit throat. A 3D simulation of the flow behaviour in these parts is given in fig. 3.10. The C nozzle is shown in fig. 3.10a and the CSG nozzle in fig. 3.10b.
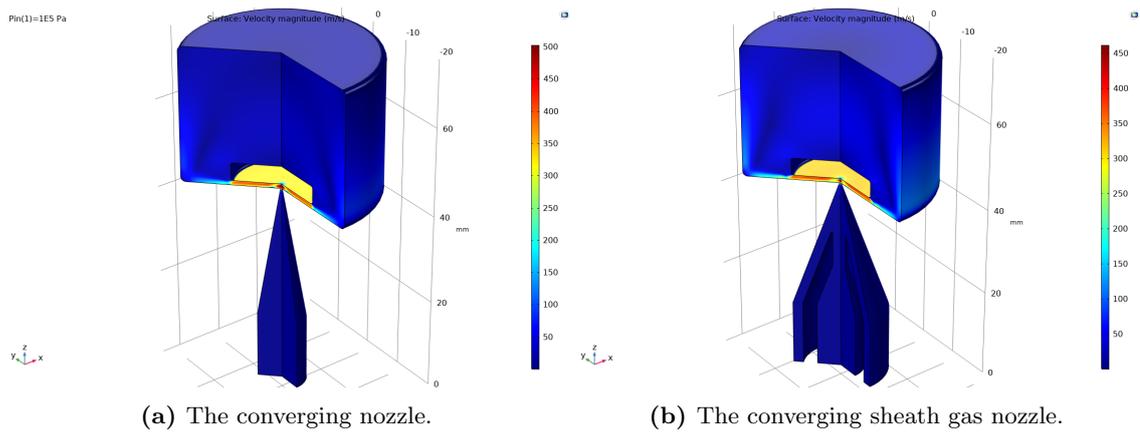
(a) The converging nozzle.

(b) The converging sheath gas nozzle.

Figure 3.9: 3D view of the velocity profiles of the converging and converging sheath gas nozzle.

(a) The converging nozzle.
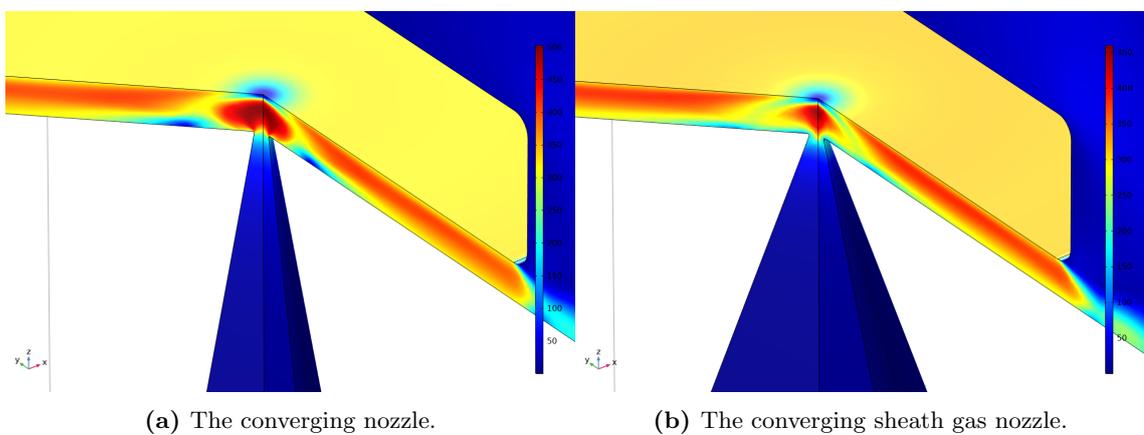
(b) The converging sheath gas nozzle.

Figure 3.10: 3D view of the flow behaviour slightly before and after the nozzle exit throat.

The particle trajectories can be visualized in various ways. Figure 3.11 shows the trajectories of the particles while using a C nozzle. These particles have a diameter of 50 nm. In fig. 3.11a the particle velocity is also shown and in fig. 3.11b the flow velocity is shown.
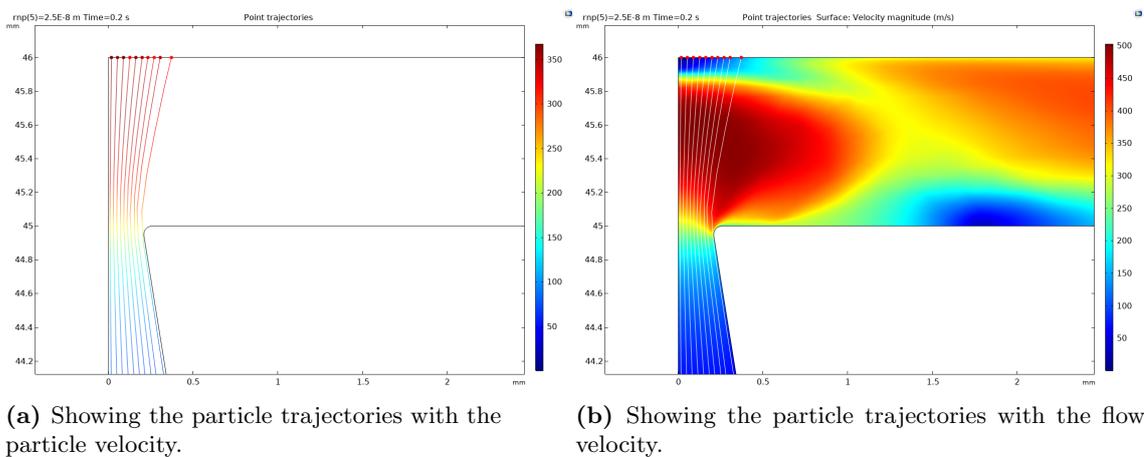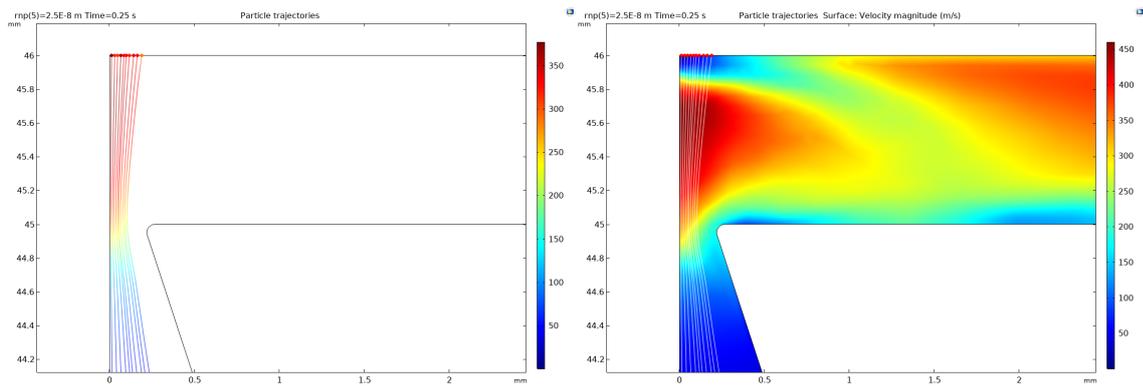

(a) Showing the particle trajectories with the particle velocity.

(b) Showing the particle trajectories with the flow velocity.

Figure 3.11: The particle trajectories using a converging nozzle shown in two ways. These particles have a diameter of 50 nm.

The same is shown for the CSG nozzle in fig. 3.12.

(a) Showing the particle trajectories with the particle velocity.

(b) Showing the particle trajectories with the flow velocity.

Figure 3.12: The particle trajectories using a converging sheath gas nozzle shown in two ways. These particles have a diameter of 50 nm.

The model only shows half of the line width. The correct way to interpret the line width is given in fig. 3.13. For this example, a C nozzle is used with 50 nm diameter particles.
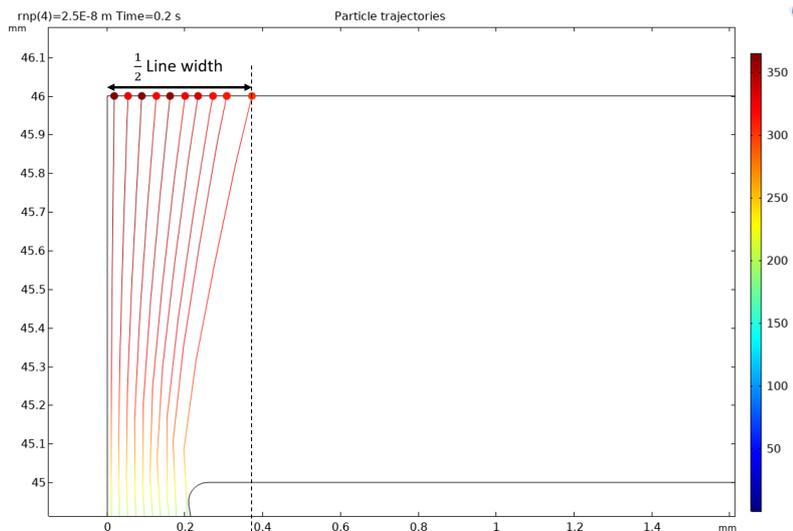

Figure 3.13: Converging nozzle used to explain the interpretation of the line width.

Half of the line width here is approximately 375 microns. The total line width of this example is then 750 microns.

All the examples of the results that are visually given, can also be given in text files. Considering the variety of results that these models deliver, it is concluded that these models are able to provide the information needed as stated at the beginning of this chapter.

3.4 Validation of models

To confirm the validity of the models, the velocity of the flow is checked. Considering all the velocity profiles of the simulated nozzles, it is seen that Mach disks are formed directly after the nozzle exit throat. It is known, from chapter 2, that this observation should always happen. The velocity of the flow suddenly increases at the nozzle exit throat, creating these Mach disks. This indicates that the flow velocity looks correct. To be more sure about this confirmation, the profile of the axial (Z) and radial (R) velocities are considered. These profiles are shown in a graph that shows the velocity from the substrate (0 mm) to inside the nozzle (1-6 mm). This is also done at different distances from the axis of the nozzle (0, 0.1 and 0.2 mm) and is shown in fig. 3.14. This is both plotted for the C and CSG nozzle, as shown in figs. 3.14a and 3.14b respectively.
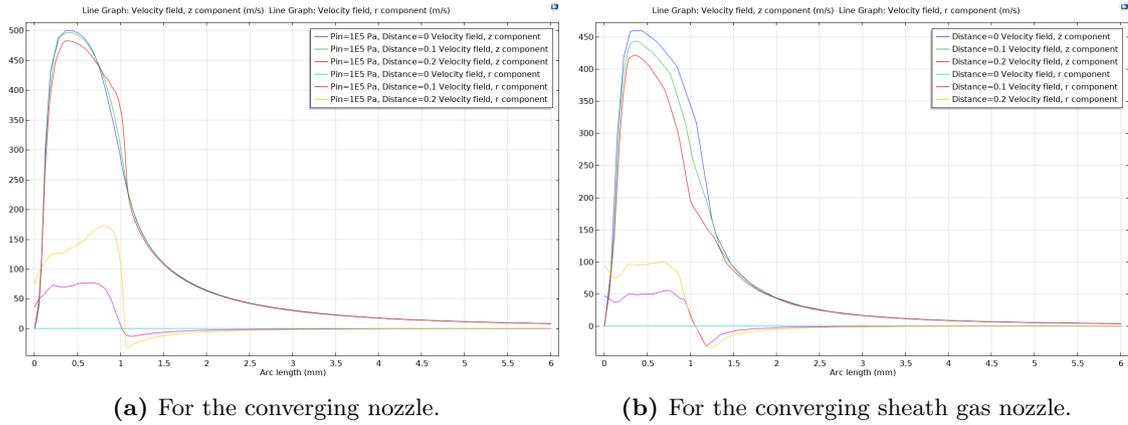

(a) For the converging nozzle. **(b)** For the converging sheath gas nozzle.

Figure 3.14: The z- and r-velocity at different distances from the nozzle axis at the last 6mm before the substrate. The substrate is at 0 mm and the nozzle exit throat at 1 mm, everything after that is in the nozzle.

The upper three lines are the lines corresponding to the Z-velocity and the lower three to the R-velocity of the flow. Considering the particles in the nozzle, it is seen that the particles have relatively low velocities and thus are in the subsonic regime. Close to the nozzle exit throat these z-velocities do not pass sonic levels. The r-velocity is within the nozzle very close to zero since the particles slowly converge towards the centerline and the Stokes force is dominant. This is both for the C and CSG nozzles. Considering chapter 2, it is known that within a nozzle the Mach number can maximum reach sonic levels, so this observation is justly. Another interesting region is between 0 and 1 mm, this is the region where the particles are outside the nozzle. It is seen that the particles reach their highest speeds here (Mach disks). Again, this is both for the C and CSG nozzles. These observation are again corresponding with what is known about these type of nozzles. However, the r-velocity of the CSG nozzle is noticeably lower than that of the C nozzle. This indicates that the sheath gas helps the particles to stay closer to the centerline. This is also an effect that is expected. It can be seen that the velocity is 0 m/s at 0 mm. This makes sense because when the particles are deposited they will not move anymore.

Considering the three different distances shown in the graphs, it is seen that the particles closer to the centerline always have higher velocities than the particles further from this line. This is also a plausible observation, since a Poiseuille flow is expected.

Figure 3.15 shows the typical solution of the C and CSG models, when considering the line width of different particle sizes.
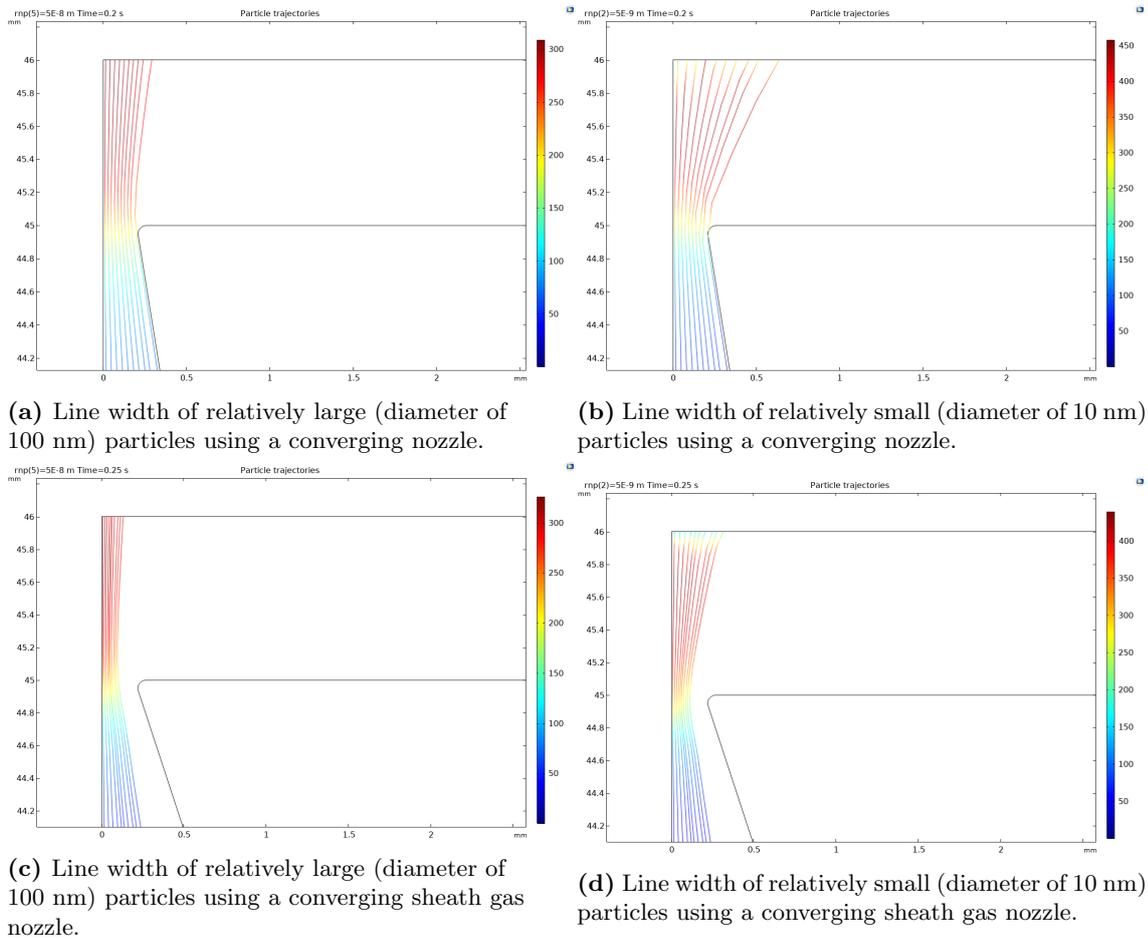

(a) Line width of relatively large (diameter of 100 nm) particles using a converging nozzle.

(b) Line width of relatively small (diameter of 10 nm) particles using a converging nozzle.

(c) Line width of relatively large (diameter of 100 nm) particles using a converging sheath gas nozzle.

(d) Line width of relatively small (diameter of 10 nm) particles using a converging sheath gas nozzle.

Figure 3.15: Typical line widths of relatively large and small particles.

It is seen that larger particles always have a smaller line width than smaller particles. It is known from chapter 2, that larger particles have a higher inertia and relaxation time and thus will less likely follow the streamlines and will stay closer to the nozzle axis. This results in smaller line widths. However, smaller particle have very low inertia and relaxation time and will tend to follow the streamlines. This phenomenon results in larger line widths. Figure 3.15 shows this phenomenon too.

Considering all these arguments and observations, it is concluded that the performance and outcome of these models is validated and are good to model and simulate what will happen during the experiments.

Chapter 4

Modelling results

Firstly, this chapter compares the results of the different model designs of the C nozzle. Hereafter, a comparison of the CSG nozzle designs is given. Then, the C nozzle is compared to the CSG nozzle. This is mainly done by using the focusing ratio. This ratio is defined as the nozzle exit throat over the line width (NT/LW).

4.1 Converging nozzle

The results gathered on the C nozzles are categorized in three main parts: the velocities, the contraction factor and the line width. To study these parts, the nozzle exit throat, working distance and angle (and nozzle length) are adjusted according to chapter 3. All these results are summarized in graphs and given in the sections below.

Velocity

The resulting axial and radial particle speeds, when adjusting the C nozzle, are given in fig. 4.1. These are the maximum speeds measured at the centerline and exit of the nozzles. The values are interpolated, since data at exactly the nozzle exit could not be extracted directly out of COMSOL. The interpolation is done by using the functions *readmatrix* and *spline* in MATLAB. An example of this MATLAB script is given in appendix B.

The difference between the diameter of the nozzle inlet and outlet changes the velocity of the flow and particles. The inlet diameter stays the same, causing the axial particle speed to increase when the nozzle exit throat diameter is decreased, as shown in fig. 4.1a. Smaller particles have higher axial speed, since they have lower inertia and tend to follow the streamlines. This is because the smaller particles have a lower relaxation time and can adjust their velocity to the flow velocity faster compared to the larger particles. However, fig. 4.1b shows that particles with a diameter of 100 nm and 50 nm have a higher radial speed. Since these values are interpolated, they will contain some margin of error. It is expected that this observation is caused during the interpolation. Nevertheless, the radial velocities in the nozzle are still negligible compared to the axial velocities.
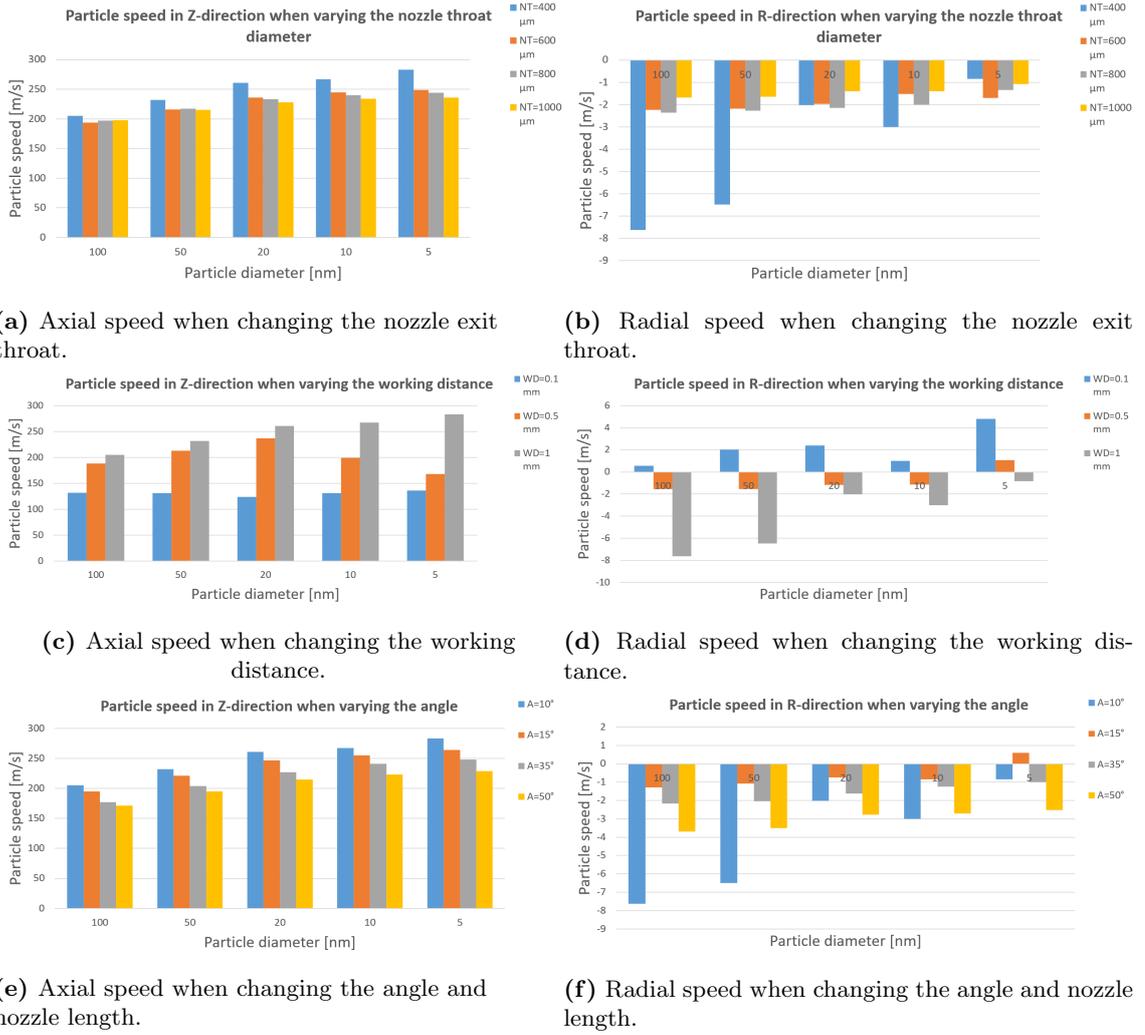
(a) Axial speed when changing the nozzle exit throat.

(b) Radial speed when changing the nozzle exit throat.

(c) Axial speed when changing the working distance.

(d) Radial speed when changing the working distance.

(e) Axial speed when changing the angle and nozzle length.

(f) Radial speed when changing the angle and nozzle length.

Figure 4.1: The particle axial (Z) and radial (R) speeds of different particle sizes when changing different parameters of a converging nozzle. These are the maximum speeds measured at the centerline and exit of the nozzles. The values are interpolated.

If the substrate is too close to the outlet, the particle velocity can not reach high values. It is seen that the axial particle speed increases significantly if the working distance is larger, as shown in fig. 4.1c. This increase is again higher for the smaller particles. Again, the radial particle speed in the nozzle, as shown in fig. 4.1d, is higher for larger particles and negligible compared to the axial speed.

Finally, different angles are studied. When the angle increases, the nozzle itself becomes shorter and vice versa. It is seen that smaller angles have higher axial particle speeds than larger angles, as shown in fig. 4.1e. This is due to the fact that these nozzles with smaller angles are longer, which results in the particles to have more time to reach higher velocities. This effect, again, is even larger for smaller particles. Repeatedly, the radial particle speed, as shown in fig. 4.1f, is higher for larger particles and negligible compared to the axial speed.

Contraction factor

The resulting contraction factors, when adjusting the C nozzle, are given in fig. 4.2.

(a) The nozzle exit throat.

(b) The working distance.
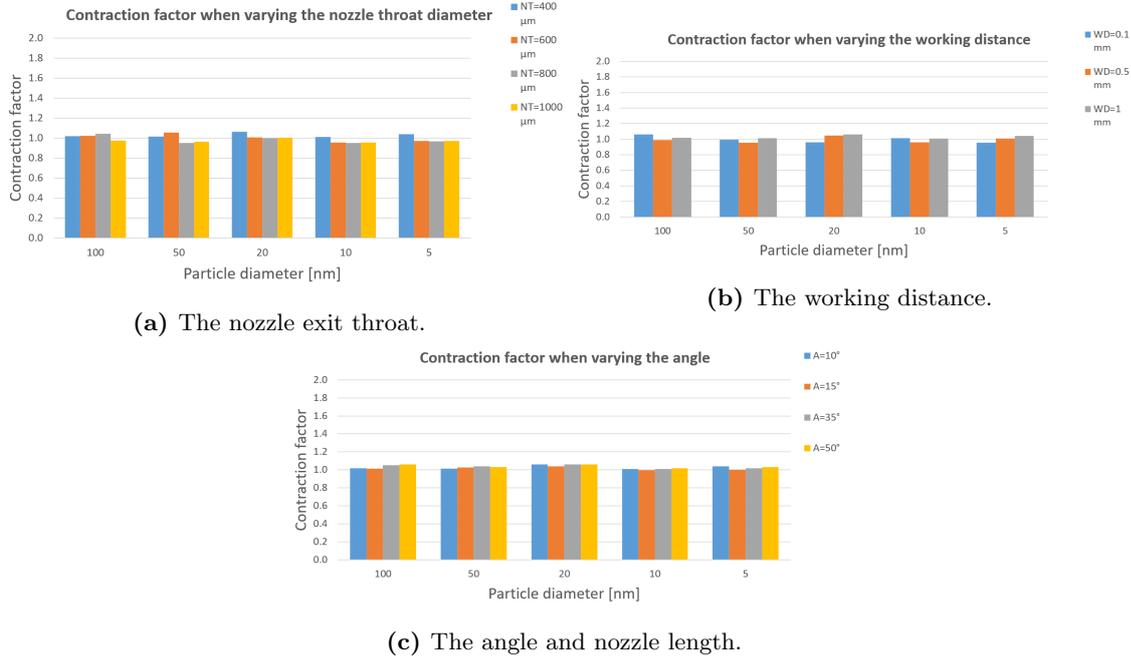

(c) The angle and nozzle length.

Figure 4.2: The contraction factor of different particle sizes when changing different parameters of a converging nozzle.

The contraction factor here is defined as given in eq. (4.1).

$$\text{Contraction factor} = \frac{\left(\dfrac{\text{The distance of the furthest particle from the axis at the nozzle inlet}}{\text{Half the diameter of the nozzle inlet}}\right)}{\left(\dfrac{\text{The distance of the furthest particle from the axis at the nozzle exit throat}}{\text{Half the diameter of the nozzle exit throat}}\right)} \tag{4.1}$$

The contraction factor indicates how well the nozzle system brings the particles towards the centerline. Consequently, higher contraction would result in particles to move more towards the centerline. However, the results, as shown in figs. 4.2a to 4.2c, indicate that all C nozzles have a contraction factor of approximately 1. This means that, all these nozzles do not contract the particles more towards the centerline within the nozzle. This is an unpleasant result for a focusing nozzle. The only element that brings the particles more towards the centerline, is the diameter of the nozzle exit throat. A smaller nozzle exit throat will result in the particles to be closer to the axis when exiting the nozzle, but still have a contraction factor of 1.

Line width

The resulting line widths, when adjusting the C nozzle, are given in fig. 4.3.

Line widths larger than 2500 μm indicate that the particles did not deposit on the substrate. This phenomena only happens when particles are relatively small, i.e. a diameter of 20 nm and smaller. However, when designing the nozzle exit throat smaller, it is seen that these particles are able to deposit on the substrate. Considering the results, as shown in fig. 4.3a, it is seen that smaller nozzle exit throats result in a smaller line widths. This is due to the fact that nozzles with smaller nozzle exit throats result in higher (particle)
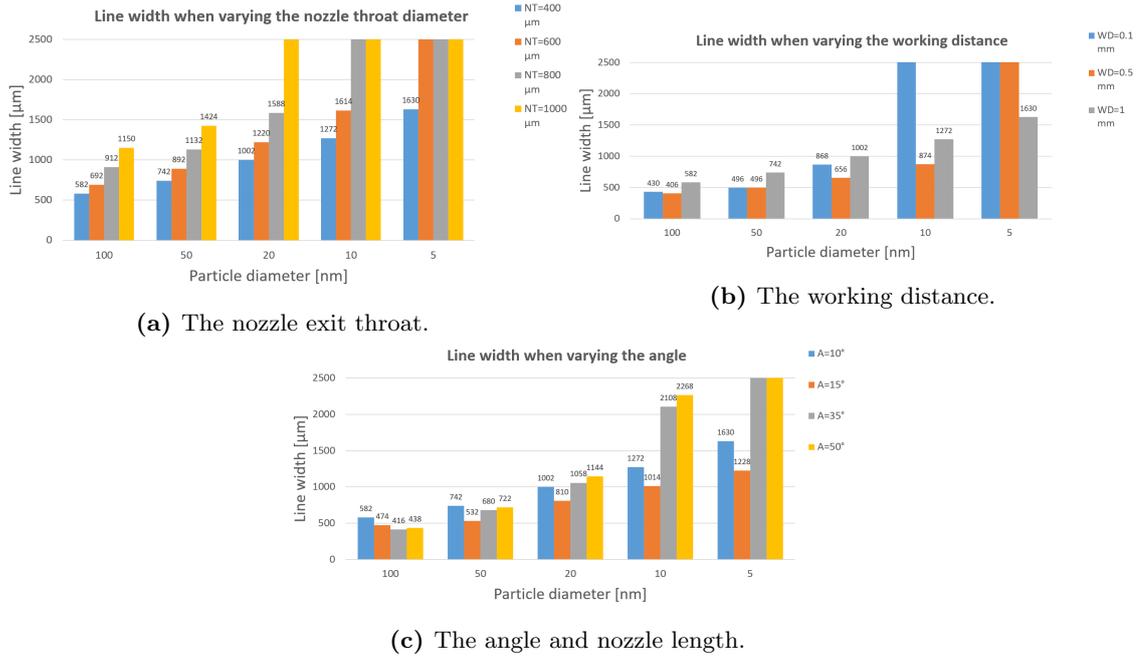
(a) The nozzle exit throat.

(b) The working distance.

(c) The angle and nozzle length.

Figure 4.3: The line width of different particle sizes when changing different parameters of a converging nozzle. Values above 2500 microns indicate that (most of) the particles did not deposit.

velocities and thus higher Stokes numbers. In addition, the particles are already brought more towards the centerline before exiting the nozzle, making it easier to stay focused.

It is seen that the distance of the nozzle to the substrate (working distance) also matters. Very small distances, i.e. 0.1 mm, result in the widest lines, as shown in fig. 4.3b. Moving the nozzles slightly more back to a distance of 0.5 mm, results in much smaller line widths for small particles. However, for particles as small as 5 nm, it is seen that they are unable to deposit. Moving the nozzle to a distance of 1 mm results, for particles of 10 nm and larger, to have wider lines than a distance of 0.5 mm. Particles smaller than 10 nm are able to be deposited with this distance. Considering the results, it is seen that too small working distances results in smaller particles not being able to deposit. Moving the nozzle further away from the nozzle, results in wider lines but smaller particles being able to deposit. This phenomena is due to the fact that the (particle) velocities are higher for a larger working distance. This increases the Stokes number and eventually decreases the line widths.

Figure 4.3c shows that for larger particles the angle does not change the line width much. This difference is much larger for smaller particles. If the angle is too large, i.e. larger than 35 degrees, it is seen that small particles are unable to deposit. Angles of 10 or 15 degrees generally preform the best when considering line widths. This is because these angles have higher (particle) velocities than larger particles. Since the nozzles are longer, the particles have more time to reach a higher velocities within the nozzle.

4.2 Converging sheath gas nozzle

The gathered results for the CSG nozzle are categorized in the same three parts as for the C nozzle. However, unlike for the C nozzle, now the aerosol and sheath gas flow rates are also adjusted. The results of the nozzle exit throat, working distance and angle are only given for A/T=2/8 in this chapter. This is done to keep an clear overview and because these models gave the best results. The results for the other flow rates can be found in appendix C.

Velocity

The resulting axial and radial particle speeds, when adjusting the CSG nozzle, are given in fig. 4.4. These are the maximum speeds measured at the centerline and exit of the nozzles. The values are interpolated using the MATLAB script as shown in appendix B.
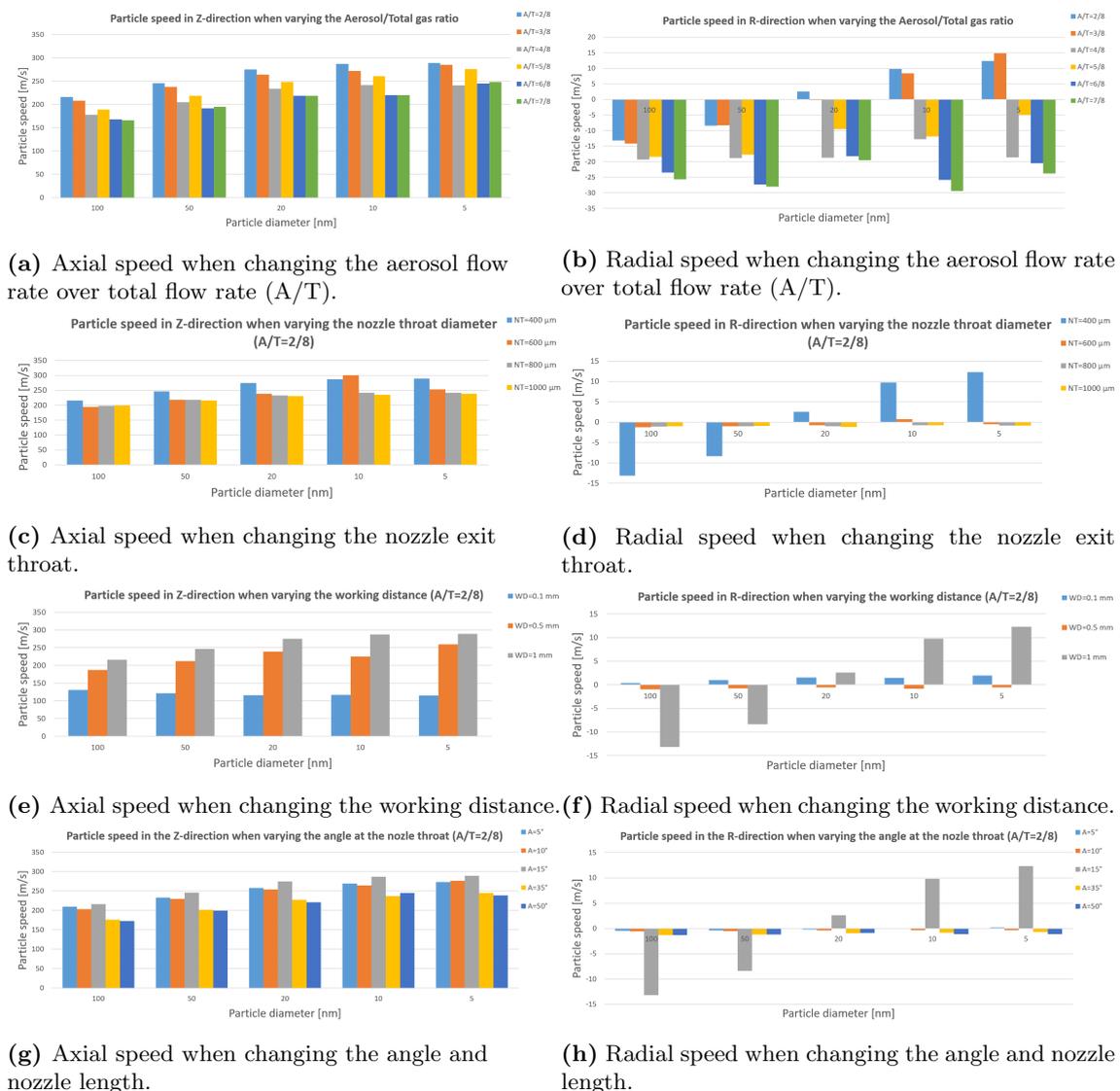

(a) Axial speed when changing the aerosol flow rate over total flow rate (A/T).

(b) Radial speed when changing the aerosol flow rate over total flow rate (A/T).

(c) Axial speed when changing the nozzle exit throat.

(d) Radial speed when changing the nozzle exit throat.

(e) Axial speed when changing the working distance.

(f) Radial speed when changing the working distance.

(g) Axial speed when changing the angle and nozzle length.

(h) Radial speed when changing the angle and nozzle length.

Figure 4.4: The particle axial (Z) and radial (R) speeds of different particle sizes when changing different parameters of a converging sheath gas nozzle. These are the maximum speeds measured at the centerline and exit of the nozzles. The values are interpolated.

When considering fig. 4.4a, it is seen that generally the axial particle speed is higher for lower A/T ratios. A/T=2/8 indicates that the sheath gas has a flow rate of 6/8 of the total flow rate. Thus, higher sheath gas flow rates cause the particles to have a higher axial speed. This higher sheath gas flow rate also causes the radial velocity to be smaller, as shown in fig. 4.4b. This is because the particles are forced to stay close to the centerline.

Figures 4.4c and 4.4d, show that for decreasing nozzle exit throat diameters, the axial and radial speeds are higher. These speeds are also higher for larger working distances, as shown in Figures 4.4e and 4.4f. Smaller angles result in higher axial particle speed, as shown in fig. 4.4g. The particle radial speeds in the nozzle, as shown in Figures 4.4d, 4.4f and 4.4h, can be neglected compared to the axial speeds.

Contraction factor

The resulting contraction factors, when adjusting the CSG nozzle, are given in fig. 4.5.

(a) The aerosol flow rate over total flow rate (A/T).

(b) The nozzle exit throat.

(c) The working distance.

(d) The angle and nozzle length.
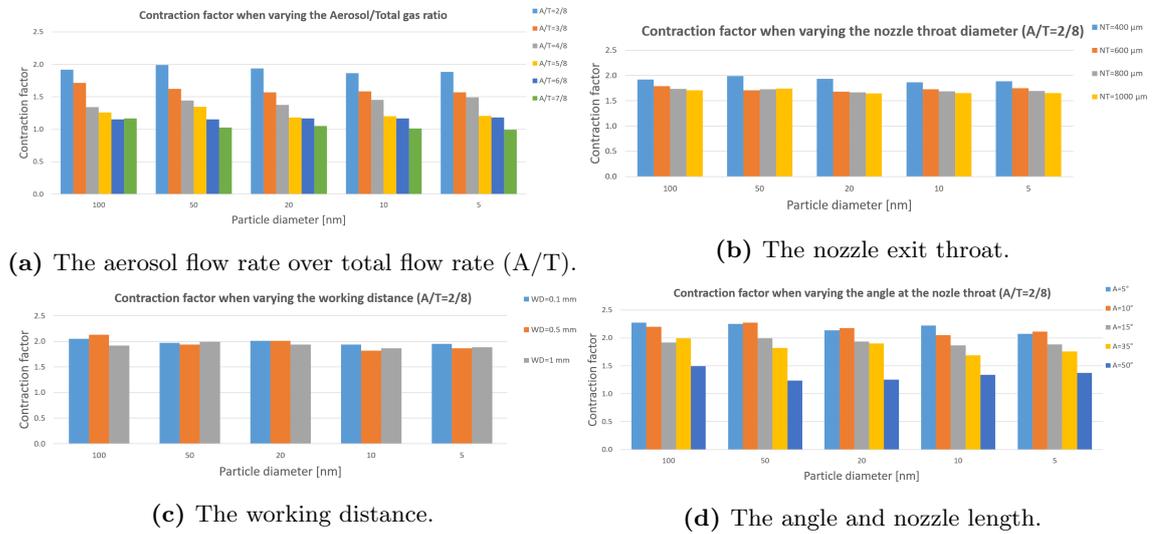
Figure 4.5: The contraction factor of different particle sizes when changing different parameters of a converging nozzle.

According to fig. 4.5a, higher sheath gas flow rates result in a higher contraction factor. This is due to the fact that the sheath gas pushes the particles more towards the centerline and increases the particle velocities. Figure 4.5b shows that the nozzle exit throat diameter does not effect the contraction factor of the nozzle itself. However, the overall contraction factor is lower when the nozzle exit throat is larger. In fig. 4.5c it is seen that the working distance does not effect the contraction factor directly. This indicates that the nozzle does not have to work very close to substrate and can deposit on non-flat surfaces. Smaller angles have a significantly larger contraction factor, as seen in fig. 4.5d. This is caused by the fact that the nozzle is longer when the angle is smaller. Also, the particles have more time to move towards the centerline with a less aggressive change in path.

Line width

The resulting line widths, when adjusting the CSG nozzle, are given in fig. 4.6.

(a) The aerosol flow rate over total flow rate (A/T).

(b) The nozzle exit throat.

(c) The working distance.
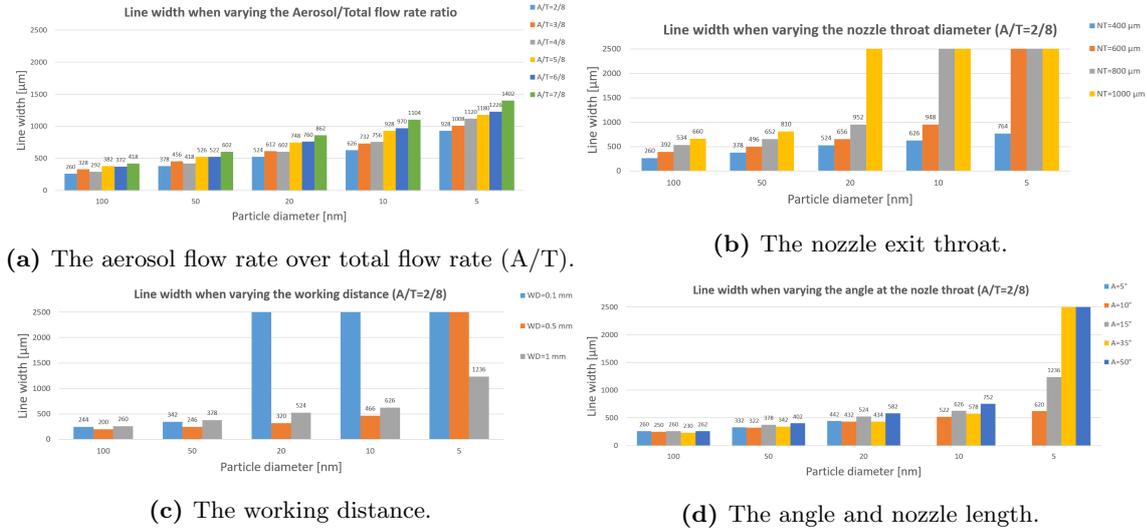

(d) The angle and nozzle length.

Figure 4.6: The line width of different particle sizes when changing different parameters of a converging sheath gas nozzle. Values above 2500 microns indicate that (most of) the particles did not deposit.

Figure 4.6a shows that a higher sheath gas flow rate results in smaller line width. This is due to that the particle velocities are higher for this situation, which results in a higher Stokes number and smaller line widths. Also, it is seen that the contraction factor for this situation is higher, so the particles are closer to the axis before exiting the nozzle.

Figure 4.6b showes that significantly smaller line width can be achieved by reducing the diameter of the nozzle exit throat. It is also seen that small particles, i.e. 20 nm and smaller, can only be deposited on the substrate if the nozzle exit throat is small enough.

The working distance does not change the line width of larger particles much, as shown in fig. 4.6c. However, when considering particles of the size 20-10 nm, the line width is smaller when slightly increasing the working distance. To be able to deposit particles smaller than 10 nm it is seen that the working distance needs to be slightly increased. It is found that for 1 mm working distance, these particles are able to be deposited.

Changing the angle does not effect the line width much, when considering particles larger than 20 nm, as shown in fig. 4.6d. However, for particles smaller than 10 nm, it is seen that having a small angle is necessary to be able to deposit the particles on the substrate with narrow line widths.

4.3 Comparison of the converging and converging sheath gas nozzle

The focusing ratio is defined as the nozzle exit throat over the line width (NT/LW). The focusing ratio of the different A/T ratios is given in fig. 4.7. This is first shown, to conclude what the sheath gas does to the focusing ratio, before adding more changes to the CSG

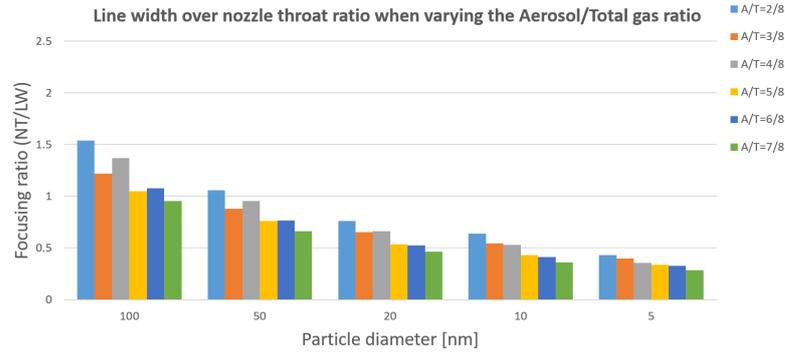nozzle. This makes the comparison between the C and the CSG nozzle easier to explain and understand.

Figure 4.7: The focusing ratios (nozzle exit throat/line width) of different particle sizes when changing the aerosol flow rate to total flow rate ratio of a converging sheath gas nozzle.

Focusing ratios higher than one indicate that the line width is focused to a value smaller than the diameter of the nozzle exit throat. It is observed that higher sheath gas flow rates result higher focusing ratios. Also, the focusing ratios are higher for larger particles than for the smaller ones. These observations are due to the higher particle velocities for higher sheath gas ratios and the larger inertia of the larger particles. Also, the sheath gas forces the particles inside the nozzle towards the centerline, causing the particles to leave the nozzle more collimated.

The focusing ratios of both the C and CSG nozzle are compared to see the differences between both nozzles. Figure 4.8 shows this difference when considering the nozzle exit throat.

(a) The converging nozzle.

(b) The converging sheath gas nozzle.
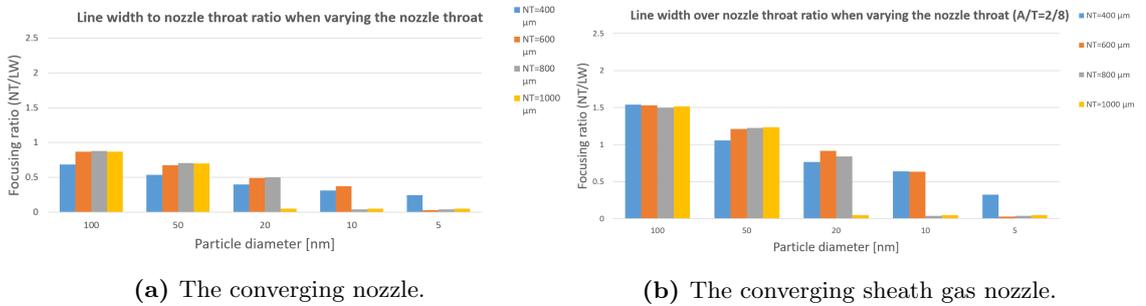
Figure 4.8: The focusing ratios (nozzle exit throat/line width) of different particle sizes when changing the nozzle exit throat of a converging and converging sheath gas nozzle.

It is clearly seen that the focusing ratios of the CSG nozzles, as shown in fig. 4.8b, are much higher than those of the C nozzles, shown in fig. 4.8a. The focusing ratio of the C nozzles never exceed the value of one, indicating always a wider line width than the nozzle exit throat diameter. The CSG nozzles have focusing ratios higher than one. However, for smaller particles this focusing ratio decreases significantly. Larger nozzle exit throat diameters, result in significantly lower focusing ratios for smaller particles. The 400 μm nozzle exit throat shows a significantly higher focusing ratio for particles smaller than 10 nm.

Figure 4.9 shows the difference between the focusing ratio of the C and the CSG nozzle, when changing the working distance.
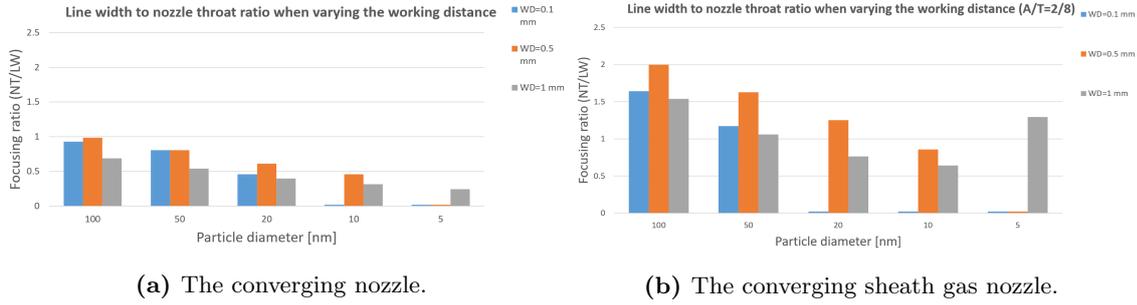

(a) The converging nozzle.

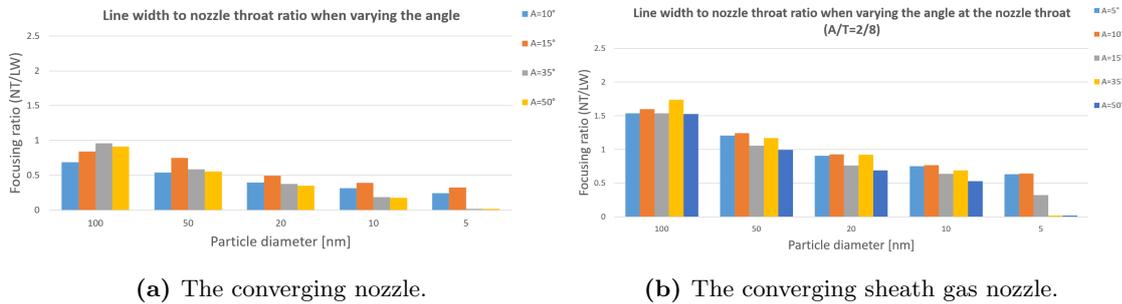

(b) The converging sheath gas nozzle.

Figure 4.9: The focusing ratios (nozzle exit throat/line width) of different particle sizes when changing the working distance of a converging and converging sheath gas nozzle.

Again, the CSG nozzles show much higher focusing ratios, than the C nozzles, as shown in figs. 4.9a and 4.9b, respectively. The C nozzles again fail to pass the value of one considering the focusing ratios. The 1 mm working distance shows, even for the smallest particle sizes, promising focusing ratio values for the CSG nozzles. However, a working distance of 0,5 mm has better focusing ratio for particles larger than 10 nm. All in all, working distances from 0.5 - 1 mm seem very promising to achieve good focusing, using a CSG nozzle.

The focusing ratios of the C nozzle and the CSG nozzle, when changing the angle at the nozzle exit throat, is given in fig. 4.10.

(a) The converging nozzle.

(b) The converging sheath gas nozzle.

Figure 4.10: The focusing ratios (nozzle exit throat/line width) of different particle sizes when changing the angle of a converging and converging sheath gas nozzle.

The C nozzles have much lower focusing ratios than the CSG nozzles, as shown in figs. 4.10a and 4.10b respectively. Again, the C nozzles are not able to pass the value of one considering the focusing ratio, leaving the CSG nozzle again superior to it. It is observed that the focusing ratios of the CSG nozzles stay decent for all particle sizes, when using small angles such as 5-15 degrees.

Overall, these focusing ratios indicate that the CSG nozzles are much better at focusing particles than the C nozzles. Also, it is seen that is very hard to have small line widths with the C nozzle if small particles are deposited. The focusing ratios of the CSG nozzles have in the case of small nozzle exit throats (400 μm) and angles (5-10 degrees) and a working distance of 0.5-1mm decent values. The goal can be reached by designing a nozzle that maximizes the potential of these values. These nozzles are proposed in the following chapter.

Chapter 5

Proposed nozzles

Firstly, this chapter gives the models and COMSOL results of the proposed nozzles. Hereafter, the modifications needed in the SAM setup to implement a sheath gas system, are discussed. Then, the process to print a CSG nozzles is explained. This procedure is then used to print a proposed nozzle. Finally, the experimental results gathered with a C nozzle and the proposed CSG nozzle, are given and briefly compared.

5.1 Models and results

Based on the findings in chapter 4, three nozzle designs are introduced, labeled: Proposed 1, 2 and 3. Proposed 1 is based on the model used in the previous chapter with chosen parameters to be in the most favourable range, as found through modelling. This model is shown in fig. 5.1. Proposed 2 and 3 have a capillary and diverging end, respectively.
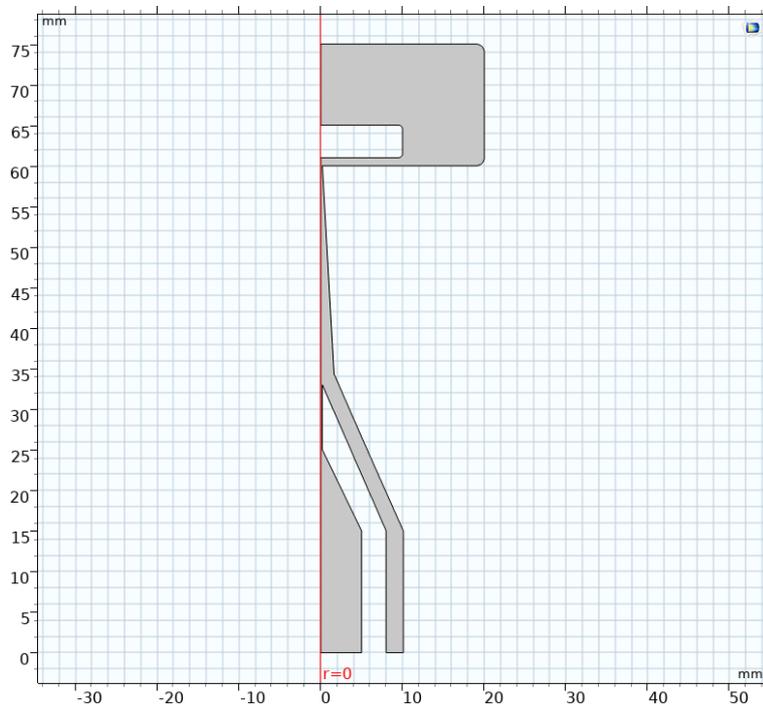
Figure 5.1: Proposed converging sheath gas nozzle design.

This nozzle is set to have a nozzle exit throat of 400 μm, a working distance of 1 mm, an angle of approximately 5 degrees and a total length of 60 mm. Further details about the dimensions and geometry are given in section 5.2.2.

Two other nozzles are designed with this nozzle as the base, as shown in fig. 5.2. Proposed 2 has exactly the same geometry as proposed 1, but has a capillary end at the nozzle exit of proposed 1. The diameter of this part is also 400 μm and has a length of 3mm, making the total nozzle length 63mm. This nozzle is shown in fig. 5.2a. Proposed 3 has also exactly the same geometry as proposed 1, but has a diverging end at the nozzle exit of proposed 1. This diverging part starts at 400 μm and becomes gradually after 5 mm 800 μm, making the total length of this nozzle 65 mm. This nozzle is shown in fig. 5.2b. The capillary part and diverging part at the end were not studied. However, section 2.5 shows that adding a diverging and capillary part at the end will increase the velocity and should cause the particles to migrate towards the centerline, respectively. This should result in narrower line widths. The exact geometries of both nozzles are given in section 5.2.2.
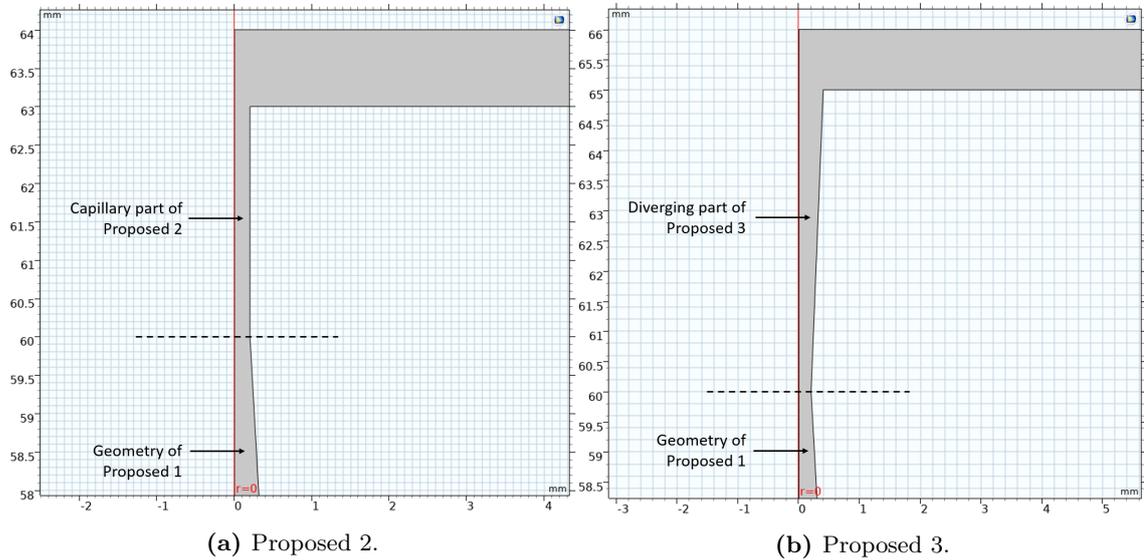

(a) Proposed 2. **(b)** Proposed 3.

Figure 5.2: Geometry difference of proposed 2 and 3.

Chapter 4 showed that the best results, for a CSG nozzle, are achieved when using the ratio A/T=2/8. Hence, all the following results are based on this ratio.

The modelled particle velocities of the nozzles are given in fig. 5.3. These are the maximum speeds measured at the centerline and exit of the nozzles. The values are interpolated.
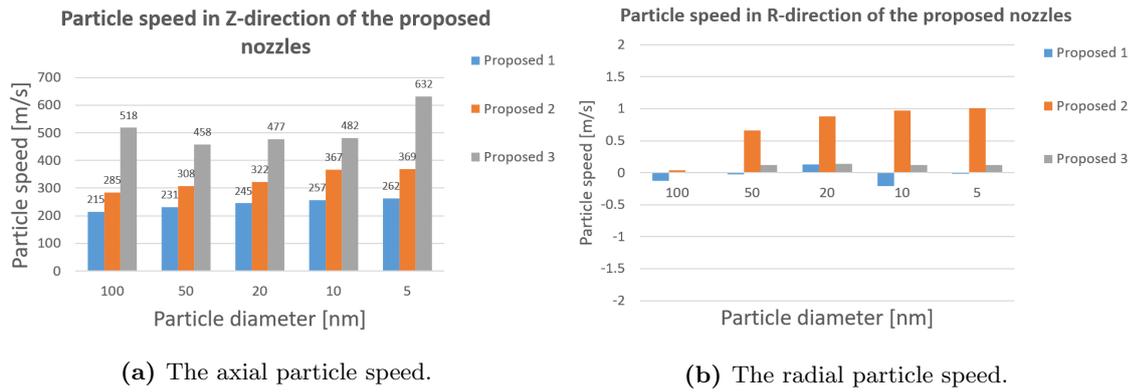
(a) The axial particle speed.

(b) The radial particle speed.

Figure 5.3: The particle axial (Z) and radial (R) speeds of different particle sizes of the proposed nozzles. These are the maximum speeds measured at the centerline and exit of the nozzles. The values are interpolated.

Figure 5.3a shows that proposed 1 has the lowest particle speed of all three nozzles. Adding a capillary end results in an approximately 30% particle speed increase. More than 200% particle speed increase is achieved by adding the diverging end. As mentioned earlier in this chapter, it is expected that adding a capillary and diverging part would result in higher velocities. Figure 5.3b shows the radial speeds. It is seen that the radial speed in the nozzle is neglectable compared to the axial speed.

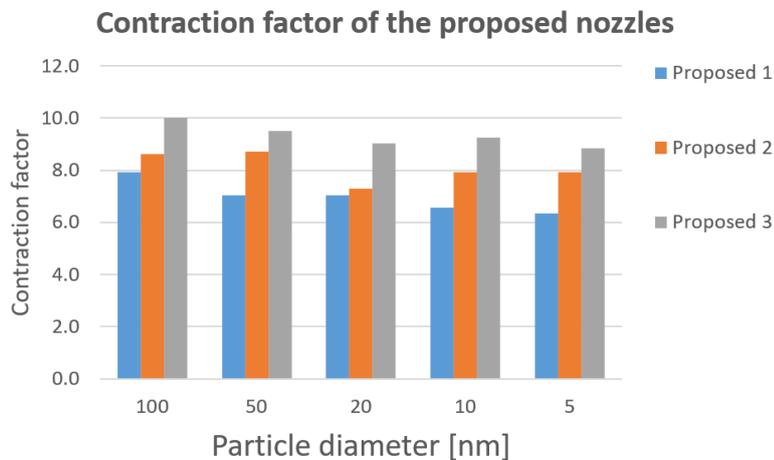The modelled contraction factors of these nozzles is given in fig. 5.4.

Figure 5.4: The contraction factor of different particle sizes of the proposed nozzles.

All three nozzles have excellent contraction factors. Proposed 2 and 3 have slightly better contraction factors than proposed 1. This is due to the higher axial particle speeds of these nozzles. However, the significant higher speeds of proposed 2 and 3 are not proportional to the contraction factor. Proposed 1 has a very good contraction factor given its relatively low axial particle speed.

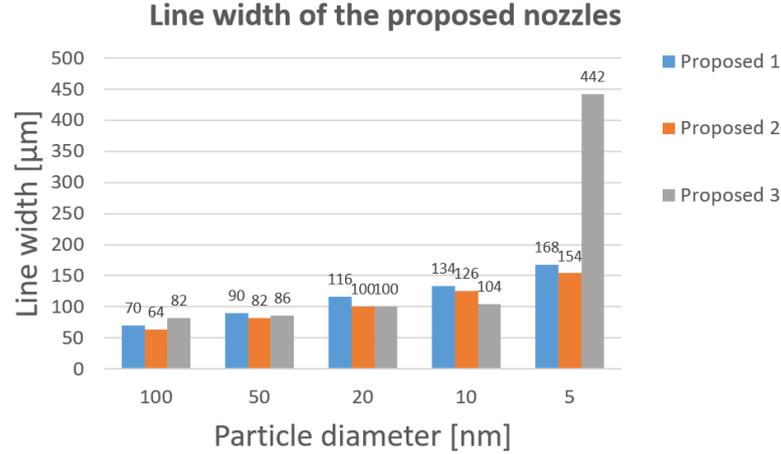The line width of the proposed nozzles are given in fig. 5.5.

Figure 5.5: The line width of different particle sizes of the proposed nozzles.

All three nozzles have approximately the same modelled line widths for each different particle size. The main difference in the line width is in proposed 3, with particle diameters of 5 nm. This nozzle shows significantly higher line width for these small particles. These proposed nozzles show line widths of 104-134 microns for particles with a diameter of 10 nm.

The focusing ratios of the proposed nozzles are given in fig. 5.6.
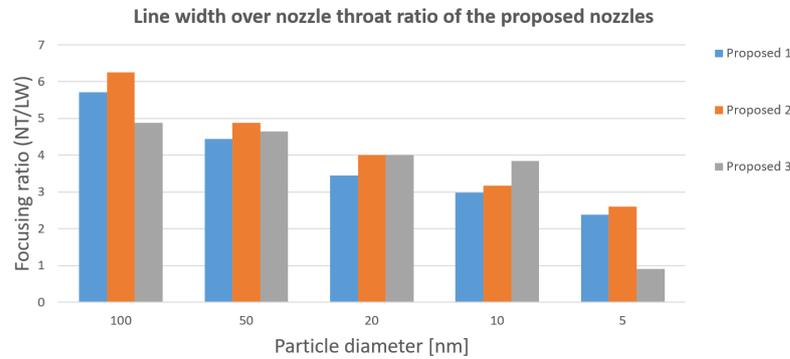
Figure 5.6: The focusing ratio (nozzle exit throat/line width) of different particle sizes of the proposed nozzles.

The nozzles have approximately the same focusing ratios in each particle size. The only difference is again with proposed 3 and a particle diameter of 5 nm. This particle size shows a relatively low focusing ratio compared to the other nozzles. With these proposed nozzles it is seen that even the small particles have focusing ratios above the value of one, indicating a good focusing nozzle for small particle sizes.

All in all, it is seen that the proposed CSG nozzles have much better focusing aspects than the traditional C nozzles. These proposed nozzles are used to reach the desired goal of this research.

5.2 Sheath gas implementation in experimental setup and nozzles

The setup, as given in section 1.3, does have the possibility to add a sheath gas line, but is was never fully connected and tested. The nozzles tested on this setup were the C nozzle type. To implement sheath gas into the SAM setup, some modifications have to be made to the setup itself and the nozzles, including the the procedure of printing and connecting these nozzles.

5.2.1 SAM setup preparation

As discussed earlier, the SAM setup generates a polydisperse aerosol flow. Since the sizes in this aerosol differ, different inertia forces will act on the (nano)particles. Smaller particles will more likely follow the streamlines, due to their small relaxation time, after the nozzle exit.

Considering this, first the size dependency of the particles related to the nozzle design is investigated. The results in chapter 4 showed that larger particles will always be better focused than smaller particles. Due to this result, it is chosen to not add a size selector to the system, but to focus all the particles in the system. The designed nozzles that focus ≤ 10 nm nanoparticles to a line width of approximately 100 μm, are good to experiment with in this setup.

To connect a nozzle that uses sheath gas, the setup is slightly modified. The nozzle has two entries instead of one, i.e. one for the aerosol and one for the sheath gas. The sheath gas is supplied via another line to the vacuum chamber. The total system including these modifications is given in a schematic view, as shown in fig. 5.7.
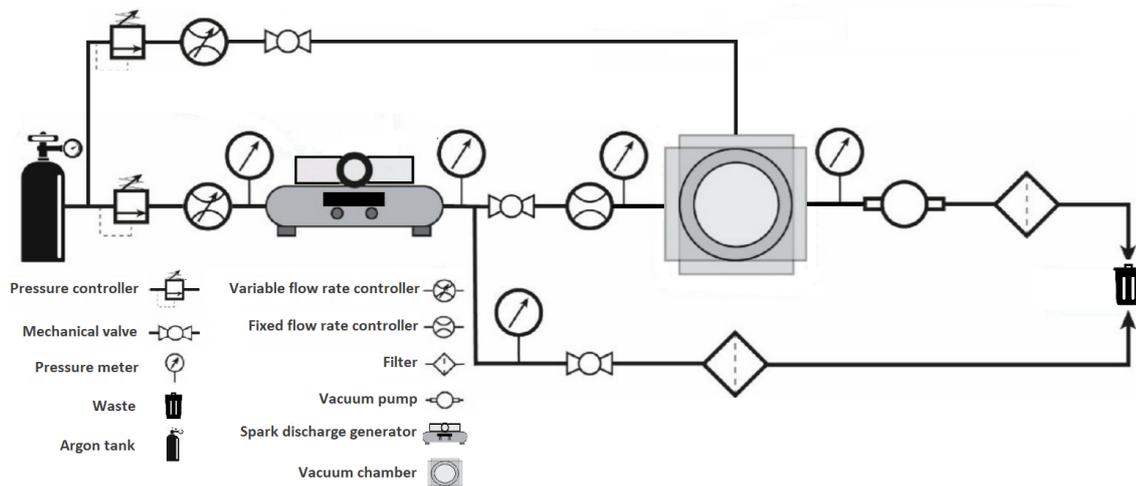

Figure 5.7: Schematic representation of the SAM setup with the connected sheath gas line.

The sheath gas line is connected to the vacuum chamber on the backside. A 4 mm pipe is connected, on the inside, to the the sheath gas inlet. This is then connected to the nozzle itself. Figure 5.8 shows the CSG nozzle connected and installed in the vacuum chamber.

This enables the nozzle to receive sheath gas separately from the aerosol line. Considering the proposed nozzles, it is seen that all of these nozzles are significantly longer than
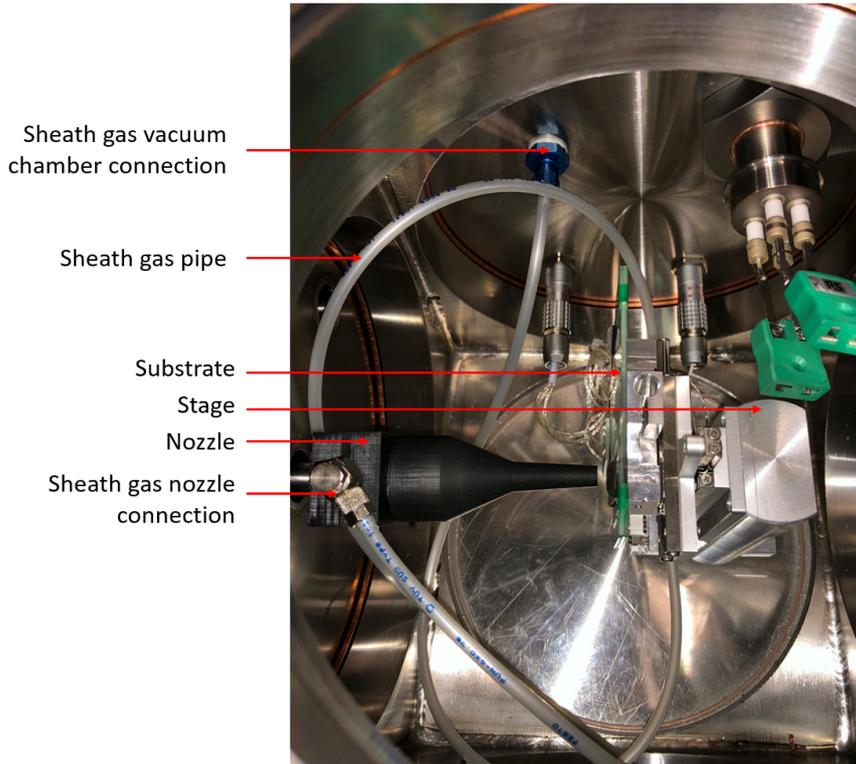
Figure 5.8: Converging sheath gas nozzle connected and installed in the vacuum chamber.

the originally used C nozzles. The SAM setup was designed to fit these C-size-nozzles. Unfortunately, the space in the vacuum chamber was not large enough to mount these nozzle without damaging it. The pipe where the nozzles are mounted on was longer than necessary. To be able to fit these nozzles in the vacuum chamber and mount them, this pipe was removed and cut.

5.2.2 Nozzle preparation

To be able to print and connect the proposed nozzles properly, a few CSG type nozzles are test printed. The first nozzle printed is the standard CSG nozzle with a nozzle exit throat of 400 μm, as shown in fig. 5.9. A first CAD model of this concept was made using Autodesk. This model is shown in fig. 5.9a. The dimensions and technical details are shown in fig. 5.9b.

This model is printed using the SLA 3D printer with HTM140V2 as resin material. After curing this nozzle an attempt was made to connect it to the aerosol and sheath gas line of the SAM setup.

The sheath gas connection hole in this nozzle has a diameter of 4.3 mm, while the connection itself is 5 mm. After printing the nozzle, this hole is drilled to 5 mm and tapped. By mechanically drilling it to 5 mm, unnecessary leakage is prevented. This is because the mechanical drilling has a higher resolution than the SLA printing. However, this hole is made in a 15 degree angle with a 3 mm wall. This resulted in a fracture in the hole. Also, the chips of the drilling and tapping caused the nozzle to be clogged. To fix the fracture, manually resin was put around the (air pneumatic L-shaped pipe) connection and cured. However, the nozzle was still clogged. Nevertheless, it was concluded that this
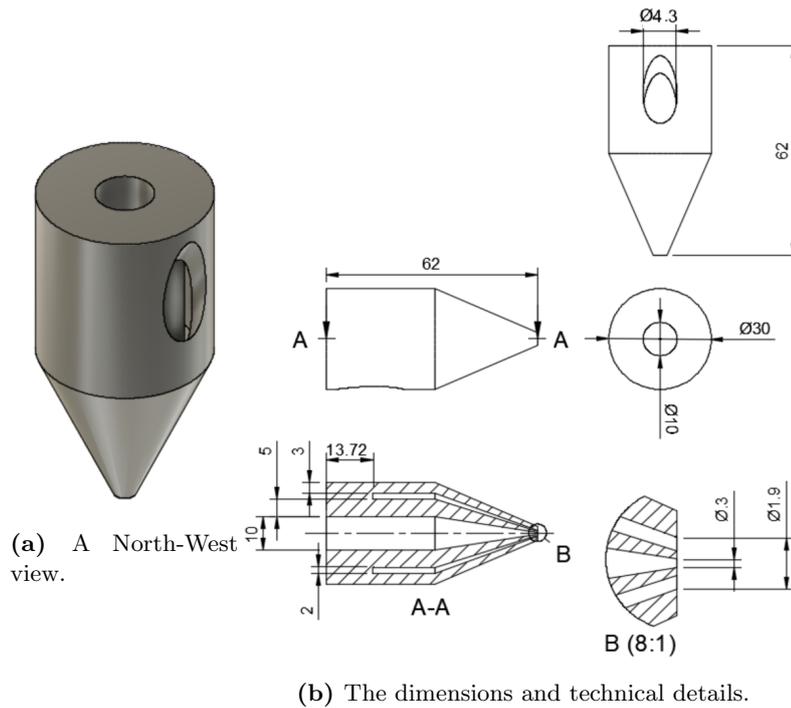
(a) A North-West view.

(b) The dimensions and technical details.

Figure 5.9: The first CAD model of the Converging sheath gas nozzle.

procedure of printing, drilling and tapping to connect the nozzle, is a successful idea. The first, clogged and fractured, connected nozzle to the sheath gas pipe, is shown in fig. 5.10.

Figure 5.10: First connected converging sheath gas nozzle to the sheath gas pipe.

To solve the fracturing and clogging of the nozzle, a few updated CAD models were made. In these models the Design for manufacturing (DFM) failures were adjusted. The main DFM violations were at the sheath gas connection.

The DFM rules, that are used to adjust the nozzle, are given in the bullet points below. [69]

- It is important that only surfaces perpendicular to the centerline of the hole are entered and exited when drilling. The drill tip will tend to wander if it contacts the non-planar surface.

- Machining deep and small diameter holes is difficult. Hence they should be avoided. Drills with small diameters tend to wander and are prone to breaking. Also, when drilling too deep, chip removal becomes more difficult. Therefore, a hole diameter to depth ratio of less than three is recommended.

- Avoiding holes intersecting with cavities is recommended in drilling operations. If not, the drill will tend to wander and the chance of the drilling tool breaking increases.

Using these rules, it was chosen to remove the angle of the sheath gas connection hole and to make a muscle around the hole to prevent fracturing during drilling. The sheath gas connection was drilled with a diameter of 5 mm and only 10 mm deep, to prevent clogging and leakage. The aerosol connection hole is made 9.8 mm and is drilled to a diameter of 10 mm and 10 mm deep. These modifications resulted in the nozzle shown in fig. 5.11a. The dimensions and technical details are shown in fig. 5.11b.
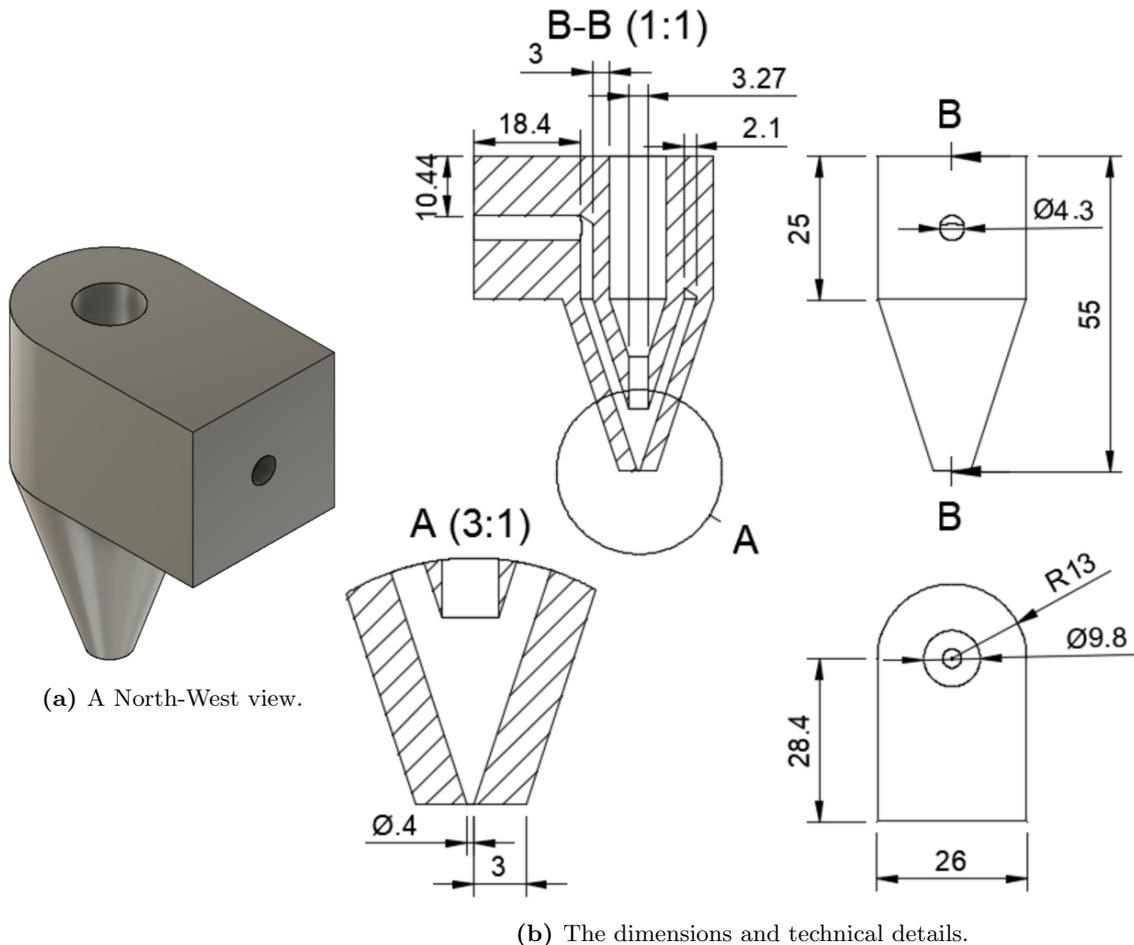

(a) A North-West view.

(b) The dimensions and technical details.

Figure 5.11: Modified CAD model of the converging sheath gas nozzle.

The modifications prevented the nozzle from fracturing and clogging. Also, the fitting of the aerosol inlet hole was much better. This resulted in the first working and mounted CSG nozzle.

It was concluded that this system will be able to print with sheath gas nozzles and that this procedure completely works.

Using the same procedure as above, the proposed nozzles are printed and manufactured. This procedure is used to ensure a tight and leakage proof fit without any fractures. The same geometry is used, in these nozzles, for the muscle around the sheath gas inlet. The rest of the shape and geometry of Proposed 1 is shown in fig. 5.12.

Figure 5.12: Shape, geometry and cross sections of Proposed 1.

As described earlier, Proposed 2 and 3 have the same shape and geometry as Proposed 1, the only difference is at the nozzle exit. All three nozzles are shown side to side in fig. 5.13.

(a) Proposed 1.   **(b)** Proposed 2.   **(c)** Proposed 3.

Figure 5.13: All three proposed nozzles.

A close up on the differences at the nozzle exit throat, are shown in fig. 5.14.

(a) Proposed 1.
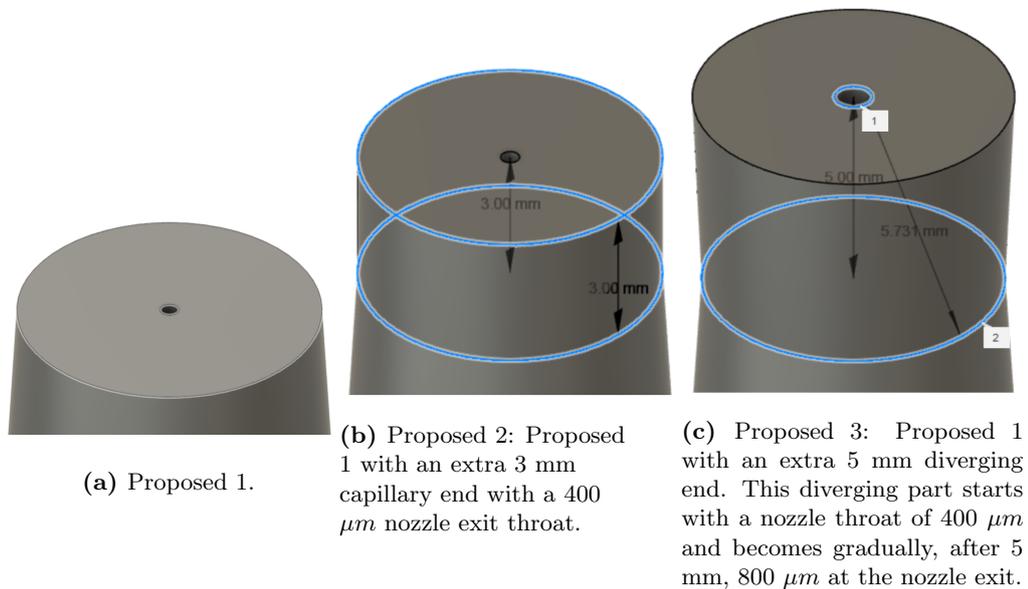
(b) Proposed 2: Proposed 1 with an extra 3 mm capillary end with a 400 μm nozzle exit throat.

(c) Proposed 3: Proposed 1 with an extra 5 mm diverging end. This diverging part starts with a nozzle throat of 400 μm and becomes gradually, after 5 mm, 800 μm at the nozzle exit.

Figure 5.14: The differences between the three proposed nozzles.

Proposed 1 was printed and connected, using the same procedure found earlier. This nozzle is shown in fig. 5.15.

Figure 5.15: Proposed 1 connected to the sheath gas line of the SAM setup.

5.3 Experimental results

Experiments are conducted using a C and CSG nozzle. Considering chapter 4, it is seen that the best C nozzle has the smallest possible nozzle exit throat and angle. For this reason, the C nozzle used during the experiments, has a nozzle exit throat of 400 μm and a angle of approximately 10 degrees. The CSG nozzle used during these experiments is Proposed 1. Microscopic glass sliders are used as substrates in these experiments.

5.3.1 Effect of writing speed

To be able to write good lines and have a good comparison between the C and CSG nozzle, the effect of the writing speed needs to be studied. This is tested by using the C nozzle. During experiments the working distance was kept at 500 μm and the pressure in the vacuum chamber was approximately kept at 285 Pa. The generator was set to have a voltage of 1.3 kV and a current of 9.0 mA. The resulting printed lines, using different writing speeds, are shown in fig. 5.16.

The line widths are measured using the Keyence microscope, which is a digital microscope. To determine the average measurement error, the same configuration is used to write two lines. These lines are then measured. This is done for several lines. Using these values an estimated error margin is set for all the digital microscope measurements. The average of all these differences is found to be: $\frac{18+45+9+28}{4} = 25\mu m$.

The lines are traditionally written by moving the stage to the right and then, following the same path, back to it's origin. This is done to increase the amount of particles deposited per line. However, it causes an overlay error. It is clearly seen that high writing speeds result in less deposited particles. To have good and visible lines, writing speeds of maximum 0.1 mm/s should be chosen. For this reason, a speed of 0.045 mm/s is preferred to go back and forth on the line. To prevent the overlay error, the nozzle is moved with approximately half the speed (0.03 mm/s) to the desired position on the substrate. On the way back a much higher speed of 5 mm/s is used to be able to neglect the particle deposition. This results in approximately the same particle density, but a more accurate line width since the overlay and stage offset error on the way back can be neglected.
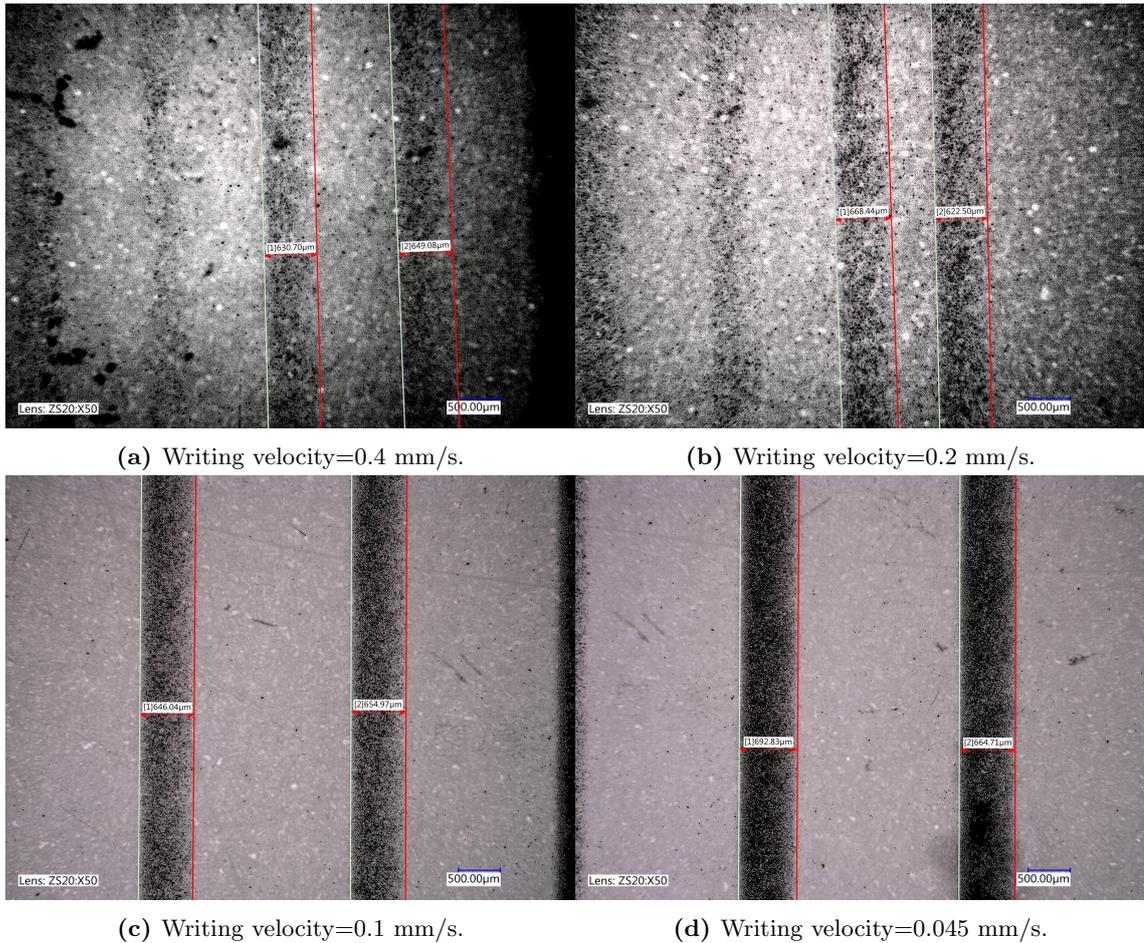
(a) Writing velocity=0.4 mm/s.

(b) Writing velocity=0.2 mm/s.

(c) Writing velocity=0.1 mm/s.

(d) Writing velocity=0.045 mm/s.

Figure 5.16: Digital microscope imaging showing the printed lines with different writing speeds, using a converging nozzle. The line widths shown have an error margin of ± 25 microns.

5.3.2 Effect of vacuum chamber pressure

Since the sheath gas line blows sheath gas into the nozzle in the vacuum chamber, the pressure in this area (outlet pressure) will be higher for CSG nozzles than for the C nozzles. To understand the effect of this difference, various outlet pressures were set while printing lines with the C nozzle. The outlet pressure was varied by not connecting the sheath gas line to the nozzle, but letting the sheath gas blow into the vacuum chamber. During the experiments the working distance was kept at 400 μm. The generator was set to have a voltage of 1.3 kV and a current of 9.0 mA. The resulting line widths are shown in fig. 5.17.

It can be seen that the line width slightly increases when increasing the outlet pressure. This indicates that the CSG nozzles will have a small disadvantage, considering the pressure, since they operate in a higher outlet pressure than the C nozzles.
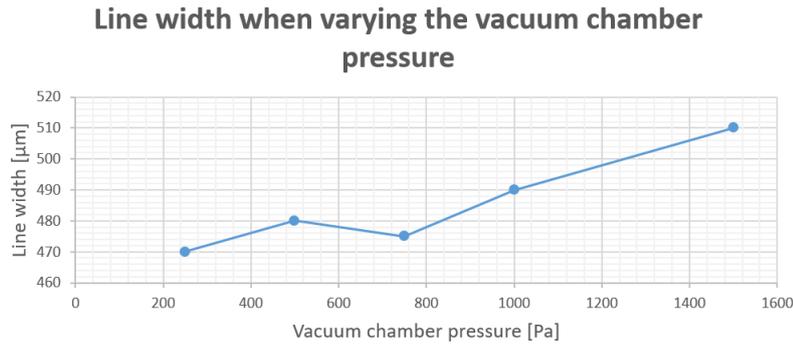
Figure 5.17: Line width, using a converging nozzle, when varying the vacuum pressure.

5.3.3 Effect of flow rates

Since the system has to operate at a pressure of 1 bar (inlet pressure), the flow rates of the nozzles are restricted. Each specific nozzle has a flow rate value that keeps the system at this pressure. The C nozzle used in these experiments has a flow rate of 1.00 l/min and the CSG nozzle, Proposed 1, has a flow rate of 2.15 l/min. The flow rate of the CSG nozzle is higher, since a separate line blows sheath gas into the nozzle. This indicates that the maximum flow rate, that can be used in this system while operating at 1 bar, is mainly dependent on the nozzle exit throat of the aerosol channel.

Experiments were done with different sheath gas flow rates, as shown in fig. 5.18. During these experiments, the working distance was kept at 500 μm and the pressure in the vacuum chamber was approximately 600 Pa. The generator was set to have a voltage of 1.3 kV and a current of 9.0 mA. Figure 5.18a shows the line widths using the digital microscope and fig. 5.18b shows these line width in a graph.

It can clearly be seen that increasing the sheath gas ratio results in narrower lines. The same trend was also seen in chapter 4 when modelling these nozzles. However, the results of the effect of sheath gas become less significant for values below A/T=2/8.
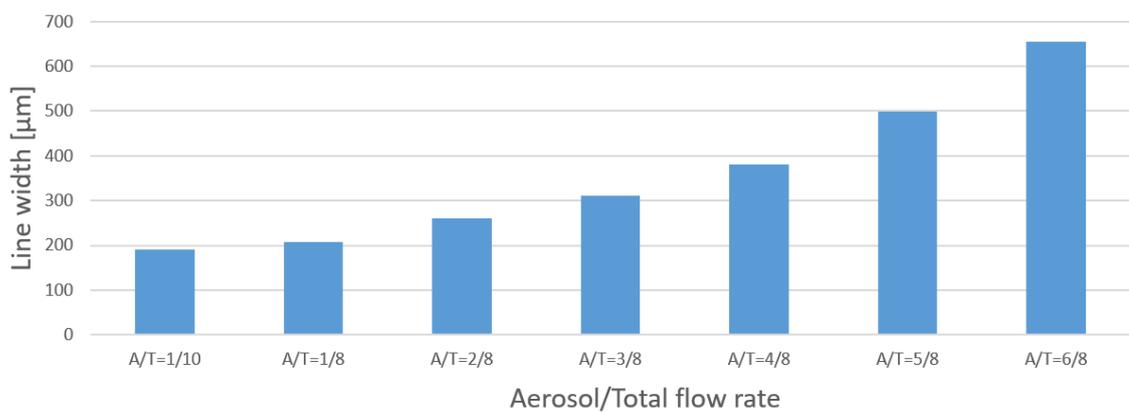
These line widths are found to be wider during the experiments than expected using the models. This difference is due to all the losses that were not accounted for during modelling. Firstly, the model assumes that when the particles hit the substrate, they will directly adhere to it. It may well be that this is not the case during the experiments, since particles can bounce and shift from their first impaction location on the microscopic glass slider substrate. Secondly, it is assumed during modelling that the outlet pressure would be 100 Pa. In reality this was higher. Finally, the stage has some inaccuracies. It is very hard to set up the nozzle exactly parallel to the substrate and the desired working distance. All these factors could explain why the line widths during the experiments are slightly wider than seen during modelling.

Also, the stages moves down, due to gravity, when it is moved sideways. This shift can be 50-200 μm when writing a line, which effects where the line is written on the substrate. However, this shift does not effect the line width itself.
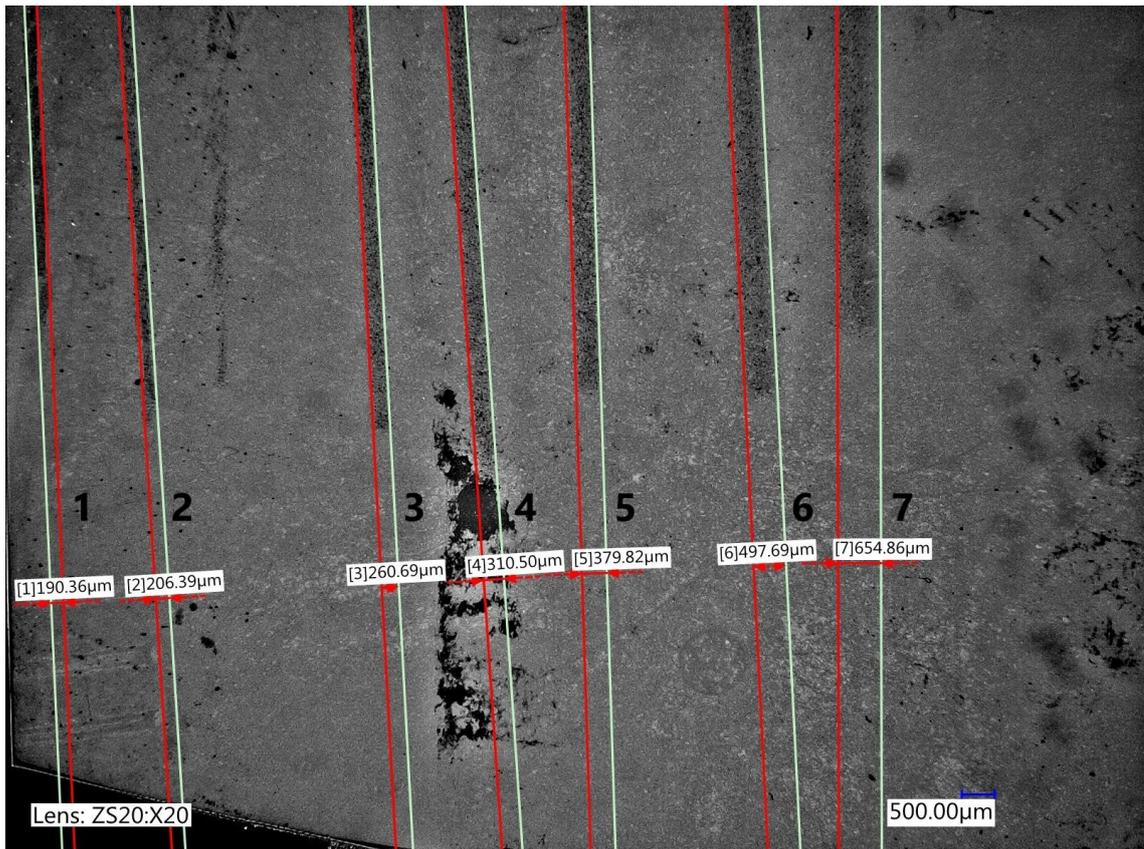
(a) Digital microscope imaging: 1) A/T=1/10, 2) A/T=1/8, 3) A/T=2/8, 4) A/T=3/8, 5) A/T=4/8, 6) A/T=5/6 and 7) A/T=6/8. The line widths shown have an error margin of ±25 microns.

(b) The trend of the different average line widths shown in a graph.

Figure 5.18: Line widths of Proposed 1 when varying the aerosol flow rate to total flow rate ratio.

All in all, the experiments showed that the models are capable of representing what will happen in reality.

Chapter 6

Conclusions

The models showed that the contraction factor of the C nozzle is dependent on its shape only, i.e. a small nozzle exit throat will physically move the particles towards the centerline. Hence, the machinery used to make high deposition resolution C nozzles, should have very high resolution to be able to print small nozzle exit throats. The C nozzles are only capable of depositing ≤ 10 nm particles if these exits are sufficiently small. This makes these nozzle more likely to get clogged. Also, the focusing ratio never exceeds the value of one, indicating always a wider line width than the nozzle exit throat diameter.

The models also showed that the deposition resolution is much better with the sheath gas system. High sheath gas ratios in the system, regardless of other design parameters, are essential for bringing particles close to the nozzle centerline. Small nozzle exit throats are essential for small line widths. The A/T ratio has the biggest contribution to raising the contraction factor. This also results in the ability to decrease the nozzle exit throat diameters without any clogging occurring. Introducing the sheath gas earlier in the nozzle is more effective than at the end of the nozzle. Also, adding sheath gas to the nozzle increases the particle velocity.

A high particle velocity is very important to deposit narrow line widths. However, this is not the only important factor. Smaller line widths are also achieved with smaller angles and longer converging sections. Also, it is seen that the contraction factor hardly depends on the particle size. The focusing ratio is subsequently most influenced by the nozzle exit throat diameter. It is seen that smaller nozzle exit throats have significantly higher focusing ratios for ≤ 10 nm particles. It is also noticed that the working distance does not effect the contraction factor directly. This indicates that the nozzle does not have to work very close to substrate and can deposit on non-flat surfaces.

Using these learnings, three proposed nozzles are designed and manufactured. It is seen that all three nozzles have excellent contraction factors. Proposed 2 and 3 have slightly better contraction factors than proposed 1. This is because they have higher axial particle speeds due to their capillary and diverging end.

The best modelled contraction factor, focusing ratio and line width achieved, using 10 nm particles, with a converging nozzle are 1.0, 0.4 and 874 microns, respectively. This nozzle has a nozzle exit throat of 400 microns and an angle of 10 degrees. However, a modelled contraction factor of 9.3, focusing ratio of 3.8 and line width of 104 microns are achieved using the proposed converging sheath gas nozzle with a nozzle throat of 400 microns and an angle of 5 degrees. Even narrower line widths are expected if the throat diameters are reduced.

During the experiments it is seen that the maximum flow rate, that can be used in this setup while operating at 1 bar, is mainly dependent on the nozzle exit throat of the aerosol channel. The line widths, for the CSG type nozzle, during the experiments are wider than modelled. This difference is due to all the losses that were not accounted for during modelling. Firstly, the model assumes that when the particles hit the substrate, they will directly adhere to it. It may well be that this is not the case during the experiments, since particles can bounce and shift from their first impaction location on the substrate. Secondly, during modelling it is assumed that the outlet pressure would be 100 Pa. In reality this was slightly higher. Finally, the stage has some inaccuracies. It is very hard to setup the nozzle exactly parallel to the substrate and the desired working distance. All these factors could explain why the line widths during the experiments are slightly wider than seen during modelling.

Chapter 7

Recommendations

Firstly, recommendations are given to improve the SAM setup. Then, future work recommendations are discussed.

SAM setup

The stage used in the SAM setup is not very robust and accurate. It is very difficult to write controlled lines, with a high resolution, using this stage. It could be improved in terms of robustness and accuracy. Actuation of the stage rotation can also be implemented. This would enable the selection of the right angle while depositing particles. Also, placing the substrate exactly parallel to the nozzle would be more accurate and significantly easier.

The controller used in this system needs to be manually handled. It can be changed to a Labview operated system. This could increase the usability and accuracy of the system.

Future work

It was seen that Proposed 2 and 3 also achieved good results. Thus, different shapes than the C and CSG nozzles can be designed and tested using the conclusions gathered in this research.

The usage of multi-scale printing can be studied and applied. Doing so, the SLA printer can still be used for the bulk parts of the nozzle and the Nanoscribe for the parts that require higher resolution printing. This can be used to print smaller nozzle exit throats to enhance the deposition resolution.

Skimmers can be studied and added to the nozzles. By using these skimmers, well collimated molecular beams can be made. If these skimmers are engineered correctly within a nozzle, the deposition resolution can be enhanced.

The addition of E-fields can be studied and added to the system. The nanoparticles can be manipulated to focus towards a specific spot by using these electrical fields. The deposition resolution can be enhanced by designing a nozzle, of multi-material, that is able to use the advantages of this field.

Deposition on different substrates can be studied. In this research microscopic glass sliders were used as substrates. A higher surface roughness could result in higher deposition resolution. With increase of substrate surface roughness, the adhesive strength is increased. Using glass, the particles could easily impact and then slide or bounce to other position or not deposit at all. Different coatings on substrates can also be studied.

The deposited particles are made out of copper. In future research different metal particles can be studied and compared in terms of deposition resolution. Difference in particle density might effect the line width while using the same sizes of particles as used in this research. There might be a larger range of particle diameters that focus better if particles with higher density are deposited and vice versa.

Appendix A

MATLAB script for aerosol and sheath gas flow rate calculation

```matlab
%%Flow rates (FR) in liter per min
fra=1.6;                        %Aerosol flow rate [L/min]
frs=0;                          %Sheath gas flow rate [L/min]

%%Dimensions nozzle in meter
r1=5e-3;                        %Aersol inlet diamter [m]
r2=8e-3;                        %Inner ring sheath gas inlet diamter [m]
r3=10.1e-3;                     %Outer ring sheath gas inlet diamter [m]


%%Fixed Properties of Argon gas
c=319;                          %Speed of sound (Argon gas) [m/s]

%%Calculate Mach Number of flow rates for aerosol
FRa=fra*(1/60000);

Aa=pi*(r1^2);

Va=FRa/Aa;

Maa=Va/c;                       %Mach Number for the given aerosol flow rate

%%Calculate Mach Number of flow rates for sheath gas
FRs=frs*(1/60000);

As=pi*(r3^2-r2^2);

Vs=FRs/As;

Mas=Vs/c;                       %Mach Number for the given sheath flow rate
```

Figure A.1: MATLAB script for calculating the Mach Numbers for different ratios of aerosol and sheath gas flow rates.

Appendix B

MATLAB script for speed interpolation and extraction

```matlab
%Extract speed data from COMSOL file

%%
%Read extracted COMSOL values
A=readmatrix('C:\Users\Roberto-PC\Desktop\TU Documenten\Master thes
%%
%Find values
XX=31296;
z=A((XX)-100:XX,2);
vz=A((XX)-100:XX,6);
vr=A((XX)-100:XX,5);
x=z(1):0.0001:z(101);
vzm=spline(z,vz,x);
vrm=spline(z,vr,x);

%%
%Extract (interpolated) speed nozzle throat
XXX=78079;
vzm(XXX)
vrm(XXX)
```

Figure B.1: An example of a MATLAB script that reads the extracted COMSOL values, interpolates the extracted axial and radial speeds and gives these speeds at the centerline of the nozzle exit.

Appendix C

Additional flow rates results

This appendix shows the results of the CSG models with A/T=4/8 and A/T=7/8.

Velocity

The resulting axial and radial particle speeds, when adjusting the CSG nozzle with A/T=4/8, are given in fig. C.1. These are the maximum speeds measured at the centerline and exit of the nozzles. The values are interpolated.
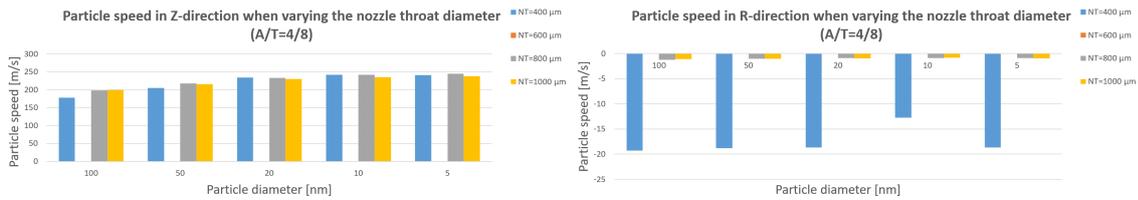
(a) Axial speed when changing the nozzle exit throat.
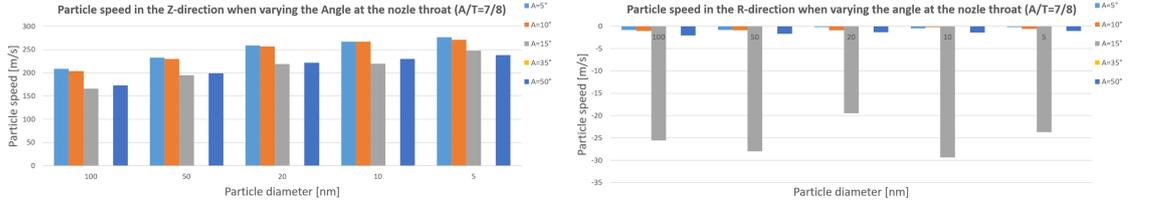

(b) Radial speed when changing the nozzle exit throat.
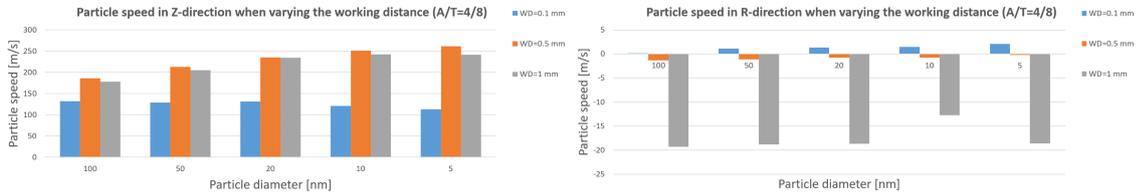
(c) Axial speed when changing the working distance.

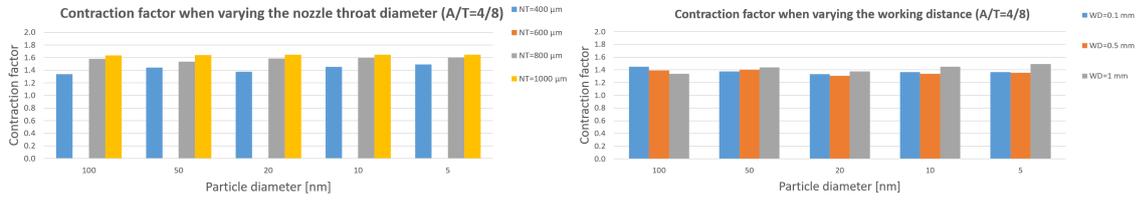**(d)** Radial speed when changing the working distance.
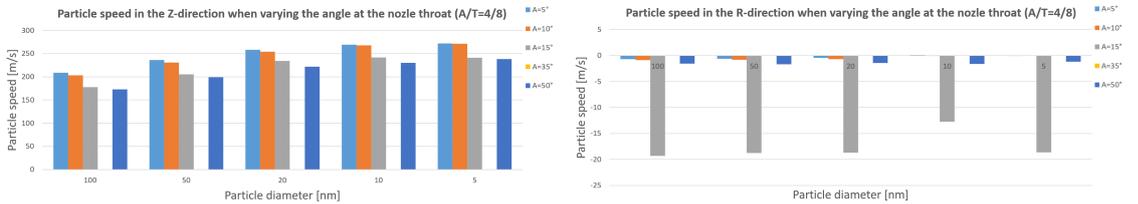
(e) Axial speed when changing the angle and nozzle length.

(f) Radial speed when changing the angle and nozzle length.

Figure C.1: The particle axial (Z) and radial (R) speeds of different particle sizes when changing different parameters of a converging sheath gas nozzle with A/T=4/8. These are the maximum speeds measured at the centerline and exit of the nozzles. The values are interpolated.

The resulting axial and radial particle speeds, when adjusting the CSG nozzle with A/T=7/8, are given in fig. C.2. These are the maximum speeds measured at the centerline and exit of the nozzles. The values are interpolated.
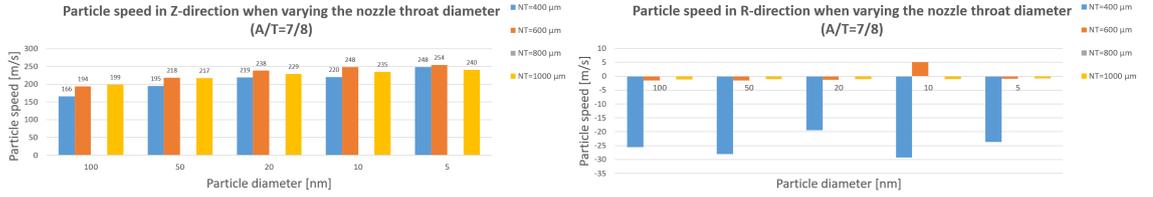
(a) Axial speed when changing the nozzle exit throat.

(b) Radial speed when changing the nozzle exit throat.
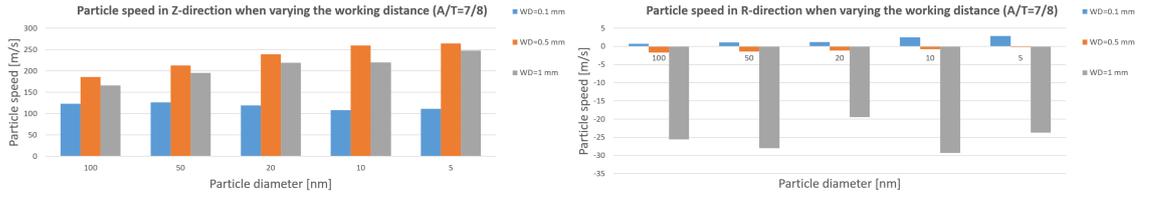
(c) Axial speed when changing the working distance.

(d) Radial speed when changing the working distance.

(e) Axial speed when changing the angle and nozzle length.

(f) Radial speed when changing the angle and nozzle length.

Figure C.2: The particle axial (Z) and radial (R) speeds of different particle sizes when changing different parameters of a converging sheath gas nozzle with A/T=7/8. These are the maximum speeds measured at the centerline and exit of the nozzles. The values are interpolated.
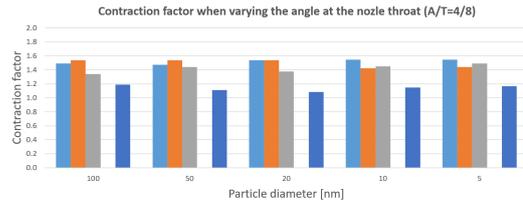
Contraction factor

The resulting contraction factors, when adjusting the CSG nozzle with A/T=4/8, are given in fig. C.3.

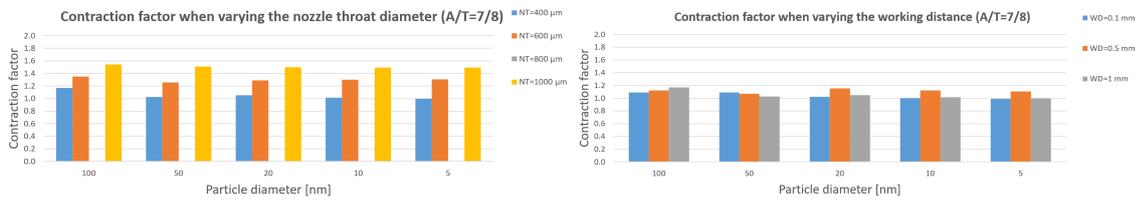
(a) The nozzle exit throat.

(b) The working distance.
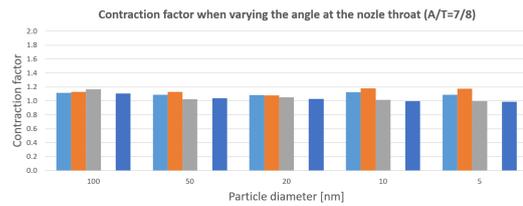

(c) The angle and nozzle length.

Figure C.3: The contraction factor of different particle sizes when changing different parameters of a converging sheath gas nozzle with A/T=4/8.

The resulting contraction factors, when adjusting the CSG nozzle with A/T=7/8, are given in fig. C.4.

(a) The nozzle exit throat.

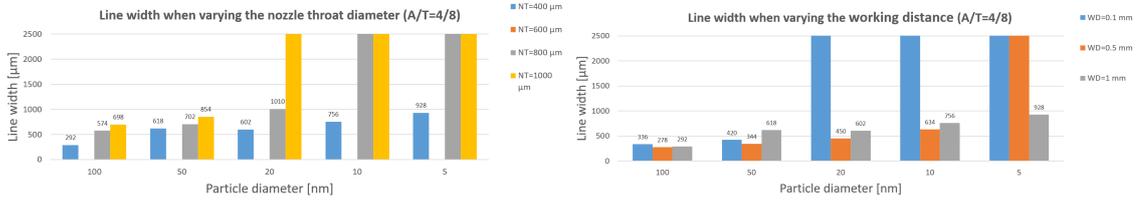**(b)** The working distance.

(c) The angle and nozzle length.

Figure C.4: The contraction factor of different particle sizes when changing different parameters of a converging sheath gas nozzle with A/T=7/8.
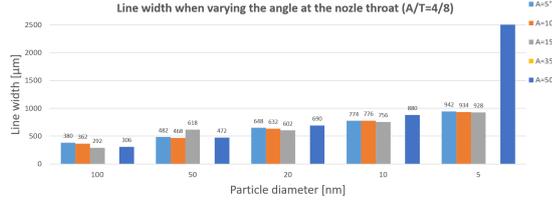
Line width

The resulting line widths, when adjusting the CSG nozzle with A/T=4/8, are given in fig. C.5.
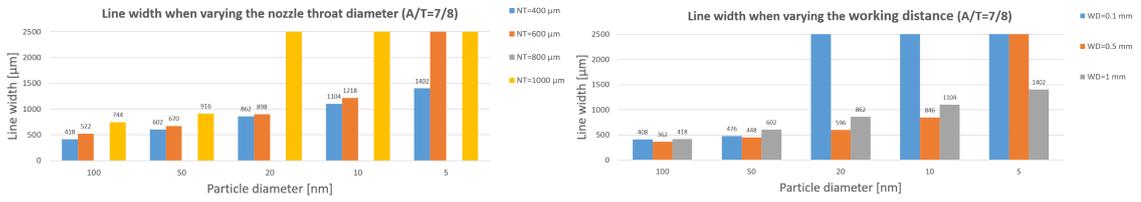

(a) The nozzle exit throat.

(b) The working distance.

(c) The angle and nozzle length.

Figure C.5: The line width of different particle sizes when changing different parameters of a converging sheath gas nozzle with A/T=4/8. Values above 2500 microns indicate that (most of) the particles did not deposit.

The resulting line widths, when adjusting the CSG nozzle with A/T=7/8, are given in fig. C.6.

(a) The nozzle exit throat.

(b) The working distance.
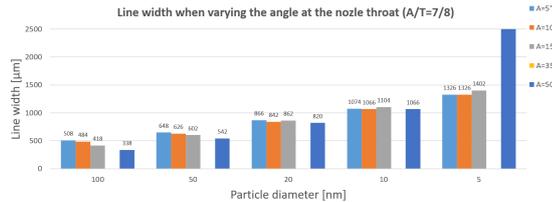

(c) The angle and nozzle length.

Figure C.6: The line width of different particle sizes when changing different parameters of a converging sheath gas nozzle with A/T=7/8. Values above 2500 microns indicate that (most of) the particles did not deposit.

Focusing ratio

The resulting focusing ratios (NT/LW), when adjusting the CSG nozzle with A/T=4/8, are given in fig. C.7.

(a) The nozzle exit throat.

(b) The working distance.

(c) The angle and nozzle length.

Figure C.7: The focusing ratio (nozzle exit throat/line width) of different particle sizes when changing different parameters of a converging sheath gas nozzle with A/T=4/8.

The resulting focusing ratios (NT/LW), when adjusting the CSG nozzle with A/T=7/8, are given in fig. C.8.

(a) The nozzle exit throat.

(b) The working distance.

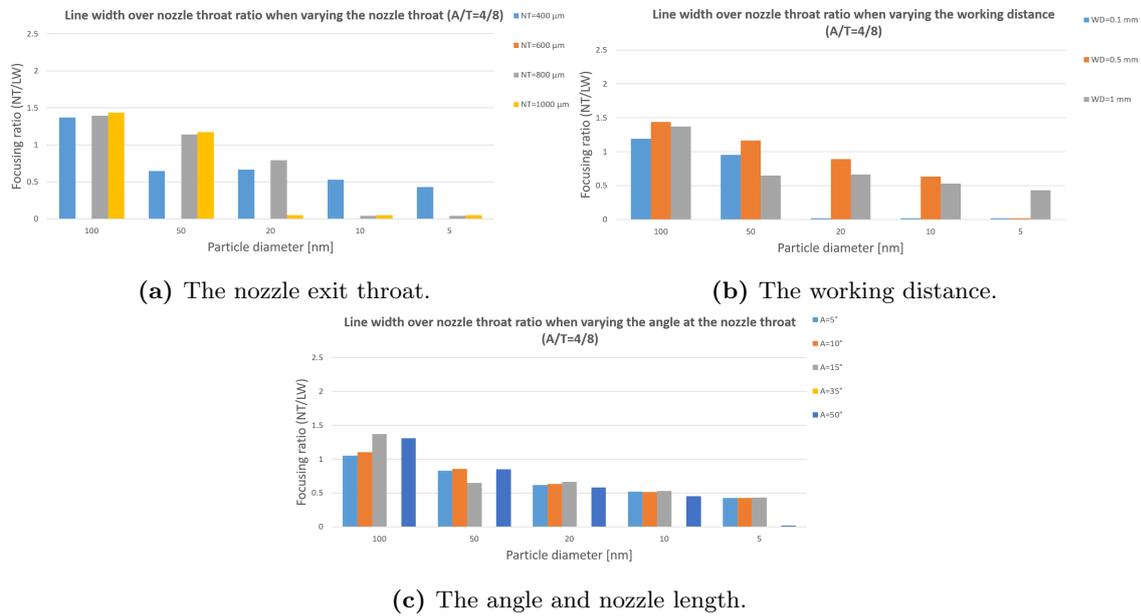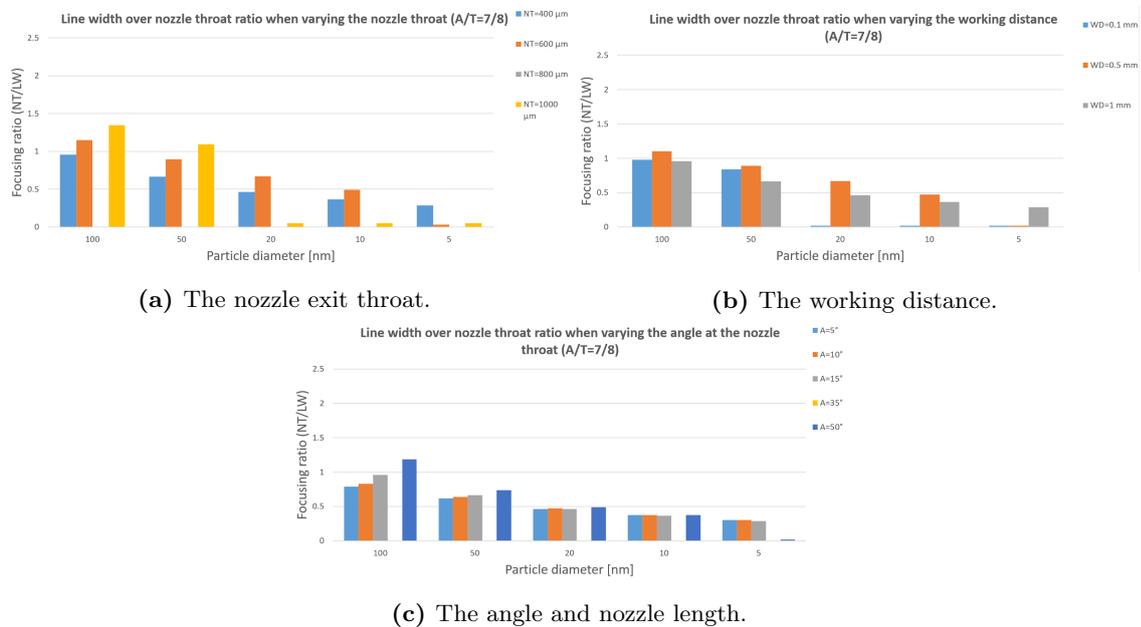**(c)** The angle and nozzle length.

Figure C.8: The focusing ratio (nozzle exit throat/line width) of different particle sizes when changing different parameters of a converging sheath gas nozzle with A/T=7/8.

Bibliography

[1] Florian J Heiligtag and Markus Niederberger. "The fascinating world of nanoparticle research". In: *Materials Today* 16.7-8 (2013), pp. 262–271.

[2] Kaufui V Wong and Aldo Hernandez. "A review of additive manufacturing". In: *International scholarly research notices* 2012 (2012).

[3] K. K B Hon, L. Li, and I. M. Hutchings. "Direct writing technology-Advances and developments". English. In: *CIRP Annals - Manufacturing Technology* 57.2 (2008), pp. 601–620. ISSN: 0007-8506. DOI: 10.1016/j.cirp.2008.09.006.

[4] Bruce King and Mike Renn. "Aerosol Jet direct write printing for mil-aero electronic applications". In: *Lockheed Martin Palo Alto Colloquia, Palo Alto, CA*. 2009.

[5] Victor Champagne et al. "Deposition of copper micro-circuitry by capillary focusing". In: *Journal of Micromechanics and Microengineering* 23.6 (2013), p. 065023.

[6] Justin Hoey et al. "CAB-DW^{TM} for 5 μm trace-width deposition of solar cell metallization top-contacts". In: *2009 34th IEEE Photovoltaic Specialists Conference (PVSC)*. IEEE. 2009, pp. 001857–001861.

[7] N. S. Tabrizi et al. "Generation of nanoparticles by spark discharge". In: *Journal of Nanoparticle Research* 11.2 (May 2008), p. 315. ISSN: 1572-896X. DOI: 10.1007/s11051-008-9407-y. URL: https://doi.org/10.1007/s11051-008-9407-y.

[8] Dion G. Vlachos. "Handbook of Nanophase Materials Edited by Avery N. Goldstein (The Dow Chemical Company). Dekker: New York. 1997. vii + 369 pp. \$165.00. ISBN 0-8247-9469-9." In: *Journal of the American Chemical Society* 120.18 (1998), pp. 4556–4556. DOI: 10.1021/ja9756026. eprint: https://doi.org/10.1021/ja9756026. URL: https://doi.org/10.1021/ja9756026.

[9] NJ Wilkinson et al. "A review of aerosol jet printing—a non-traditional hybrid process for micro-manufacturing". In: *The International Journal of Advanced Manufacturing Technology* 105.11 (2019), pp. 4599–4619.

[10] M. J. Renn et al. "Flow-and laser-guided direct write of electronic and biological components," in: *Direct-Write Technologies For Rapid Prototyping Applications* 48 (2002), pp. 475–492.

[11] Weiping Liu and J.N. DuPont. "Fabrication of functionally graded TiC/Ti composites by Laser Engineered Net Shaping". In: *Scripta Materialia* 48 (May 2003), pp. 1337–1342. DOI: 10.1016/S1359-6462(03)00020-4.

[12] "Mesoscribe Technologies". In: *Mesoscribe* (). URL: http://www.mesoscribe.com/.

[13] DB Chrisey et al. "Direct writing of conformal mesoscopic electronic devices by MAPLE DW". In: *Applied Surface Science* 168.1-4 (2000), pp. 345–352.

[14] A Doraiswamy et al. "Laser microfabrication of hydroxyapatite-osteoblast-like cell composites". In: *Journal of Biomedical Materials Research Part A* 80.3 (2007), pp. 635–643.

[15] Linda H Schmoll et al. "Nanoparticle aerosol generation methods from bulk powders for inhalation exposure studies". In: *Nanotoxicology* 3.4 (2009), pp. 265–275.

[16] Artur Lutfurakhmanov et al. "Capillary-based liquid microdroplet deposition". In: *Applied Physics Letters* 97.12 (2010), p. 124107.

[17] IS Akhatov et al. "Aerosol flow through a long micro-capillary: collimated aerosol beam". In: *Microfluidics and Nanofluidics* 5.2 (2008), pp. 215–224.

[18] J. M. Hoey et al. "Convergent-divergent-convergent nozzle focusing of aerosol particles for micron-scale direct writing". In: (2009).

[19] R. A. Sailer and J. M. Hoey. "Micro cold spray direct write technology for printed micro electronics applications". In: (2012).

[20] S. Bhattacharya et al. "Aerosol flow through a long micro-capillary: collimated aerosol beam". In: *Microfluidics and Nanofluidics* (2012).

[21] S. Watson. "Aerosol Jet printed electronics overview". In: *Optomec* (2012).

[22] Xuefeng Zhang et al. "A Numerical Characterization of Particle Beam Collimation by an Aerodynamic Lens-Nozzle System: Part I. An Individual Lens or Nozzle". In: *Aerosol Science and Technology* 36.5 (2002), pp. 617–631. DOI: `10.1080/02786820252883856`. eprint: `https://doi.org/10.1080/02786820252883856`. URL: `https://doi.org/10.1080/02786820252883856`.

[23] Raymond Reinmann and Muhammad Akram. "Temporal investigation of a fast spark discharge in chemically inert gases". In: *Journal of Physics D: Applied Physics* 30.7 (1997), p. 1125.

[24] VsParticle. In: *VsParticle Technology* (). URL: `https://vsparticle.com/about/technology/`.

[25] Emil Yankov and Maria Nikolova. "Comparison of the Accuracy of 3D Printed Prototypes Using the Stereolithography (SLA) Method with the Digital CAD Models". In: *MATEC Web of Conferences* 137 (Nov. 2017), p. 02014. DOI: `10.1051/matecconf/201713702014`.

[26] Ze-Xian Low et al. "Perspective on 3D printing of separation membranes and comparison to related unconventional fabrication techniques". In: *Journal of Membrane Science* 523 (2017), pp. 596–613. ISSN: 0376-7388. DOI: `https://doi.org/10.1016/j.memsci.2016.10.006`. URL: `http://www.sciencedirect.com/science/article/pii/S0376738816304215`.

[27] "ANSYS CFX-Solver Theory Guide". In: (2011).

[28] I.S. Akhatov et al. "Aerosol flow through a micro-capillary". In: vol. 1. cited By 6. 2010, pp. 223–232. DOI: `10.1115/MNHMT2009-18421`. URL: `https://www2.scopus.com/inward/record.uri?eid=2-s2.0-77954321037&doi=10.1115%2fMNHMT2009-18421&partnerID=40&md5=d80ce39adb7f11eb8c6b50fe299aaaf1`.

[29] M. Sommerfeld C. T. Crowe and Y. Tsuji. "Multiphase Flows with Droplets and Particles". In: (1998).

[30] Inchul Kim, Said Elghobashi, and William A Sirignano. "On the equation for spherical-particle motion: effect of Reynolds and acceleration numbers". In: *Journal of Fluid Mechanics* 367 (1998), pp. 221–253.

[31]   JS Marshall. "Discrete-element modeling of particulate aerosol flows". In: *Journal of Computational Physics* 228.5 (2009), pp. 1541–1561.

[32]   Fuat Odar and Wallis S Hamilton. "Forces on a sphere accelerating in a viscous fluid". In: *Journal of Fluid Mechanics* 18.2 (1964), pp. 302–314.

[33]   Jingyu Ran et al. "Numerical simulation of the particle motion characteristics in boundary layer of gas-solid rotary flow". In: *Journal of fluids engineering* 128.3 (2006), pp. 596–601.

[34]   PGT Saffman. "The lift on a small sphere in a slow shear flow". In: *Journal of fluid mechanics* 22.2 (1965), pp. 385–400.

[35]   R. I. Nigmatulin. "Dynamics of Multiphase Media". In: 1-2 (1991).

[36]   George Gabriel Stokes. *On the effect of the internal friction of fluids on the motion of pendulums.* Vol. 9. Pitt Press Cambridge, 1851.

[37]   J Fernandez De La Mora and P Riesco-Chueca. "Aerodynamic focusing of particles in a carrier gas". In: *Journal of Fluid Mechanics* 195 (1988), pp. 1–21.

[38]   Zhigang Li and Hai Wang. "Drag force, diffusion coefficient, and electric mobility of small particles. I. Theory applicable to the free-molecule regime". In: *Physical Review E* 68.6 (2003), p. 061206.

[39]   Robert A Millikan. "Coefficients of slip in gases and the law of reflection of molecules from the surfaces of solids and liquids". In: *Physical review* 21.3 (1923), p. 217.

[40]   Ed RW Johnson. "The Handbook of Fluid Dynamics CRC Press LLC". In: (1998).

[41]   Emilio E Paladino and Clovis R Maliska. "Virtual mass in accelerated bubbly flows". In: *Proceedings of 4th European Themal Sciences, 29th-31st March, National Exhibition Centre, Birmingham, UK* (2004).

[42]   Alek Jezoriek and Scott Moura. "Motions of baseballs and footballs". In: *Mechanical Engineering* 170 (2004).

[43]   Peng Liu et al. "Generating Particle Beams of Controlled Dimensions and Divergence: I. Theory of Particle Motion in Aerodynamic Lenses and Nozzle Expansions". In: *Aerosol Science and Technology* 22.3 (1995), pp. 293–313. DOI: 10.1080/02786829408959748. eprint: https://doi.org/10.1080/02786829408959748. URL: https://doi.org/10.1080/02786829408959748.

[44]   P. C. Reist. "Aerosol Science and Technology". In: *McGraw-Hill Inc.* Vol. Second Edition (1993).

[45]   Martin R Maxey and James J Riley. "Equation of motion for a small rigid sphere in a nonuniform flow". In: *The Physics of Fluids* 26.4 (1983), pp. 883–889.

[46]   Abraham Robinson. "On the motion of small particles in a potential field of flow". In: *Communications on pure and applied mathematics* 9.1 (1956), pp. 69–84.

[47]   Daniel J Rader. "Momentum slip correction factor for small particles in nine common gases". In: *Journal of aerosol science* 21.2 (1990), pp. 161–168.

[48]   NA Fuchs et al. "The mechanics of aerosols". In: *Physics Today* 18 (1965), p. 73.

[49]   T. Stoltenhoff, H. Kreye, and H. J. Richter. "An analysis of the cold spray process and its coatings". In: *Journal of Thermal Spray Technology* 11.4 (Dec. 2002), pp. 542–550. ISSN: 1544-1016. DOI: 10.1361/105996302770348682. URL: https://doi.org/10.1361/105996302770348682.

[50] Viacheslav Vladimirovich Sychev et al. "Thermodynamic properties of nitrogen". In: *Washington, DC, Hemisphere Publishing Corp.(National Standard Reference Data Service of the USSR. Volume 2), 1987, 355 p. Translation.* Vol. 2. 1987.

[51] Viacheslav Vladimirovich Sychev et al. "Thermodynamic properties of helium". In: *Washington, DC, Hemisphere Publishing Corp.(National Standard Reference Data Service of the USSR. Volume 1), 1987, 332 p. Translation.* Vol. 1. 1987.

[52] Wei Dai, Yixiang Gan, and Dorian Hanaor. "Effective Thermal Conductivity of Submicron Powders: A Numerical Study". In: *Applied Mechanics and Materials* 846 (July 2016), pp. 500–505. DOI: 10.4028/www.scientific.net/AMM.846.500.

[53] Dariusz Góral, Franciszek Kluza, and Katarzyna Kozłowicz. "Assessment of Heat Transfer and Mass Change During Fruits and Vegetables Impingement Pre-Cooling". In: *International Journal of Food Engineering* 10.1 (2014), pp. 183–189.

[54] Chong Huang et al. "Supersonic jet deposition of silver nanoparticle aerosols: Correlations of impact conditions and film morphologies". In: *Journal of applied physics* 101.6 (2007), p. 064902.

[55] Kiao Inthavong et al. "Simulation of sprayed particle deposition in a human nasal cavity including a nasal spray device". In: *Journal of Aerosol Science* 42.2 (2011), pp. 100–113.

[56] William C Hinds. *Aerosol technology: properties, behavior, and measurement of airborne particles.* John Wiley & Sons, 1999.

[57] J Fernandez de la Mora and A Schmidt-Ott. "Performance of a hypersonic impactor with silver particles in the 2 nm range". In: *Journal of Aerosol Science* 24.3 (1993). Aerosols in Materials Processing, pp. 409–415. ISSN: 0021-8502. DOI: https://doi.org/10.1016/0021-8502(93)90012-X. URL: http://www.sciencedirect.com/science/article/pii/002185029390012X.

[58] Gerhard W Israel and S.K Friedlander. "High-speed beams of small particles". In: *Journal of Colloid and Interface Science* 24.3 (1967), pp. 330–337. ISSN: 0021-9797. DOI: https://doi.org/10.1016/0021-9797(67)90258-5. URL: http://www.sciencedirect.com/science/article/pii/0021979767902585.

[59] G Mohan Kumar, Dominic Xavier Fernando, and R Muthu Kumar. "Design and Optimization of De Level Nozzle to Prevent Shock Induced Flow Separation". In: *Advances in Aerospace science and Applications* 3.2 (2013).

[60] Yung-Chieh Tan, Vittorio Cristini, and Abraham P. Lee. "Monodispersed microfluidic droplet generation by shear focusing microfluidic device". In: *Sensors and Actuators B: Chemical* 114.1 (2006), pp. 350–356. ISSN: 0925-4005. DOI: https://doi.org/10.1016/j.snb.2005.06.008. URL: http://www.sciencedirect.com/science/article/pii/S0925400505005228.

[61] F. White. "Viscous Fluid Flow". In: *McGraw-Hill, New York* (1974), p. 184.

[62] Jerry M. Chen, Ming-Che Kuo, and Chien-Po Liu. "Control of Droplet Generation in Flow-Focusing Microfluidic Device with a Converging-Diverging Nozzle-Shaped Section". In: *Japanese Journal of Applied Physics* 50.10 (Oct. 2011), p. 107301. DOI: 10.1143/jjap.50.107301. URL: https://doi.org/10.1143%5C%2Fjjap.50.107301.

[63] Justin M Hoey et al. "A review on aerosol-based direct-write and its applications for microelectronics". In: *Journal of Nanotechnology* 2012 (2012).

[64] I.S. Akhatov et al. "Aerosol focusing in micro-capillaries: Theory and experiment". In: *Journal of Aerosol Science* 39.8 (2008), pp. 691–709. ISSN: 0021-8502. DOI: `https://doi.org/10.1016/j.jaerosci.2008.04.004`. URL: `http://www.sciencedirect.com/science/article/pii/S0021850208000773`.

[65] F Di Fonzo et al. "Focused nanoparticle-beam deposition of patterned microstructures". In: *Applied Physics Letters* 77.6 (2000), pp. 910–912.

[66] C. Goth et al. "IEEE 61st Electronic Components and Technology Conference (ECTC)". In: *Lake Buena Vista, FL* (2011), 12111216.

[67] Ankit Mahajan, C. Daniel Frisbie, and Lorraine F. Francis. "Optimization of Aerosol Jet Printing for High-Resolution, High-Aspect Ratio Silver Lines". In: *ACS Applied Materials & Interfaces* 5.11 (2013). PMID: 23659570, pp. 4856–4864. DOI: `10.1021/am400606y`. eprint: `https://doi.org/10.1021/am400606y`. URL: `https://doi.org/10.1021/am400606y`.

[68] Paul Peter Urone, Roger Hinrichs, et al. "College Physics: OpenStax". In: (2018).

[69] DFMPro. *A DEFINITIVE GUIDE TO DESIGN FOR MANUFACTURING SUCCESS*. Geometric Limited, Dec. 2014.